UNIVERSITÉ DU LUXEMBOURG

PhD-FSTM-2025-018

Faculty of Science, Technology and Medicine

DISSERTATION

Defence held on 10 March 2025 in Luxembourg
to obtain the degree of

DE L'UNIVERSITÉ DU LUXEMBOURG

EN CHIMIE

by

Najiya
Born on 14 January 1996 in Malappuram Dist., Vazhayoor, Kerala (India)

Fabrication and Tailoring of Liquid Crystalline Elastomer Tubes: Toward Bio-Compatible Microactuators for Organoid Cultures

Dissertation Defence Committee

- Dr. Jan P.F. Lagerwall, Supervisor
  Professor, Université du Luxembourg
- Dr. Philip Dale, Chairman
  Professor, Université du Luxembourg
- Dr. Jens Schwamborn
  Professor, Luxembourg Centre for Systems Biomedicine
- Dr. Nathalie Katsonis
  Professor, University of Groningen
- Dr. Elda Hegmann
  Associate Prof., Kent State University

Fabrication and Tailoring of Liquid Crystalline Elastomer Tubes: Toward Bio-Compatible Microactuators for Organoid Cultures

Author: Najiya

A dissertation submitted for the partial fulfillment for the degree of
DOCTEUR DE L'UNIVERSITÉ DU LUXEMBOURG
EN CHIMIE

University of Luxembourg

Defence Date: March 10, 2025

Acknowledgement

Reflecting on the past four years, I am overwhelmed with gratitude for the many people who have shaped and supported my journey. As I pen this acknowledgment, I am struck by how deeply intertwined their contributions are with every milestone I've reached. It is an honor to finally express my heartfelt thanks to everyone who has been a part of this incredible chapter of my life.

Four years ago, Luxembourg welcomed me with its first snow of the season. Time has flown by, and now, on another winter night, I find it hard to believe this journey is coming to an end. I vividly recall the uncertainty of the pandemic: the tension of online interview, the ambiguity surrounding my relocation, and taking one of the first flights post-COVID to reach Luxembourg—a country I knew almost nothing about. The grey winters and post-pandemic melancholy were not easy, and adjusting to a new normal in an unfamiliar place was challenging. Yet, thanks to my incredible group, I survived. Despite cultural differences, language barriers, and other hurdles, I was fortunate to form friendships that have been integral to both my personal and professional growth during this PhD journey.

First and foremost, I express my deepest gratitude to Prof. Jan Lagerwall, who gave me this opportunity and guided me tirelessly to the finish line. Without his support and encouragement, this journey would not have been possible.

I owe a debt of gratitude to every member of ESMP for their support and collaboration. To Rijesh, thank you for your invaluable chemistry insights and for always being a phone call away, even after moving on to new opportunities. To Alejandro, who has been extremely helpful with my research and together with Xu, making our shared office a positive space, thank you. To Zory, I am grateful not only for your help with administrative work but also for your gentle and kind nature, always offering support whenever you could. To Yansong, thank you for your willingness to assist with experiments whenever required. To Nikolay for our collaboration on the first paper—thank you for your involvement. I would also like to acknowledge Yosuke, Larry, and the rest of the team for their contributions and support. A heartfelt thanks goes to former colleagues Anjali, and Yong, who generously helped me train on different techniques, making a lasting impact on my skills.

I also extend my heartfelt thanks to my CET members, Prof. Jens Schwamborn and Prof. Nathalie Katsonis, for their valuable feedback and suggestions over these four years. To the technicians Uli and Bob, your help with setups and experiments has been invaluable. To Sònia Sabaté Soler and Anna-Sophie Zimmermann at LCSB for their assistance with biology experiments, which contributed significantly to my work. I also wish to thank Prof. Philip Dale, with whom I had the privilege of working as

a teaching assistant for the lab course. It is truly an honor to now have him serve as the chairperson of my defense committee.

My friends often joked that this was a "collective PhD", and I wholeheartedly agree. Many people stood by me and played pivotal roles throughout. To my college friends—Haseeb, Femi, Kripa and Asha—who shared their own PhD stories from different parts of the world, and to Adarsh, for his steady friendship—thank you for helping me navigate this journey. Majdi, in particular, has been one of the first friends I made in Luxembourg and has truly become like family to me here. To Ricardo, who believed in me even when I doubted myself, and to Deniz, my best flatmate, who supported me in countless ways and pampered me during tough times, I am sincerely thankful. To Mubeen and Amritha, for their steadfast encouragement, being a source of calm and reassurance during difficult times, and for the thoughtful meals they prepared for me during thesis writing, I am incredibly grateful. Their support, both emotional and practical, made a world of difference during those challenging moments. To Katrin, despite not sharing office space anymore, our bond remains strong, and I am truly grateful for her unwavering support. To other friends, including Kilian, Sharadhi, Andrea, Alba, Tabea, Narges and many others, thank you for making my time on the Limpertsberg campus so enjoyable. Those little breaks amidst hectic research schedules will always be cherished. The laughter we shared, the motivation we gave each other, and the team spirit we built made those moments so memorable. Standing side by side, we grew stronger together.

My family has been my backbone throughout this journey. My mother and sister have been my unwavering pillars of support, and words cannot express how much they mean to me. This acknowledgment page is far too small to capture the depth of my gratitude to them. I also wish to honor my grandfather, who is no longer here to see me achieve this goal. He was a major source of motivation in my life, always encouraging me to pursue my dreams. His joy and pride in my success were greater than anyone's, and I can only wish he were here to witness this accomplishment.

This PhD journey has been a rollercoaster, filled with moments of happiness with each breakthrough and disappointment with each setback. There were times when I wanted to give up, but looking back, I realize it was all worth it. As I reflect, I feel a sense of sadness knowing that countless experiments remain yet to be explored, and I won't have the opportunity to delve into them at ESMP. This journey has taught me that there is always more to learn, and I remain open to embracing those lessons in the future.

To everyone who has contributed to this journey in one way or another, thank you!

Najiya

Abstract

Liquid crystal elastomers (LCEs) with their unique combination of mechanical flexibility and responsive actuation, hold immense potential for mimicking biological functions and enabling advanced actuation systems. However, creating complex ground state shapes for LCEs beyond basic sheets or fibres is challenging. The first part of the thesis focuses on the fabrication of arbitrarily long tubular LCE actuators using a continuous coaxial flow microfluidic technique. This scalable approach produces hollow LCE tubes that can be actuated thermally to act as peristaltic pumps, moving fluids in and out. This capability makes them suitable for use as synthetic vasculatures in biological contexts, potentially delivering nutrients and oxygen to organoids and waste removal from them.

In the second part, photoresponsive nematic LCE sheets are synthesized using oligomeric precursors functionalized with azobenzene. The photoactuation of these materials is systematically analyzed across different temperatures, with particular attention to the nematic-isotropic transition under UV light. These sheets performed well at physiological temperatures ($30 - 37°C$), making them viable candidates for isothermal actuators embedded in biological systems, such as organoids functioning without harmful UV light, crucial for maintaining cell viability. Additionally, towards the end of the thesis, the biocompatibility of the LCE materials in organoids are also investigated focusing on their ability to function as peristaltic pumps in the future.

This thesis advances on the understanding and demonstrating how tailored LCE can address critical challenges in biotechnology, including the need for scalability, biocompatibility and functionality. This work lays the foundation for integrating LCEs into future organoid and soft robotics applications.

Contents

Chapter 1

Introduction

1.1 Overview of the thesis

LCEs are a unique class of materials that combine the dynamic responsiveness of liquid crystals (LCs) with the mechanical flexibility of elastomers. This dual functionality enables reversible and controllable shape changes, making LCEs promising candidates for applications in soft robotics[1], tissue engineering[2], and electronics[3]. However, challenges remain in fabricating complex geometries, optimizing responsiveness, and integrating LCEs into living systems. This thesis addresses these challenges by developing innovative LCE fabrication techniques, tailoring their functionality, and exploring their biocompatibility for advanced applications. This overview provides a detailed introduction to the motivation, objectives, and scope of the thesis.

The second and third chapters lay the foundation by covering general topics, experimental setups, and protocols essential for the entire thesis. These include the fundamental principles of liquid crystal behavior, LCE synthesis and fabrication techniques, and mechanisms of actuation under external stimuli like heat and light. This chapter provides the theoretical and practical background necessary for understanding the subsequent work.

The fourth chapter focuses on the development of tubular LCE actuators using a continuous coaxial flow microfluidic process. LCE tubes, because of their hollow structure and large inner surface area, make them highly suitable for efficient fluid transport and functionalization for specific needs[4–6]. Simulations have also suggested that LCE tubes could exhibit peristaltic pumping behavior when actuated along their length[7]. However, realizing such well-defined, dynamic actuation in LCE tubes has proven challenging, as existing fabrication methods face several limitations.

Many traditional approaches rely on static fabrication techniques that inherently constrain the scalability and uniformity of the tubes. For instance, some methods encapsulate LCE precursor liquids within cylindrical molds made of glass[8] or Teflon[9], where the tube dimensions are restricted by the mold size. Others involve rolling preformed LCE sheets into tubular structures[10], which limits the achievable length to the dimensions of the sheet. In another method, short sections of large-diameter LCE tubes were created using 3D-printed filaments arranged in a spiral pattern[11], but this approach is unsuitable for producing long, continuous tubes. Braun et al. proposed

a more dynamic fabrication technique, using a triple-phase microfluidic approach to create spherical LCE shells. These were elongated into millimeter-length cylinders using narrow capillaries and photocrosslinked to form LCE tubes[12]. Although this method demonstrated the feasibility of fabricating tubular LCE structures, the resulting tubes were limited in length by the size of the initial LCE shells and the capillary geometry. In addition, cutting the cylinders into smaller sections to confirm actuation restricted the functionality of the tubes.

Addressing these challenges, this work presents a scalable method that enables the fabrication of LCE tubes with arbitrary lengths and controlled alignment through flow-induced shear and in situ photocrosslinking. By tailoring the viscosities of the LCE precursor and the inner and outer isotropic phases, as well as minimizing interfacial tension, the onset of the Rayleigh–Plateau instability is delayed, stabilizing the tubular precursor over lengths on the order of 10 cm. The resulting tubes exhibit reversible thermal actuation and demonstrate peristaltic pumping behavior when locally heated. This chapter also characterizes the director field using polarizing optical microscopy (POM) and links the alignment to the observed actuation behavior. It is proposed that the tubes on functionalized for light-triggered actuation can act as artificial vasculature in organoids.

The fifth chapter transitions to the synthesis and characterization of photoresponsive LCE sheets functionalized with azobenzene. Designed to operate at physiologically relevant temperatures ($30 - 37°\mathrm{C}$), these materials are suitable for biotechnological applications, including integration with organoids and other living systems. The LCE sheets are fabricated from LC oligomer precursor solutions, enabling the formation of monodomain sheets with uniform alignment, a critical factor for achieving efficient actuation.

Isothermal actuation, a key focus of this chapter, addresses the limitations of traditional thermal actuation methods, which are incompatible with bioderived materials due to temperature sensitivity. The incorporation of azobenzene moieties allows dynamic modulation of the nematic-isotropic transition temperature (T_{NI}) through UV-induced switching between LC-promoting (rod-shaped *trans*-isomer) and LC-disturbing (kinked *cis*-isomer) configurations[13, 14]. However, photoactuation in such systems is not straightforward due to the interplay of competing phenomena.

Thermally induced back relaxation and uncontrolled local heating during UV irradiation complicate the actuation process. Efficient photoactuation requires that T_{NI} prior to UV irradiation remain well above the operating temperature, but drop to or below it after UV exposure[15, 16]. Programming of LCEs typically involves aligning the mesogens in a desired orientation and then using photocrosslinking to fix this alignment in the LCE network. However, this process competes with the photoisomerization of azobenzene moieties, making it challenging to program LCEs effectively.

The systematic analysis of T_{NI} behavior under UV irradiation identifies the optimal operating conditions while minimizing UV exposure, ensuring compatibility with biological systems. Incorporating tetrafunctional crosslinkers, as introduced by Jeong et al., offers a viable solution to mitigate the competition between photocrosslinking and photoisomerization, enabling the development of more efficient photoresponsive LCEs[17]. This chapter establishes the foundations for the use of photoresponsive

LCEs in living systems, offering strategies to overcome current challenges and unlock their potential for advanced biotechnological applications.

Chapter Six focuses on evaluating the biocompatibility of LCE materials in midbrain organoid (MO) cultures, providing critical insights into their potential integration with living systems for advanced biomedical applications.

The study incorporates LCE tubes into pluripotent stem cells on day 0 of differentiation, allowing the cells to mature into fully developed organoids by day 30. Analysis reveals that the LCE materials exhibit good biocompatibility; however, the large diameter of the LCE tubes hinders their full integration into the organoids. Since it was not feasible to fabricate LCE tubes with smaller diameters, the study instead introduces LCE fibers with diameters of 10–20 μm to overcome this limitation. The results confirm that these smaller LCE fibers are fully compatible with the organoid environment and successfully integrate into the MOs without hindering their development. Furthermore, lactate dehydrogenase (LDH) assays indicate minimal cell death, corroborating the cytocompatibility of the LCE materials. These findings highlight the significance of optimizing the dimensions of LCE tubes for seamless integration into biological systems.

The final chapter discusses potential advancements, including the development of light-actuated LCE tubes, porous LCE designs, and reduced-diameter tubes. These innovations could further expand the utility of LCEs in tissue engineering, soft robotics, and other emerging fields.

In summary, this thesis contributes to the advancement of LCE technology by addressing challenges in scalability, functionality, and integration. By bridging the gap between material design and real-world applications, it establishes LCEs as versatile and practical materials for bio inspired systems and next-generation technologies.

Chapter 2

Relevant concepts

2.1 Liquid crystals

Liquid crystals (LCs) are materials that form mesomorphic phases, i.e., phases with intermediate properties between Nature's two most common condensed matter phases, the solid and the liquid, as shown in figure 2.1. As the name suggests, this class of condensed matter shares the properties of both liquids and crystals. Like liquids, they exhibit fluidity and an inability to sustain shear stress. LCs display properties similar to those of crystals, notably by showing anisotropy in their optical, electrical, and magnetic behaviors. This means that LCs respond differently to light, electric fields, and magnetic fields depending on the direction in which these interactions occur. They also show long-range orientational and sometimes long-range positional orders, like solid crystals. Molecules that tend to form liquid crystalline phases by self-organizing are called mesogens. These mesogens often contain (1) a *core*, usually made up of aromatic or aliphatic rings. The rigidity of the core contributes significantly to the anisotropy of the molecule. (2) Flexible *alkyl chains*, which contribute to the flexibility and fluidity of the the LC phase; and (3) *terminal groups*, which are different functional groups attached to the end of the molecule and can influence mesogenic properties [18]. Figure 2.2 shows the structure of the most commonly used nematic mesogen 4-Cyano-4'-pentylbiphenyl (5CB) with the three regions demarcated.

LC forming compounds that show one or more anisotropic phases over a specific temperature range are known as thermotropic LC materials [19]. LCs obtained when amphiphilic mesogens are mixed with a solvent are called lyotropic LCs. In lyotropic LCs, the concentration of the solution is the most crucial parameter that determines the stability of the LC phase while in thermotropic LCs, it is the temperature that is most crucial [20]. The most important property of an LC phase is its anisotropy, which causes it to exhibit birefringence.

Intermolecular interactions, including van der Waals forces, hydrogen bonding, and electrostatic forces, strongly influence how mesogens are arranged into structured phases. In thermotropic LC compounds, as temperature changes, the strength of intermolecular interactions shifts, driving phase transitions in liquid crystals. These transitions can either move the material into different LC phases or lead to a shift from an LC phase to an isotropic liquid phase or to a solid crystalline phase. The

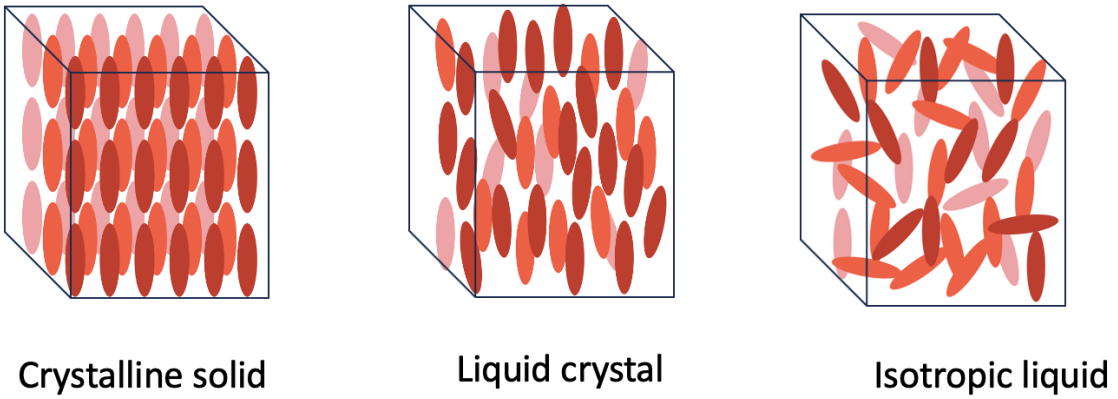

Figure 2.1: Schematic diagram of the states of matter: solid, liquid crystal, and liquid. The solid state is characterized by a fixed, orderly arrangement of molecules, resulting in a definite shape and volume. In contrast, the liquid state exhibits a disordered arrangement, allowing molecules to flow and take the shape of their container while maintaining a constant volume. The liquid crystal state is depicted as an intermediate phase, exhibiting both liquid-like flow and ordered molecular alignment.

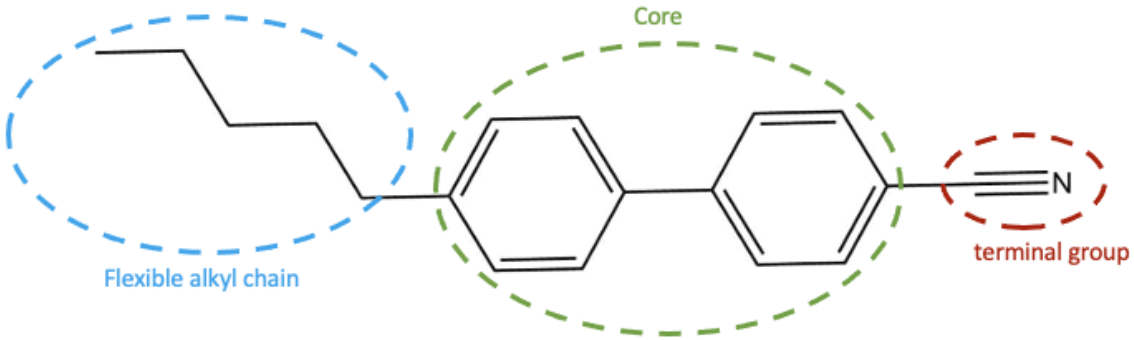

Figure 2.2: Molecular structure of 4-pentyl-4'-cyanobiphenyl (5CB), illustrating the distinct regions within the molecule: a rigid core, a flexible alkyl chain, and a terminal group.

molecular structure of the mesogen (e.g., rod-like, disc-like) also influences the type of liquid crystalline phase that forms. Depending on their structural properties, LCs are classified into, for instance, nematic, cholesteric, smectic, and columnar mesophases. There are other categories and subcategories of each one, but they will not play a role in this thesis. For this project, we used the thermotropic LC nematic phase. Thus, the following section gives a brief description of the nematic phase.

2.1.1 The director concept

The term director (**n**) refers to the primary orientation or average alignment direction of the long molecular axes in a liquid crystalline material. In a monodomain sample, the director is uniform throughout the sample, which means that the average molecular alignment direction is the same throughout. However, this does not imply perfect molecular alignment as in a crystal; instead, individual molecules fluctuate around the director. The alignment of the director in monodomain samples is typically achieved using various processing methods such as rubbing a surface, applying an electric or magnetic field, or through self-assembly processes during fabrication. This uniform average alignment of mesogens allows for predictable and controllable optical and mechanical properties.

In contrast, polydomain LCs have multiple regions (domains) with different average orientations; each domain will have its own director. These multiple domians can influence the overall behavior of the material, often resulting in isotropic or averaged properties. This type of LCs are commonly observed in samples in which no external aligning forces are applied. Monodomain samples are often used in optical and electronic devices because of their uniform properties, while polydomain systems are advantageous in applications requiring tunable or dynamic responses, such as in soft robotics or bio-inspired materials.

2.1.2 Optical anisotropy in liquid crystals

The unique optical properties exhibited by LCs stem from their anisotropic molecular alignment. Optical anisotropy refers to the directional dependence of a material's optical properties. It is one of the most distinctive features of LCs, where their interaction with light depends on the orientation of the incident light relative to the director.

A direct consequence of optical anisotropy is the phenomenon of birefringence. Although optical anisotropy is a general property that describes how the material properties differ in different directions, birefringence is a specific, measurable effect. It is defined as the property of a material to exhibit two distinctive refractive indices for light polarized in two different directions. Specifically in LCs, light polarized parallel to the director experiences the extraordinary refractive index (n_e), while light polarized perpendicular to the director encounters the ordinary refractive index (n_o). The difference between these refractive indices, $\Delta n = n_e - n_o$ is referred to as the birefringence of the material.

The birefringence of the liquid crystals is a direct consequence of their molecular alignment and orientational order. In a monodomain sample, where the director orientation is uniform, the observed birefringence is consistent throughout the material.

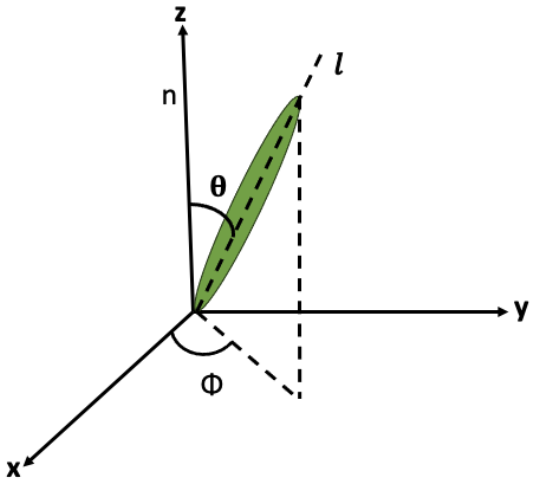

Figure 2.3: Schematic representation of the orientation of a rod-like LC molecule in the coordinate system. The vector **l** represents the long axis of the molecule and the director **n** is along the z-axis.

In contrast, a polydomain sample contain domains with differing director orientations, leading to spatial variation in the effective birefringence due to changes in optical axis orientation relative to the incident polarized light.

These spatial variations in birefringence can be visualized using polarized optical microscopy (POM) when the sample is viewed between crossed polarizers. Because LCs are optically anisotropic, the amount of light transmitted through each region depends on the local director orientation relative to the polarizer and the analyzer. This results in bright and dark regions or interference colors that reflect the spatial distribution of the director. In nematic phases, Schlieren textures are observed that are marked by brush-like patterns with disclination points (defects). The number and arrangement of brushes provide information about the strength and type of defect. These textures not only reveal the local orientation but also provide valuable information on the alignment, defects, and phase structure of the liquid crystal sample.

2.1.3 The orientational order parameter

Anisotropic systems require a set of parameters that can describe the mesophase in certain thermodynamic conditions. While **n** represents the average alignment of the long molecular axes in a liquid crystal sample, the orientation order parameter (S) quantifies the degree of alignment of the LC molecules relative to **n**. Each individual molecule in a liquid crystal sample retains some mobility while they tend to align their long axis along the **n** resulting in partial order. The extent of this alignment is determined by the scalar orientational order parameter.

Mathematically, S is defined as:

$$S = \left\langle \frac{3\cos^2\theta - 1}{2} \right\rangle$$

where θ is the angle between the long axis of an LC molecule and the director, as shown in figure 2.3, and the angular bracket denotes the average over all molecules in

the sample.

The value of S ranges from $-\frac{1}{2} \leq S \leq 1$, with $S = 0$ implying completely random orientation, characteristic of an isotropic LC phase, and $S = 1$ implying perfect orientational order, where all molecules are aligned parallel to the director, though this ideal value is rarely achieved in practice. The negative order parameter refers to the rare cases in which molecules are predominantly oriented perpendicular to the director [21].

Typically for a nematic LC, S is between 0.4 and 0.6 depending on the temperature and the specific liquid crystal material [20]. As the LC sample approaches the nematic-to-isotropic transition temperature (T_{NI}), S decreases as thermal fluctuations disrupt molecular alignment. In contrast, at lower temperatures, S approaches high values because of strong intermolecular interactions that favor alignment.

2.1.4 Nematic Liquid crystals

The nematic phase represents the most basic type of liquid crystal phase and exhibits the lowest level of order. In this phase, the molecules possess long-range orientational order, meaning they align along **n**, but there is no long-range positional order. The term "nematic" has a Greek origin, which translates to "thread," referring to the optically distinct threads (defects) exhibited on a birefringent background. Both rod-like (calamitic) and disc-like (discotic) LCs can generate nematic phases, but they maintain distinct characteristics and do not typically mix. This distinction arises from their different molecular geometries, which influence their behavior and interactions.

Nematic phases tend to be favored when the terminal chains are short in rod like molecules. For example, 5CB exhibits a nematic phase near room temperature (24℃-35℃). Hence, the 5CB molecule can be referred to as a nematogen, i.e., the nematic phase is the only mesophase exhibited. Chiral nematic phases, also called cholesteric, is the nematic phase developed in a chiral system, in which the molecular director rotates helically throughout the material, along an axis perpendicular to the director itself. These phases can occur in materials as a direct consequence of the chiral nature of the mesogens or the presence of chiral dopants in an otherwise non-chiral nematic LC [18].

2.2 Elastomers in general

A material's ability to deform in response to an applied force and return to its original shape and size once those forces are removed is called elasticity. Young's modulus quantitatively measures a material's stiffness in the context of solid mechanics. It defines the linear relationship between stress and strain within the linear elastic region of a material's stress-strain curve. This relationship is given by Hooke's law and expressed as:

$$\sigma = E \cdot \varepsilon \tag{2.1}$$

where σ is the stress, ε is the strain and E is the Young's modulus. Stress is defined as the force applied per unit area:

$$\sigma = \frac{F}{A} \tag{2.2}$$

where F is the applied force and A is the cross-sectional area over which the force is applied. Strain is defined as the relative deformation of the material:

$$\varepsilon = \frac{\Delta L}{L_0} \tag{2.3}$$

where ΔL is the change in length and L_0 is the original length.

A high value of Young's modulus indicates that a material exhibits significant resistance to deformation when subjected to stress, reflecting its stiffness or rigidity. Conversely, a lower Young's modulus suggests that the material is more compliant or flexible. Elastomers are polymeric materials, natural or synthetic, that exhibit significant elasticity. They can undergo large deformations under applied stress and return to their original shape upon release of the stress without breaking due to their ability to rotate their constituent polymeric chain elements about the chain bonds [22]. Young's modulus and elastic limit are two parameters used to quantify a material's elasticity. The elastic limit refers to the highest stress level that a material can withstand without experiencing permanent deformation. Beyond this threshold, the material will not return to its original shape after the applied stress is removed. Unlike a rigid solid, which has a Young's modulus in the range of approximately 10^5 N/mm^2 and a corresponding maximum elastic limit of about 1% or less, rubber has a very low Young's modulus of 1 N/mm^2 and high extensibility in the range of 100-800% [23]. Rubber does not undergo any volume change during deformation (Poisson's ratio is 0.5).

At the molecular level, elastomers consist of long-chain polymers that are lightly cross-linked. They are generally amorphous, implying the chains are coiled and entangled (figure 2.4) rather than arranged in a regular pattern. This randomly oriented or coiled structure gives elastomers their unique properties. For a material to show rubber-like elasticity, it should fulfill these requirements [23]: a) The presence of long-chain molecules. These polymer chains provide flexibility to the elastomer, allowing the chains to slide past each other and stretch out when force is applied. b) Weak secondary forces between the molecules. Van der Waals forces, including dispersion forces and dipole-dipole interactions, allow polymer chains to move past one another when subjected to stress, facilitating the stretching of the material. c) Cross linking the polymer chains through chemical bonds at a few places along their length to form a 3D network. These cross-links provide the material "memory" effect, enabling it to return to its initial shape after being deformed. The stiffness of an elastomer, quantified by its Young's modulus, is determined by the density of crosslinks in the material.

Crosslinked natural rubber and a wide variety of synthetic rubbery polymers show characteristic Gough-Joule Effect [24, 25]: a)When rubber is stretched, it releases heat and warms up, and when it is released, it cools down. b)Under a constant load, stretched rubber will shrink when heated and elongate when cooled. This characteristic of rubber is due to its entropy elasticity. As rubber is stretched, its polymer chains adopt more extended conformations, reducing their conformational entropy (as depicted in figure 2.5). In the case of chemically cross-linked rubber, such as vulcanized rubber, the process of vulcanization introduces covalent bonds between polymer chains, which prevent complete uncoiling. Similarly, physical cross-links, such as crys-

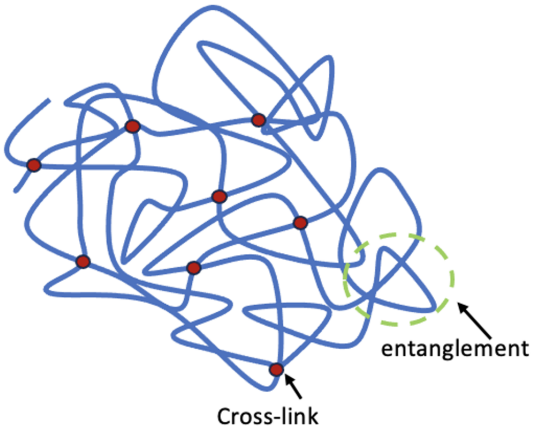

Figure 2.4: Depicts the random-coiled conformation of an elastomer, highlighting the presence of crosslinks and entanglements within the polymer structure.

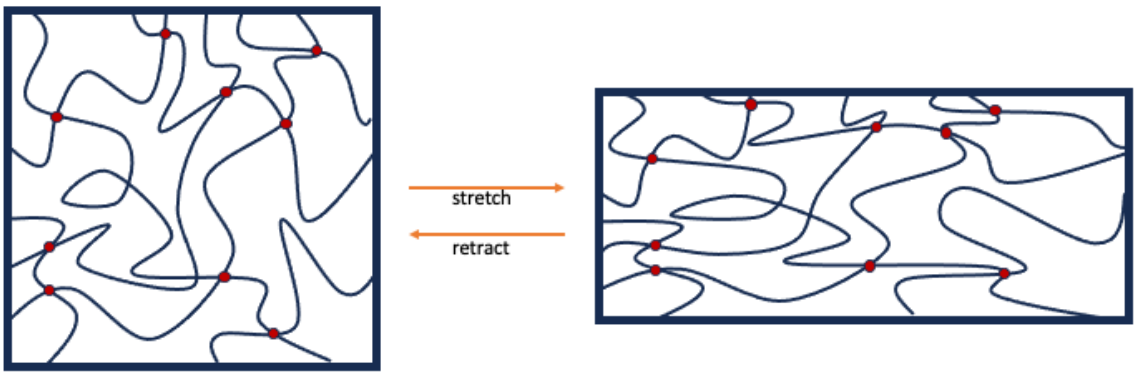

Figure 2.5: Demonstrates the changes occurring in an elastomer network upon uniaxial stretching. As the elastomer is extended, the originally coiled polymer chains align along the direction of the applied force, resulting in increased chain orientation.

tallites, and temporary entanglements also restrict the motion of the chains, though their effects may differ in duration and strength. During the application of tensile strain—particularly in an adiabatic manner, where there is no heat exchange with the surroundings, the rubber molecules align along the direction of the applied force. This alignment decreases the system's entropy as the polymer chains become more ordered [26]. According to the first law of thermodynamics:

$$\Delta U = Q - W \tag{2.4}$$

Where ΔU is the change in the internal energy of the system, Q is the heat exchanged with the surroundings, and W is the work done by the system. In adiabatic process, Q = 0, so the equation becomes:

$$\Delta U = -W \tag{2.5}$$

In the case of rubber under tension, the work done by the applied force stretches the material, causing the molecular chains to align and decreasing the system's entropy. Since no heat is exchanged in this adiabatic process, the decrease in entropy must be balanced by a corresponding increase in internal energy. In practice, much of this energy goes into raising the kinetic energy of the molecules- which manifests as a rise in temperature. This results in the warming of the rubber during stretching.

Although the molecular conformation changes with deformation, the angles and lengths of bonds remain unchanged until excessive force breaks the carbon-carbon bonds, leading to the breakage of the rubber piece. When the rubber is free of the force applied, the molecules coil up again due to the free rotation of atoms to restore the maximum entropy it had in its disordered state. If the retraction occurs adiabatically-without heat exchange- the rubber must perform work (W $>$ 0) on its surroundings using its own internal energy. As a result, the internal energy decreases, leading to a drop in the rubber's temperature. This cooling effect can be felt when the rubber is released rapidly. If the process is not adiabatic, heat from the surroundings is absorbed to supply the energy needed for retraction. This reversible process where the elastomeric materials experience temperature changes when they are subjected to mechanical deformation, like stretching or releasing, under adiabatic conditions, is referred to as the thermoelastic effect.

According to Kuhn's model [27], rubber elasticity can be explained by considering an ideal rubber polymer chain as a series of "Kuhn segments" or "Kuhn lengths". A Kuhn segment is the shortest length over which a polymer chain can adopt any spatial conformation independent of other segments. When rubber is stretched, the polymer chains are maximally aligned and extended as the thermal fluctuations are constrained (the chains become more ordered). The number of conformations available to each chain reduces, leading to a decrease in entropy. When the external stretching force is removed, the system's natural tendency to revert to the original disordered state gives rise to the elastic or restoring force. This model mainly treats rubber elasticity as fundamentally entropic.

When the stretched rubber is heated, the molecules in the rubber are supplied with the kinetic energy needed to revert to their higher entropy state, the more random (coiled) state and the effective length of the rubber decreases. This decrease in length

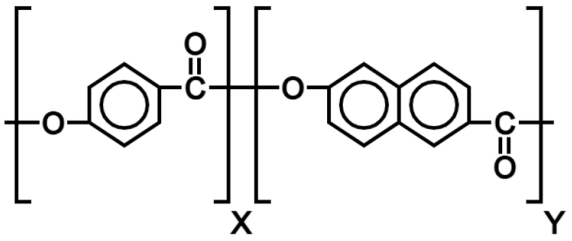

Figure 2.6: Chemical structure of Vectra

is what causes the rubber to contract upon heating. The Gibbs free energy can explain why this process is thermodynamically favorable. The change in Gibbs free energy is given by:

$$\Delta G = \Delta H - T\Delta S \tag{2.6}$$

where:

- ΔG represents the change in Gibbs free energy,
- ΔH denotes the change in enthalpy,
- T indicates absolute temperature,
- ΔS signifies the change in entropy.

In the case of stretched rubber, ΔS is positive as the chain reverts to its highest entropy state (coiled conformation). Thus, the term TΔS is positive. Since, the stretching process is primarily an entropy driven one, the enthalpy change during the heating phase does not contribute significantly to the free energy change. Therefore, $\Delta H \approx 0$ can be considered, leaving ΔG primarily driven by the term $T\Delta S$. Since ΔS is positive, this makes ΔG negative.

2.3 What are Liquid Crystal Elastomers (LCEs)?

Liquid crystalline polymers (LCPs) are a broad category of materials that exhibit liquid crystalline behavior due to the rigid, rod-like structures in their polymer backbones. These materials can be crosslinked or uncrosslinked. Linear LCPs like Vectra shown in figure 2.6, are high performance polymeric material that are primarily comprised of uncrosslinked macromolecules that can establish liquid crystalline phases. The intermolecular interactions allow these macromolecules to align and organize themselves in an ordered fashion. Liquid crystalline networks (LCNs) refer to LCPs that are chemically crosslinked, creating a network structure shown in figure 2.7b. Crosslinking can range from light to heavy, influencing the material's mechanical properties. While LCNs can still exhibit liquid crystalline behavior, the crosslinking process results in a network structure that restricts the movement of the polymer chains, making the material more rigid or glassy compared to uncrosslinked LCPs.

Liquid crystal elastomers (LCEs) represent a subclass of liquid crystalline networks, characterized by a relatively low degree of crosslinking (figure 2.7c) and retain elastomeric properties. These materials combine properties characteristic of both liquid crystals and elastomers: like liquid crystal systems, they self-organize, and like elas-

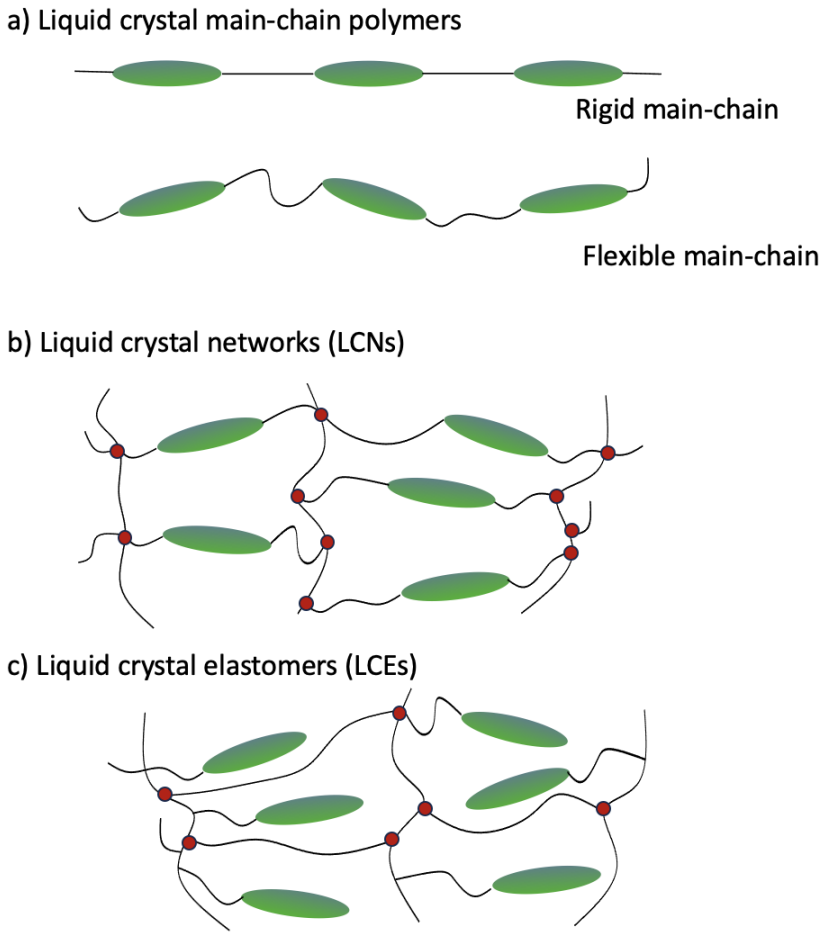

Figure 2.7: Schematic depiction of a) Liquid crystal main-chain polymers, b) Liquid crystal networks and c) Liquid crystal elastomers

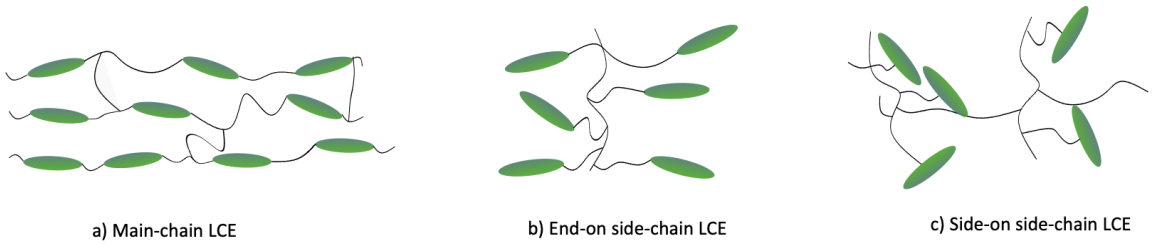

Figure 2.8: Schematic diagram illustrating the different attachment geometries of liquid crystal elastomers (LCEs). a) Main-chain LCEs b) End-on side-chain LCEs. c) Side-on side-chain LCEs.

tomers, they exhibit elastic properties [28, 29]. Nematic LCEs combine anisotropic long-range orientational order with the short range positional order typical of isotropic liquids. In LCEs, the weak crosslinking of the polymer network couples the orientational order of the liquid crystal molecules with the network itself. This coupling causes the network to align along the **n**, making the entire network anisotropic. When exposed to external stimuli like temperature, light, or other stimuli, LCEs can macroscopically change shapes due to the reorientation of LC molecules which translates to the elastomeric network [29–31]. Therefore, LCEs are potential candidates for a range of applications. For instance, LCEs can be used as artificial muscles owing to their substantial uni-axial contraction in the direction of the director when external stimuli like heat is applied, which disrupts mesogen alignment and induces actuation [32]. In contrast, other LCNs with high crosslinking densities, lack clearing points. Instead, their actuation is mainly driven by anisotropic thermal expansion and takes place over a wide range of temperatures [33]. In LCEs, the actuation is entropy-driven (a detailed description is given in the next section).

LCE polymers can adopt different architectures, including main-chain polymers, where the mesogenic groups are integrated directly within the polymer backbone, and side-chain polymers, where mesogenic units are attached to the backbone through spacer groups either end-on or side-on (figure 2.8) [34]. The geometry of the attachment of mesogenic units significantly influences the liquid crystalline phase of LCEs. For example, when mesogenic units are connected end-on, they often promote the formation of a smectic phase because of their ability to pack into layered structures with long-range positional orders. In contrast, side-on attachments due to their lateral linkage of mesogens tend to hinder the formation of layered structures and instead generally form a nematic phase [30, 35].

Liquid crystal elastomer actuation

The actuation of liquid crystal elastomers is driven by the disruption of the aligned mesogens in the elastomer matrix when transitioning from an ordered liquid crystalline phase to a disordered isotropic phase. As first demonstrated by Finkelmann and Kupfer [36], heating nematic monodomain LCEs to their isotropic state causes anisotropic deformation, thereby showcasing their thermally induced actuation. They synthesized monodomain liquid crystal elastomers (LCEs) using a two-step synthesis method. In the initial phase, they produced a lightly crosslinked network and then applied a constant load to deform the material, promoting a uniform alignment of the director throughout the network. A second crosslinking is done in the second step to arrest the network anisotropy. The alignment along this preferred direction of stretching, or chain anisotropy establishes the material's deformation axis. The LCE undergoes a phase transition when exposed to external stimuli such as heat or light, shifting from an ordered nematic phase (lower entropy) to a more randomly oriented (higher entropy) isotropic phase. This phase transition results in changes to the material's overall shape and size.

During this phase transition, the mesogens tend to randomize their orientation, losing their molecular alignment along the director. In non-chiral nematic LCEs, this transition can lead to a fully isotropic state depending on the degree of crosslinking. The loss of long-range orientational order in the isotropic phase allows the polymer

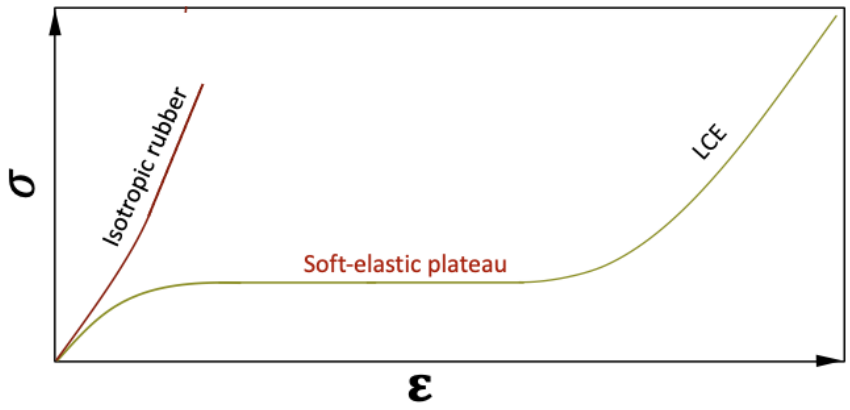

Figure 2.9: Stress-strain curve for isotropic rubber and LCE where strain is perpendicular to the nematic director **n**.

chains to adopt random conformations, maximizing entropy and lowering free energy. As a result, the elastomer network contracts along the original director axis because the chains return to their natural coiled state. Due to the material's near-incompressibility, this contraction along the director causes an expansion perpendicular to it, leading to anisotropic shape change. This volume-conserving deformation is the fundamental mechanism behind the LCE's actuation. When the external stimulus is relieved and the material cools back to the nematic phase, the mesogens realign along the director, allowing the LCE to revert to its original shape. The actuation of LCEs can be tweaked by controlling various factors like type and concentration of mesogens, nature of stimuli, and the initial alignment of LCEs.

Soft Elasticity of nematic LCEs

LCEs resemble traditional rubber in molecular architecture. They have low crosslinking density, which allows the chain molecules to slide past one another, and the material can stretch under minimal force.

In addition to the entropy-driven elastic response, LCEs show soft-elasticity, which is absent in isotropic rubber (figure 2.9). In nematic LCEs, under a certain strain, due to their additional contribution from liquid crystalline order, LC director can reorient without significantly stretching the polymer chains. Since this reorientation does not incur an entropy cost, it does not result in a rise in free energy. As a result, negligible stress is required to cause this liquid-like deformation [37]. In monodomain LCEs, when a strain is applied in the direction of nematic director, the material exhibits a linear stress-strain response like in classical rubber. However, when tensile strain is applied perpendicular to the director, the LCE stretches with minimal stress as the director reorients to adopt a new, energetically favorable configuration. Significant stretching, often up to several hundred percent, occurs when the LCE is stretched perpendicular to the director [28]. This soft elastic response arises because the nematic director of the LCE realigns itself along the direction of the applied stretch, minimizing resistance to deformation. (See figure 2.10.)

Experimentally, both monodomain and polydomain NLCEs display a plateau in the stress-strain curve [40, 41]. Based on the figure 2.11 graph, LCEs initially behave

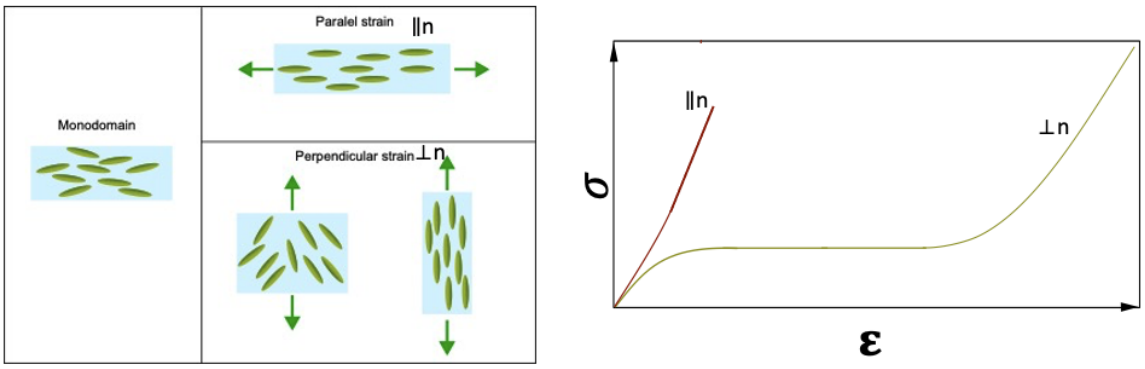

Figure 2.10: Graphical representation illustrating strain applied both parallel and perpendicular to the nematic director in a monodomain LCE, along with the corresponding stress-strain curves. Adapted from [38].

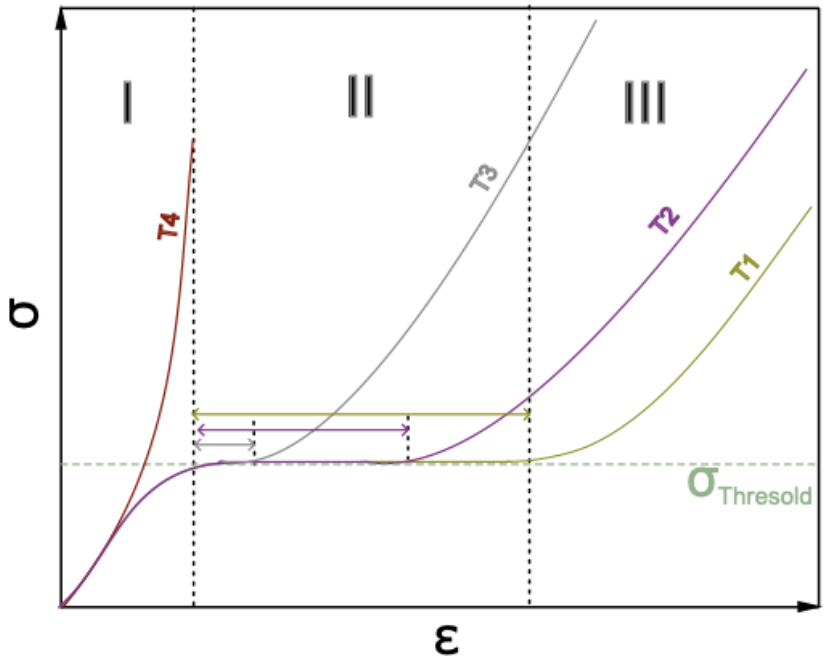

Figure 2.11: Stress-strain curves for liquid crystal elastomers (LCEs) measured at different temperatures T1 $<$ T2 $<$ T3 $<$ T4. Each curve shows the material's mechanical response, highlighting temperature-dependent behavior. The soft-elastic plateau region is indicated by double arrows, representing a distinctive region where the stress response remains relatively constant under increasing strain. Adapted from [39].

like an isotropic rubber at low strains, with the stress increasing in line with classical theory of rubber elasticity (region I). Upon reaching a certain strain level, the curve enters Region II, characterized by a plateau, indicating further deformation requires zero energy. This results in constant stress despite significant increase in strain (soft-elasticity plateau) [42]. This is due to liquid crystalline molecules undergoing reorientation without significant elastic deformation of the polymer backbone. In region III, the stress again increases with increased strain, indicating an energy requirement that causes further deformation. By this point, the nematic director has reoriented along the tensile strain direction, and any additional strain begins to stretch the polymer chains, leading to a conventional entropic elastomeric response. The Young's moduli before and after the plateau are different. Also, from the plot, if you observe the stress-strain curve for other temperatures ($T1 < T2 < T3 < T4$) below region I, Young's modulus of monodomain does not change much with temperature. As temperature increases from $T1$ to $T4$, the plateau width narrows and eventually vanishes for isotropic temperature ($T4$). Above isotropic temperature, the system behaves similarly to conventional rubber.

2.4 LCE Synthetic Chemistry

LCE synthesis methods can be broadly categorized into two main types depending on the precursor utilized: monomers or oligomers. Oligomers are intermediate-sized molecules composed of a few repeating units (typically 2–20), larger than monomers but smaller than polymers, and they retain some of the physical characteristics of both.

In the monomer-based approach, all the monomers, including mesogenic units, crosslinkers, chain extenders and radical initiators are mixed, and the polymerization and crosslinking occur together at the aligned state. By carefully selecting and designing the monomers, the resulting LCEs can exhibit tailored mechanical, optical, and thermal properties. Typically, the monomers are aligned in LC phase before crosslinking to ensure the desired anisotropic structure. However, it often requires stringent processing conditions, such as use of alignment layers or external fields, to achieve uniformity in the liquid crystal orientation. The complexity of this method limits its scalability for large-scale applications.

Oligomer-based approach uses pre-synthesized LC oligomers as precursors. After partial polymerization and light crosslinking, the resulting network can be mechanically stretched to align the director uniformly. A second crosslinking step fixes the aligned structure, producing a monodomain LCE. This method allows precise control over the molecular alignment, which is essential for achieving anisotropic behavior. It also provides greater flexibility in tuning the mechanical and actuation properties, as the molecular structure of the oligomers can be carefully designed prior to crosslinking. Both methods offer unique advantages and are chosen based on the desired level of customization, ease of fabrication, and application-specific requirements.

2.4.1 LCE Fabrication

LCEs can be synthesized using several techniques, applicable to both monomer- and oligomer- based methods:

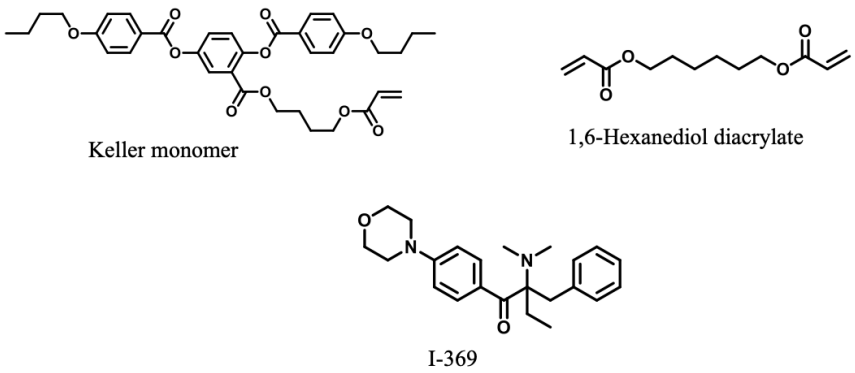

Figure 2.12: Chemical structures of Keller monomer, crosslinker 1,6-Hexanediol diacrylate and photoinitiator I-369

The classical method known as the two-stage crosslinking method or the Finkelmann method [43], involves an initial stage of loose crosslinking in the LC phase, which preserves the mesogens' natural anisotropic properties. This loosely crosslinked network is then mechanically stretched to align the director in a uniform direction, creating a monodomain structure. In the second stage, the network undergoes further crosslinking to lock in the aligned configuration, enabling the LCE to exhibit a two-way shape memory effect, causing reversible actuation. The second fabrication technique involves direct alignment and crosslinking in an anisotropic LC environment. Here, the mesogens are aligned using external stimuli or orientation techniques, such as surface alignment layers [44], external fields (electric or magnetic), photo-alignment layers [45] or flow-induced alignment through microfluidics [46]. Once the mesogens achieve uniform alignment, the polymerization and crosslinking processes are carried out using UV photoinitiators to lock in the structure. This approach eliminates the need for mechanical stretching, offering an alternative for creating uniformly aligned LCEs. While this approach is straightforward, it may face challenges with specific additives (e.g., azobenzene groups) that compete for UV light. Both techniques yield functional LCEs, but the two-stage crosslinking method is particularly favored for bulk samples and applications that require mechanical robustness and high actuation strain, as it enables precise control over the alignment throughout the thicker samples-something that can be more challenging with surface alignment alone.

The Keller monomer method exemplifies the use of photoinitiators to synthesize side-chain LCEs. In this approach, liquid crystal monomers with laterally fixed polymerizable side chains are combined with crosslinkers like 1,6-hexanediol diacrylate and photoinitiators such as Irgacure 369 (figure 2.12). The mixture at high temperature is introduced into specially prepared glass cells coated with alignment layers to promote uniform director alignment. The cell gap control the thickness of the resulting film. After filling, the sample is cooled into the nematic LC phase to allow the director to align properly. Polymerization and crosslinking are initiated by exposing the sample to UV light, locking the aligned structure into a solid elastomer [44].

Click chemistry methods, such as thiol-ene and thiol-yne reactions, have emerged as efficient and versatile approaches for LCE synthesis. These methods enable precise control over the network structure, reduced side reactions and ease in processing.

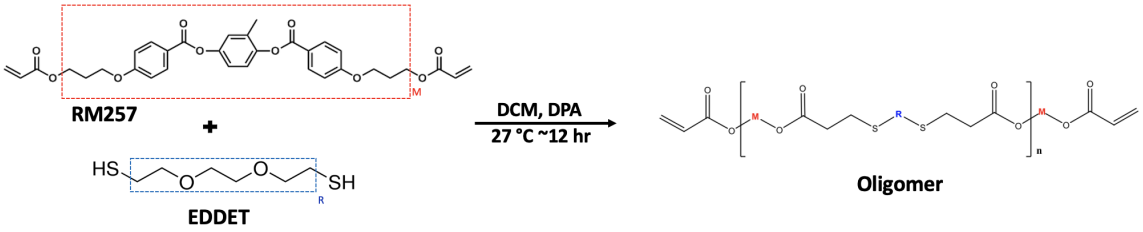

Figure 2.13: Synthesis of LCE Precursor (Oligomer) via Thiol-ene Michael Addition Reaction.

2.4.2 Thiol-ene Chemistry and click reactions for LCEs

Thiol-ene chemistry has emerged as a highly efficient approach for synthesizing LCEs, particularly in the oligomer-based framework. It leverages the "click" reaction between diacrylate LC monomer and thiols [47]. The reaction involves UV- or thermally-initiated addition of thiol (-SH group) to an activated alkene, often called a Michael acceptor, resulting in a more or less homogeneous network. Here, the thiol acts as the nucleophile, which attacks the β-carbon of the α,β-unsaturated carbonyl compound (acrylate). This results in forming a new -C-S- bond and generates a carbanion at the α-carbon of the acrylate. This carbanion is neutralized by abstracting a proton H^+ from either the original thiol or base, forming the final addition product. Thiol-Michael addition is either base or photo-catalyzed. Typically, tertiary amines are used in base-catalyzed reactions while in photo-catalyzed reactions, photoinitiators that form radicals upon exposure to appropriate light are used to facilitate the reaction. This reaction is regioselective, with thiol getting reacted to the least substituted β-carbon Michael acceptor. By varying the concentration of the thiol to the LC monomer, the molecular weight between crosslinks (M_c) can be varied. The magnitude and rate of thermomechanical responses in LCEs highly depend on the variation in (M_c) [48]. This method offers several advantages, including controlled conversion of functional groups, ensuring minimal defects in the network structure, and mild reaction conditions, often at room temperature.

The LCE synthesis that is mainly followed for our work is shown in figure 2.13. The LC monomer with acrylate ends is mixed with thiol, often with a catalyst or initiator, and is allowed to react at room temperature. The resultant oligomers are then aligned to ensure an approximate monodomain sample with desired orientation of the director. In our LCE tube fabrication, we use flow alignment using microfluidics, while in the azo-LCE sheet study, we use mechanical stretching to attain LC monodomains. This alignment is fixed by inducing crosslinking by UV or visible light curing.

2.4.3 LCE with azobenzene moieties incorporated

Conventional LCEs exhibit thermal actuation at elevated temperatures, limiting their application in biologically sensitive materials or environments. To overcome this challenge, researchers have been switching to light stimuli, as it offers several advantages: it requires low energy, allows precise control over the intensity and enables photoisomerization processes that are generally fast, selective and high yielding [49]. Photoactuation in LCEs can be categorized into photothermal and photochemical types depending on the mechanism by which the LCEs respond to light stimuli. In pho-

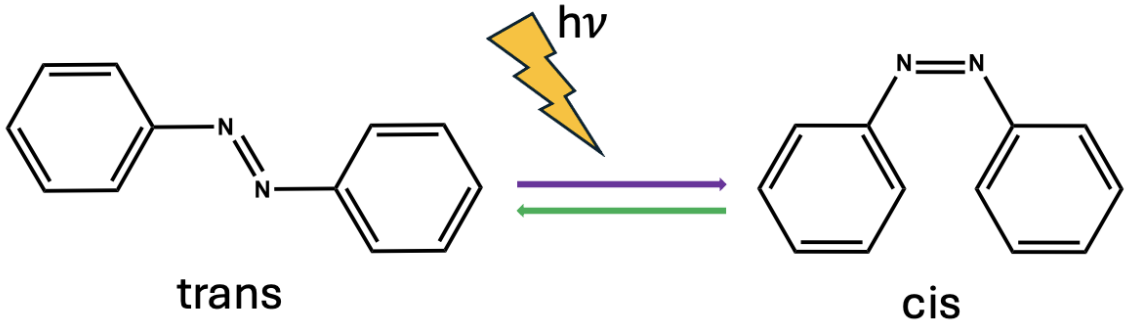

Figure 2.14: Photoisomerization in azobenzene, illustrating the reversible transformation of azobenzene between its trans and cis isomeric states under UV and visible light.

tothermal actuation, the light is absorbed by the material and converted into heat. This temperature rise is the reason for the disordering of the mesogens in LCE, most often triggering the transition to an isotropic state, leading to macroscopic shape changes. Light absorbers such as plasmonic gold nanoparticles [50], azo dyes [51] and CNTs [52] can be used in the LCE systems that utilize the photothermal effect for the actuation. In the photochemical effect, the phase transition occurs due to a reduction of the transition temperature caused by disturbance of the molecular ordering induced by a light-induced molecular shape change, thus even without a temperature rise.

Addition of photochromic moiety like azobenzene to LCs are of great interest because it can induce phase transition isothermally by undergoing photochemical reaction on ultraviolet irradiation. On exposure to UV, the *trans*- form of azobenzene can isomerize to *cis*--form. This *cis*-isomer can then return to the *trans*- form either thermally or photochemically (figure 2.14).The *trans*-form has a rod like structure that stabilizes the LC phase while the bent *cis*-form of isomer destabilizes the LC phase structure. This photo-isomerization disrupts the intermolecular order of the LC phase and causes a depression in the transition temperature (T_{NI}) of LC phase. As a result, the transition temperature of *cis* isomer system (T_{NIc}), is much lower than the transition temperature of the *trans* form (T_{NIt}).

The optimal temperature to use a photoactuated LCE that is solely driven by UV light is T_{NIc} which is the clearing temperature of the material specifically during UV exposure [15]. It is the lowest operating temperature at which the sample will have the highest degree of order prior to UV exposure, so that on UV exposure, the system can reduce its order to $S = 0$. If the operating temperature is set above T_{NIc}, then the order of the system is already reduced implying UV-induced reduction in order will be less significant, thus weakening the effect of UV light on the material. If the temperature is chosen below T_{NIc}, then the material has initial high order S before irradiation. However, in this case UV-irradiation cannot reduce S all the way to zero. Therefore, operating at T_{NIc} provides the best balance. It allows the material to begin with the highest possible order while enabling UV light to fully convert to isotropic phase, thus maximizing the material's response.

The π-conjugated system with an azo-linkage gives rise to strong electronic absorption in the UV or visible regions of the spectrum due to extended delocalization. However,

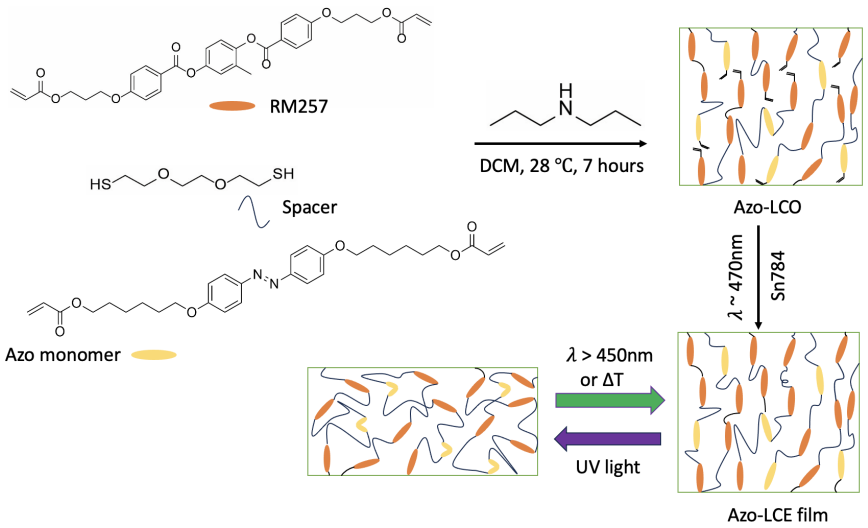

Figure 2.15: Chemical reaction for the production of photoresponsive main-chain azo-LCEs and schematic representation of of azo-LCE photoactuation.

they also have high tendency to π-stack- that is, a non-covalent interaction where planar aromatic systems align in a parallel, face to face manner, allowing overlap of delocalized π-electron clouds. Compared to biphenyls, azo compounds typically exhibit stronger π-stacking because the azo linkage (–N=N–) enforces molecular planarity and continuous conjugation which enhance stacking efficiency and stability. In contrast, biphenyls often adopt twisted conformations due to steric hindrance between ortho hydrogens, reducing $\pi - \pi$ overlap. As a result of this strong intermolecular stacking, azobenzene LC materials will exhibit LC phase at temperatures higher than required for industrial applications if not carefully designed, many having melting points reported higher than 100°C [53, 54]. The photoswitching between the *trans* and *cis* states in azobenzene occurs in microseconds with low-power light and is highly reversible, with the material able to undergo many cycles without significant fatigue, demonstrating long-term durability for practical use [55].

Doping azobenzenes into a liquid crystal (LC) matrix or film is a straightforward approach [56]; however, the resulting films frequently show instability, which can arise from phase separation or micro-crystallization. This instability is attributed to the mobility of the azobenzene within the film or matrix, as well as the tendency of the dipolar azo groups to aggregate. In order to attain stable, high-quality films, azobenzene chromophores are covalently bonded to the polymer network [57]. Figure 2.15 shows the chemical synthesis of main-chain azobenzene incorporated LCEs using oligomer method and the schematic representation shows photoactuation in these LCEs.

One major challenge in the synthesis of azo-LCEs is the interference between standard UV photoinitiators and the azobenzene groups present in the material. Azobenzene molecules absorb light in the same UV range that is typically used by many conventional photoinitiators. As a result, the absorption of UV light by the azobenzene groups leads to their photoisomerization, which consumes a substantial portion of the available light. This prevents the photoinitiators from receiving sufficient energy to generate the necessary radicals, resulting in incomplete polymerization and

crosslinking. Additionally, the reversible *cis-trans* isomerization of azobenzene can occur prematurely during synthesis, disrupting the uniform alignment of the director to form monodomain network. These factors complicate the achievement of a fully cross-linked network with reliable mechanical and actuation properties. To address these challenges, researchers must carefully optimize the light exposure conditions, select photoinitiators with visible-light activation, or modify the composition of the azo-LCE to reduce interference and ensure successful polymerization.

2.5 Bio-application of LCEs: A focus on organoids

The synthetic strategies outlined above have enabled the design of LCEs with precisely tunable mechanical and optical properties. The combination of thiol-ene chemistry and azobenzene incorporation provides dynamic responsiveness, making these materials particularly attractive for bioengineering applications. In recent years, there has been growing interest in applying smart materials to modulate biological environments. For example, in the work by Gao et al., they demonstrate the development of novel 3D LCE foams as biocompatible cell scaffolds [58]. These scaffolds feature interconnected porous channel networks that significantly enhance cell proliferation and promote spontaneous cell alignment. Such characteristics are highly valuable for guiding tissue organization and suggest strong potential for using LCEs in advanced biofabrication.

Building on these insights, this thesis focuses on exploring the application of LCEs in the context of organoids: in vitro three-dimensional (3D) tissue models that mimic the architecture, functionality, and key characteristics of their original tissue. These structures are derived from stem cells or progenitor cells that self-organize and differentiate into organ-like structures under appropriate culture conditions. Due to its ability to resemble organogenesis (the process during early development in which embryonic cells differentiate and organize into specific organs and tissues of the body) with its complexities to a greater extent, organoids serve as a powerful tool that bridges between two-dimensional cell cultures and animal models, providing a platform to explore human development, disease mechanisms, and personalized medicine [59].

Organoids recapitulate most of the aspects of cell differentiation based on the self-organizing tendency of stem cells. By providing biochemical and biophysical cues in a controlled 3D environment, cells can mimic key processes such as cell sorting and lineage-specific differentiation [60]. To guide cells into forming organized structures, small molecules, growth factors, or physical constraints are introduced to simulate the chemical gradients and reaction-diffusion processes seen in the body. These factors cause localized growth, cell sorting, and specific cell behaviors, which ultimately lead to the formation of organ-like structures.

Organoids can be developed using two main approaches: directed or undirected differentiation. In directed differentiation, stem cells are guided into specific types, such as ectoderm, endoderm, or mesoderm (the three primary layers of cells in early development), by adding specific molecules and growth factors. This results in a specific cell type or tissue. In contrast, undirected differentiation lets cells decide their fate without external signals, allowing more randomness and variability. This second approach is especially useful for studying more complex systems, such as the human

central nervous system (CNS), because it reflects the natural diversity of cell behavior. Depending on the culture conditions and cell type, organoids can model tissues ranging from the brain and intestine to the liver and kidney [61].

One of the greatest potentials of organoids is the ability to study human development and thus unravel the molecular mechanism behind human-specific diseases (polygenic, monogenic, or infectious) [62]. Organoid cultures that recapitulate most of the developmental process that occurs in vivo, combined with novel imaging techniques enable the visualization of human developmental process in real time. Using direct differentiation techniques, organoids for specific organs can be grown, making it possible to develop personalized cell therapies or gene correction strategies. Diseases like Alzheimer's and Parkinson's, which were hard to study before due to their late onset, can now be studied in 3D cultures [63, 64]. Organoids also help in understanding stem cell behavior, tissue repair, and drug testing before clinical trials [65].

2.5.1 Current limitations in organoid growth

Organoids being an exciting and promising tool, possess challenges to be addressed as well. First, 3D ensembles are only approximation of tissues and the internal cell structure is not always predictable or physiologically accurate. Although they follow developmental pathway similar to those in vivo, their size and organization vary from the real cell system [61]. Studies show that the standard culturing conditions reduce the heterogeneity of organoid population and tend to form more uniform structures. Therefore, they have to be tested for accuracy [66]. Furthermore, scalable and safe organoids are crucial in drug screening and regenerative medicine. Also, reproducibility remains a key issue. Organoids within the same culture often show significant variability in size, viability, organization, and functionality, which complicates phenotype screening and large-scale applications.

Another significant limitation of organoids is their lack of vascularization. As a result, nutrients and oxygen can only reach the cells by passive diffusion. This slow process limits how far the nutrients and oxygen can penetrate the organoid, limiting their growth and long-term viability beyond a few hundred micrometers in size [67]. This creates a gradient of metabolic activity where cells closer to the surface receive adequate nutrients, while those deeper within the organoid are prone to hypoxia (lack of oxygen) and necrosis (cell death) as shown in figure 2.16. Without vascularization, it becomes challenging to mimic the in vivo environment accurately, as the exchange of nutrients, oxygen, and signaling molecules through blood vessels is a critical aspect of tissue physiology. The elimination of cellular metabolic byproducts is equally crucial for maintaining cell survival [68]. Efforts are made to address this limitation, including co-culture with endothelial cells, bioprinting of vascular networks, and integration with microfluidic systems, to replicate the complexity of natural tissues better. However, these approaches remain in the experimental stage and require further development for widespread application.

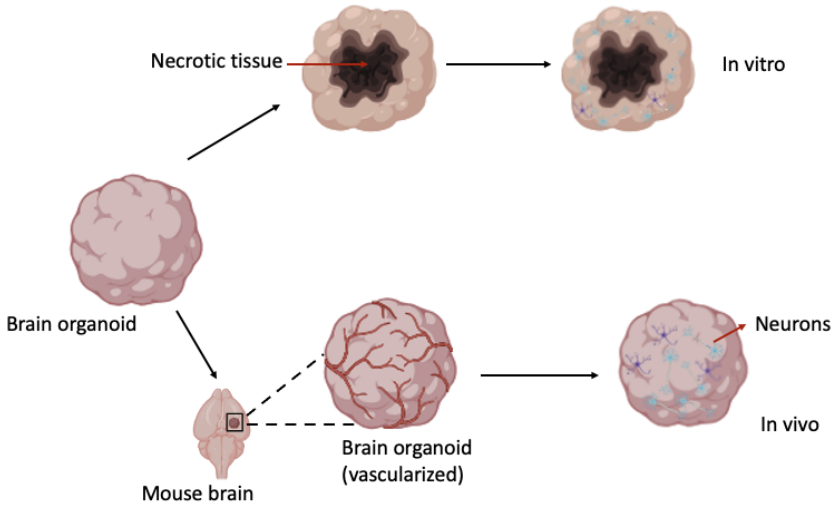

Figure 2.16: Schematic showing the growth of brain organoids in vitro and in vivo. In vitro, organoids lack vascularization, leading to hypoxia and central necrosis. Organoid if transplantated into a mouse cortex, enables vascularization improving nutrient supply, oxygenation, and neuronal differentiation at surface and core resulting in healthier and functional organoids. Drawn using BioRender scientific illustration software.

Chapter 3

Experimental setups and protocols

3.1 Microfluidic device fabrication

A nested capillary setup was employed to fabricate LCE tubes and fibres. Long cylindrical capillaries with an outer diameter 1 ± 0.01 mm were selected for constructing the devices. One end of each capillary was tapered using a micropipette puller (p-100, Sutter Instrument). The taperred end was then cut to the desired orifice size (90-150 μm for the inlet and 300-350 μm for the outlet) using a microforge (Narishige, MF-900). To ensure a smooth finish, the cut capillary tips were polished by gently rubbing them on fine sandpaper.

The cylindrical inlet and outlet capillaries were inserted into a square capillary with a side length of 1 ± 0.01 mm (from CM Scientific). The outer diameter of the cylindrical capillaries was matched with the side length of the square capillary chosen to ensure a proper fit in the nested setup. For assembly, the square capillary was glued onto a glass slide at both ends to fix its position, and the tapered cylindrical capillaries were inserted from opposite sides as shown in figure 3.1a .

To ensure proper alignment, the inlet tip is centered within the diameter of the outlet orifice. This is visualized using a microscope as shown in figure 3.1b. A spacing of 100-150 μm was maintained between the inlet and the outlet tips, forming a junction where the three fluids meet before jet formation. Once the alignment was confirmed, the other end of inlet capillary is sealed with a blunt needle (21 gauge and 2.2 cm in length) using epoxy glue. Similarly the spacing between the square capillary and the inlet capillary is also sealed using a second blunt needle. The non-tapered end of the outlet is left open to connect a collection tube, while the spacing between outlet and square capillary is sealed with a third blunt needle. The device (figure 3.1c) is then left to dry overnight to ensure the epoxy glue set properly.

In the completed setup, the inner cylindrical capillary (inlet) delivered the core polymer solution, forming the internal lumen of the tube. The LCE precursor solution flowed through the gap between the inlet capillary and the square capillary, while the outer polymer solution flowed in the opposite direction through the gap between the outlet and square capillary. The flow rates of the fluids were adjusted using syringe pumps to achieve the desired tube geometry and thickness.

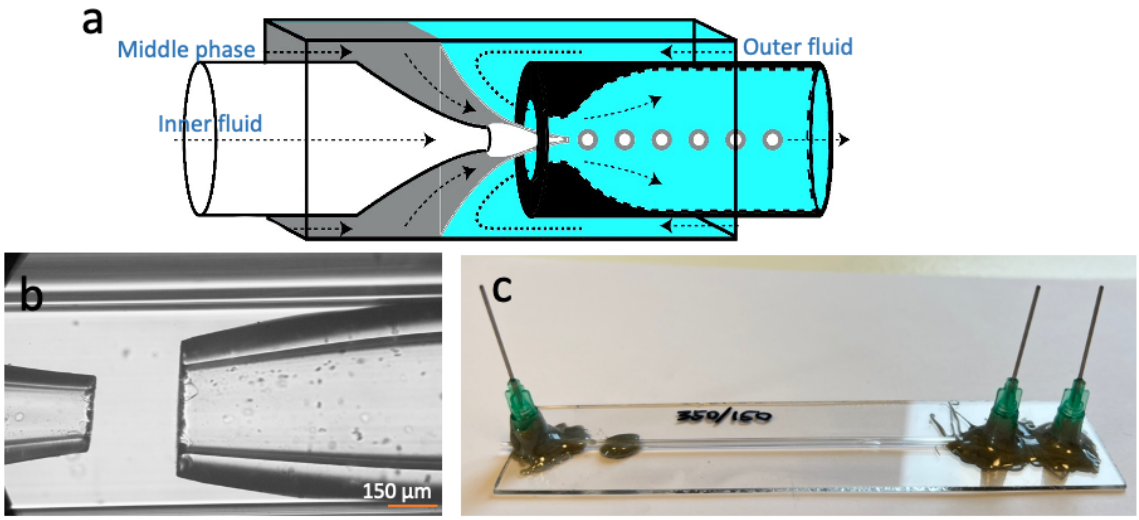

Figure 3.1: a) Schematic drawing of nested capillary set-up. b) Microscopic image of the device junction where the inlet capillary is centered within the diameter of the outlet capillary orifice viewed without analyzer. c) Macroscopic image of the microfluidic device.

3.2 Syringe pump and accessories

In this project CETONI syringe pumps were used to ensure precise and accurate flow rates. The syringes were securely attached to the pump base through leak-proof fittings. The CETONI Elements software was used to calibrate the syringes, program flow rates, and monitor real-time performance. The software supports multichannel synchronization, allowing simultaneous control of all three fluid flows.

Luer lock fittings at the syringe ends connect to PTFE tubes, which are attached to the needles of the microfluidic device for each phase. The microfluidic device is placed on the stage of an inverted POM microscope. The device junction is visualized through a Phantom camera connected to the microscope, which is operated using the Phantom Camera Control (PCC) software application.

3.3 UV LED mount

The insitu polymerization of LCE tubes and fibres were carried out using Dymax BlueWave® QX4 V2.0 LEDs spot curing system, which comprises a controller and four LED heads. The 365 nm wavelength LED heads were used to match the photoinitiator used in the LCE system. Each LED head delivered an intensity output of 16.9 W/cm^2 at 4 cm, ensuring effective curing for the experiments.

The UV LED mount, shown in figure 3.2a, was custom-designed and 3D-printed by our technician, Robert Himelrick. This mount securely holds the four UV LEDs while providing a stable platform for the microfluidic device during experiments. The design features four cylindrical holders with precisely measured inner diameters to fit the UV LED heads snugly. Small holes in each holder allow the LEDs to be secured using screws. The holders are positioned at a 45° angle to each other, ensuring uniform UV exposure at the localized region of the microfluidic device.

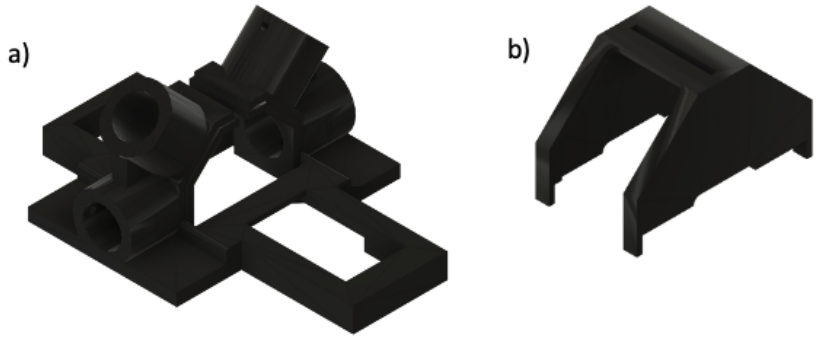

Figure 3.2: 3D print sketch of: a) UV holder, b)lid for the holder with observation slit.

The base of the mount includes a rectangular platform designed to support the microfluidic device. Two large rectangular cutouts in the base allow an unobstructed view of the microfluidic junction, enabling the inverted microscope lens to focus on the junction or the capillaries during operation.

To enhance safety and functionality, a protective lid was designed for the mount shown in figure 3.2b. The lid is positioned to ensure that UV light only illuminates the downstream region of the microfluidic device, approximately 6 cm away from the jet formation. This precise position prevents unwanted curing or clogging near the device junction. The angled and enclosed structure of the lid minimizes stray UV light exposure, ensuring protection for both users and surrounding components during operation.

3.4 Synthesis of light-insensitive LC oligomers

The synthesis of liquid crystal oligomers, LCO1 and LCO2, were performed using a one-pot method adapted from He et al. [69]. To synthesize LCO2, 1,4-bis-[4-(3-acryloyloxypropyloxy)benzoyloxy]-2-methylbenzene (RM257) (6.0 g, Wilshire Technologies, 95%) and 2,2'-(ethylenedioxy)diethanethiol (EDDET) (1.66 g, Sigma-Aldrich, 95%) were combined in a 1.1:1 molar ratio. This mixture was dissolved in 23 mL of dichloromethane (DCM) (Carl-Roth, $\geq$ 99.8%). In the synthesis of LCO1, the thiol cross-linker EDDET was replaced with 1,6-hexanedithiol (HDT, Sigma-Aldrich, 96%) while maintaining the same molar ratio to RM257. To initiate the reaction, 0.09 g of dipropylamine (DPA, Sigma-Aldrich, 99%) was added drop wise as a catalyst. The reaction mixture was stirred at room temperature for approximately 12 hours, after which the solvent was removed using a rotary evaporator.

3.5 Synthesis of light sensitive LC oligomers

Azo-LC oligomers with EDDET

In the one-pot synthesis of preparing 6-azo-LCO, RM257 (1.8 g) and 6-azo 4,4'-bis(6-acryloyloxyhexyloxy) azobenzene (0.2 g, 10 wt% of RM257)) were dissolved in 23 mL of DCM. To this mixture, EDDET (0.56 g) was added. The acrylate to thiol molar

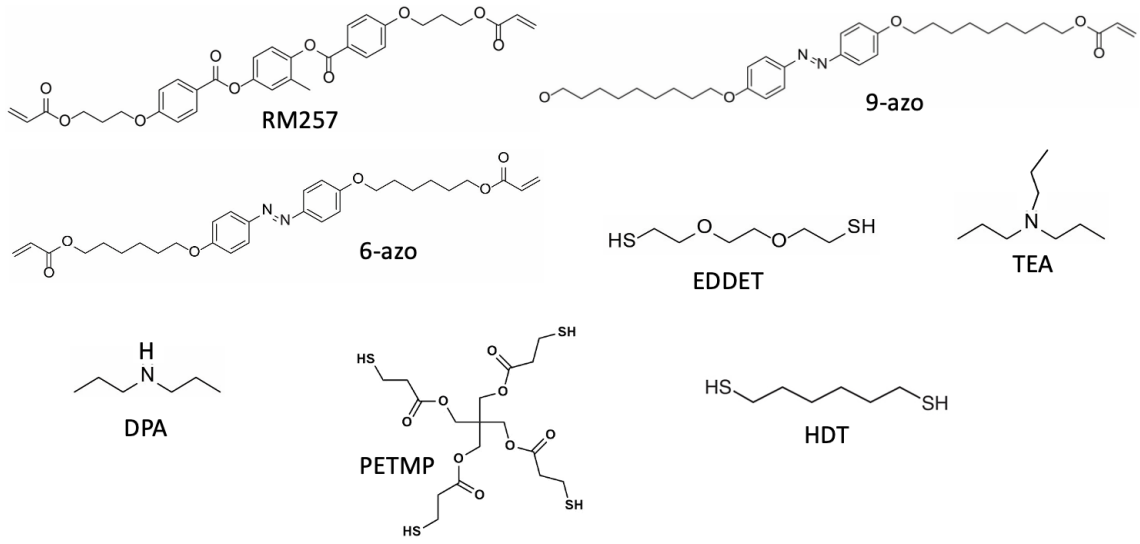

Figure 3.3: Chemical structures of monomers, chain-extenders, crosslinkers, and catalysts used in the synthesis of light-insensitive and light-sensitive LCOs/LCEs.

ratio is maintained as 1.1:1. 0.03 g of the catalyst DPA is added dropwise to the above mixture. In the synthesis of 9-azo-LCO, the azobenzene moiety was replaced with 9-azo (4,4'-Bis(9-(acryloyloxy)nonyloxy)azobenzene (0.2 g, 10 wt% of RM257)). The solution was then stirred at room temperature for about 7 hours.

Azo LCEs from azo-LCO and PETMP

Two thiol-Michael addition reactions were employed in this method. At first, 6-azo (0.2 g, 0.00038 moles), RM257 (1.8 g, 0.003 moles) and, EDDET (0.568 g, 0.003118 moles) were dissolved in 6 mL of DCM. To this solution 0.09 g of triethylamine (TEA, Sigma-Aldrich, 99%) was added dropwise as catalyst, and the reaction mixture was stirred for 48 hours at 25°C. The molar ratio of diacrylate to thiol is maintained at 1.1:1 to obtain acrylate-ended oligomers. The solvent is then evaporated using rotary evaporator to obtain the oligomer.

To the above oligomer, 4 wt% of Sn784 was added. Then to 2.5 g of the LCO-Sn784 mixture, 1 mL of DCM was added. The tetra-thiol crosslinker, pentaerythritol tetrakis(3-mercaptopropionate) (PETMP, 0.356 mmol, 6.5 wt% with respect to the oligomer) and TEA (3.5 wt% with respect to the oligomer) is dissolved in 0.5 mL of DCM and is added to the LCO mixture, which is then mixed well with a shaker. The resulting mixture is then immediately barcoated on to a PVA coated glass slide. The second thiol-Michael addition reaction occurs now when the coated slides are left in the oven to cure at 70°C for 16 hours.

All the chemical structures used in the synthesis of both light-insensitive and light-sensitive LCOs and LCEs are shown in figure 3.3.

3.6 Microscopy

3.6.1 Polarized Optical Microscopy(POM)

In this thesis, the Olympus (BX51) and Nikon inverted POM (ECLIPSE TS100) microscopes were extensively used. The Olympus microscope primarily facilitated all sample analyses, while the Nikon inverted microscope supported LCE tube or fiber production. In certain cases, I inserted a wave plate into the Olympus microscope and used it primarily in a cross-polarized configuration. An Olympus camera (DP73), mounted on the microscope, captured and recorded the observations.

All analyses were performed with the Olympus microscope in transmission mode. In this setup, unpolarized light from the source passed through the polarizer, traversed the sample, and then moved through the objective lens. The polarized light subsequently traveled to the analyzer and reached either the eyepiece or the camera. During tube production, I used the inverted microscope. Its light source, mounted at the top, directed light through the sample to the objective lens at the bottom. From there, the light continued to the eyepiece or the camera.

The core principle of POM relies on the interaction of plane-polarized light with a birefringent material. The plane-polarized light from the polarizer, on reaching the anisotropic specimen (LC), splits into two rays: the ordinary wave and the extraordinary wave. These waves experience different refractive indices. As a result, they travel at different velocities, leading to a phase difference between them when they emerge from the specimen. These out-of-phase waves leaving the sample are then recombined with constructive and destructive interferences, providing detailed information about the material's structure and optical properties. An analyzer, placed orthogonally to the polarizer, further enhances the contrast of the interference patterns by only transmitting the component of light that is aligned with its transmission axis.

3.6.2 Scanning Electron Microscopy(SEM)

SEM (JEOL JSM-6010LA) was employed to investigate the surface morphology and structural features of the LCE tubes. Unlike optical microscopes that use visible light with wavelengths in the range of 400-700 nm and are limited to a resolution of $\approx 200\ nm$,, SEM scans the sample surface using a focused beam of high energy electrons. These electrons have much shorter wavelengths-on the order of picometers-allowing SEM to resolve features at the nanometer scale, far beyond the diffraction limit of light. When the electron beam interacts with the sample surface, it generates various signals that are collected to form highly detailed images. The imaging process requires the sample to be conductive or coated with a thin conductive layer to prevent charging under the electron beam. Non-conductive samples accumulate charges when exposed to the electron beam, leading to image distortions or loss of detail. To address this issue, the non-conductive LCE tubes were coated with a thin layer of gold (2 nm layer thickness), providing a conductive surface that dissipated the accumulated electrons and ensured accurate imaging.

3.7 Other instruments and softwares used for characterization

3.7.1 Uv-vis spectroscopy

The Ultrospec 2100 Pro UV-Visible spectrophotometer was utilized for recording the absorption spectra of azobenzene moieties in both solution and thin film samples to investigate the photo-isomerization in azo-LCOs and LCEs. The technique employs the measurement of light absorption in the ultraviolet and visible regions to monitor electronic transitions in molecules.

3.7.2 Differential Scanning Calorimetry (DSC)

DSC measurements were performed using a DSC823 instrument (Mettler Toledo, USA) to analyze the thermal properties of the samples. Approximately 15 mg of each sample was loaded into the DSC pans. DSC measures the difference in heat flow between the sample pan and an empty reference pan as both are subjected to the same controlled temperature program. When the sample undergoes a thermal transition, such as melting or glass transition, it absorbs or releases heat, which shows up as a difference in heat flow compared to the reference.

The samples were initially cooled to -40° C at a rate of -5° C/min, followed by heating to 90° C at a rate of 5° C/min to acquire the first heating data. The sample was then cooled back to -40° C and reheated to 90° C to obtain the second heating data. The first cycle captures any effects of the thermal history, while the second provides a more accurate view of the intrinsic behavior of the material.

In the DSC data, the glass transition appears as a step change in the baseline due to a shift in heat capacity. Crystallization shows up as an exothermic peak during cooling, as heat is released when ordered structures form. Melting or nematic-to-isotropic transitions appear as endothermic peaks during heating, as the material absorbs heat to move into a more disordered phase. This procedure enabled the observation of thermal transitions such as glass transition, crystallization, and nematic to isotropic transition, providing valuable insights into the material's thermal behavior and stability.

3.7.3 Infrared spectroscopy

Infrared (IR) spectroscopy was used to analyze the vibrational spectra of the samples, providing information on their molecular structure and functional groups. The measurements were performed using a Nicolet iS5 FT-IR spectrometer equipped with a diamond crystal in attenuated total reflection (ATR) mode. This setup allowed for direct analysis of the samples without extensive preparation.

Vibrational spectra were recorded with transmission on the y axis and wave numbers ranging from 550 to 4000 cm^{-1} on the x axis. A total of 16 scans were performed for each sample to ensure a high signal-to-noise ratio, and the final spectra were averaged from these scans. The resolution was set at 4 cm^{-1}, allowing the detection of fine spectral features and providing precise information about the chemical composition and bonding environment of the sample.

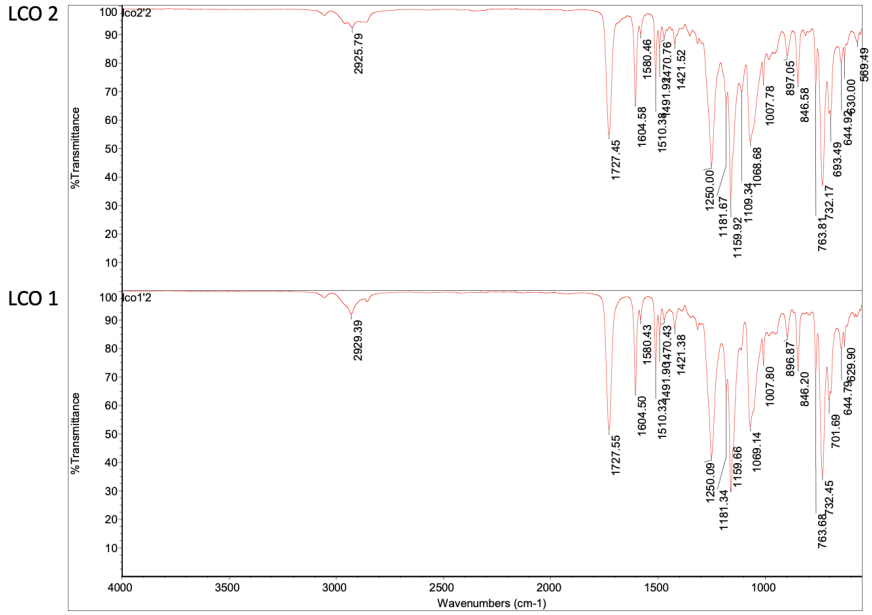

Figure 3.4: IR spectra of LCO1 and LCO2 oligomers. Reproduced from [70]

In IR spectroscopy, wavenumber is commonly used instead of wavelength as the x-axis. Wavenumber is defined as the reciprocal of the wavelength in centimeters ($\tilde{\nu} = \frac{1}{\lambda}$), and its unit is inverse centimeters (cm^{-1}). This unit is particularly convenient because it is directly proportional to the energy ($E = hc\tilde{\nu}$), making it easier to interpret vibrational transitions, which typically occur in the mid-IR region. Using wavenumber provides a straightforward way to compare vibrational modes and observe shifts related to changes in molecular structure.

Confirmation of excess acrylate ends in LCOs

IR spectra shown in Figure 3.4 for LCO1 and LCO2, confirmed the thiol-ene reaction has been complete. The absence of free thiol group represented by absence of peaks at 2600-2500 cm^{-1} confirms that all EDDET has reacted with RM257 in the system. Peaks observed at 885-800 cm^{-1} signifies the C-H bending vibrations from the acrylate group. However, the expected peak for the (C=C) stretching vibration of the acrylate group around 1635 cm^{-1} is not observed. One possible reason for not observing it could be the specific molecular environment of the terminal acrylates in these oligomers, which might affect the vibrational dipole moment of the (C=C) stretch, making it harder to detect. Despite not being detected here, I am confident that excess terminal acrylates are present, as they successfully participated in photopolymerization reactions later, leading to the formation of crosslinked elastomers.

3.7.4 Matlab for width determination of LCE sheets

With the help of my colleague Alejandro Ibarra, a MATLAB code was written to determine the width of the azo LCE sheets to study photoactuation. The code starts by isolating the blue channel from the uploaded RGB images, as this channel provided the most accurate detection of object boundaries. Using the bwboundaries function, the code identifies the contours of objects in the image, selecting the largest one

based on the number of boundary points. After locating the boundary, the centroid (geometric center) of the object is determined by averaging the boundary points. Distances between the centroid and all boundary points are then calculated, enabling the identification of key points along the boundary, such as the closest point to the centroid and additional points at 90-degree intervals. The object's width is determined by measuring the distances between the centroid and these key boundary points. Specifically, the code calculates the width by summing these distances at the 90-degree intervals. These measurements are subsequently used to analyze the behavior of the LCE sheet under various conditions.

To estimate the error bars in the relative width ratio measurements, the code accounts for two main sources of uncertainty. First, there is an estimated 1% error in the conversion of pixel measurements to millimeters. Second, potential inaccuracies in identifying boundary points introduce an error, which is approximated as a deviation of up to two pixels. These uncertainties are combined to calculate the total error in the width measurements. The combined uncertainty is then propagated when computing the ratios of each width measurement relative to the reference width.

Chapter 4

Arbitrarily long tubular LCE as peristaltic pump actuators

This chapter presents the successful fabrication of long polymerized LCE tubes, achieved through establishing stable, continuous tubular flows within a microfluidic setup. This work holds potential for applications such as peristaltic pumps in organoid systems. Published in the journal "Small" [70], this work combines contributions from both me and Nikolay Popov, with each result reflecting a collaborative effort. The experimental approaches and outcomes shared here align with our publication, highlighting the LCE tube's fabrication, characterization, and suitability for integration with biological environments.

4.1 Continuous stable tubular flow

In this study, a triple-phase coaxial microfluidic setup is modified to produce LCE tubes of arbitrary length (figure 4.1b). The inner aqueous phase was flown through the inlet, while the LCE precursor solution flowed as the middle phase between the inlet and the square capillary, both phases moving in the same direction. Both these phases at the junction encounter the outer aqueous phase flowing oppositely between the outlet and the square capillary. The outer phase exerts flow-focusing on the inner and middle phases, enabling a steady tubular flow to form.

Laminar flow is usually observed in microfluidic channels. The flow patterns in different flow situations are predicted by Reynold's number(Re) [71]. It relates inertial

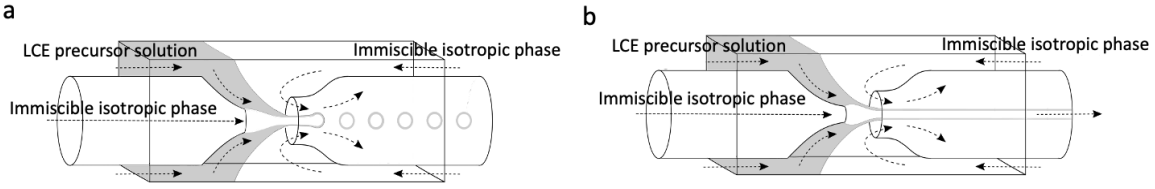

Figure 4.1: Schematic of Microfluidic Production Process for a) LCE Shells and b) LCE tube using a coaxial nested capillary set-up. Reproduced from [70]

forces to the viscous forces and is given by:

$$Re = \frac{\rho\, v\, L}{\mu} \tag{4.1}$$

where: ρ is the fluid density (kg/m^3), v is the flow velocity (m/s), L is the characteristic length (m) and, μ is the dynamic viscosity (Pa·s). At lower Re (<2000), the viscous forces dominate and laminar flow is observed. Turbulent flows are observed for Re = 2000-4000 and are generally not observed in microfluidic channels. Interfacial tension and capillary forces significantly influence fluid flow manipulation in microfluidic systems. Interfacial tension greatly impacts overall fluid dynamics due to the high surface-to-volume ratio inherent in microscale systems.

4.1.1 Interfacial tension

Interfacial tension is the surface tension specifically used when the boundary is between two different fluid phases. It is the free energy per unit area required to create an interface between two immiscible liquid phases [72]. This arises due to the imbalance between intermolecular forces at the interface, leading to a tendency to minimize the surface area. Interfacial tension is denoted by γ and is given by:

$$\gamma = \frac{F}{L} \tag{4.2}$$

where: F is the force acting on the interface, and L is the length over which the force is acting.

The strength or magnitude of the interfacial tension depends on the nature of the fluids in contact, temperature, surfactants, or other agents that can reduce the surface tension by stabilizing the interfaces. It plays a significant role in multiphase flow and in determining flow regimes, pressure drops, and fluid distribution. At lower interfacial tensions, fluids tend to easily mix, while higher interfacial tensions tend to phase separate fluids, leading to distinct fluid layers. Capillary number (Ca) is often used to relate viscosity to interfacial tension and is given by:

$$Ca = \frac{\mu U}{\gamma} \tag{4.3}$$

where: μ is the dynamic viscosity, U is the velocity, and γ is the interfacial tension. When the Capillary number is low, interfacial tension dominates, creating a dripping regime, while when Ca is high, the viscous forces overcome interfacial tension, promoting jetting [73]. In microfluidics, Ca is typically low, and interfacial tension has a high impact on flow patterns and fluid behavior.

4.1.2 Dripping to jetting transition

In microfluidics, we take advantage of the hydrodynamic instability by flowing one liquid into another immiscible liquid to form two distinct regimes: the dripping or jetting regime. In the dripping regime, drops are formed due to a balance between the surface tension and the viscous drag of the coaxial fluid pulling it downstream [74]. Here, the surface tension dominates over the viscous and inertial forces, leading

to drop pinch-off. In contrast, in the jetting regime, the fluid forms a continuous jet extending downstream of the orifice of the injection capillary. This occurs when the inertial forces of the fluid flow dominate over surface tension, allowing the liquid to maintain a continuous stream rather than breaking up into droplets. This jet eventually breaks down into droplets due to Rayleigh-Plateau instability [75]. This can be described as the breakage of a jet or stream of fluid into droplets due to surface tension. Suppose a small disturbance or perturbation occurs over the stream of flow. In that case, it will increase the Laplace pressure within the thinner region of the jet and push the fluid to either side, causing the region to become even thinner and ultimately break into drops [76]. Laplace pressure is the pressure difference across the interface of a curved surface such as bubbles or droplets due to surface tension [77]. In a drop, the pressure inside is higher than the pressure outside due to the surface tension acting to reduce the surface area. The dripping-to-jetting transition is governed by several parameters, including the capillary number (Ca), Weber number (We), flow rates of the fluid phases, and the channel geometry and dimensions. As the Ca number increases, the viscous forces dominate compared to surface tension, and the system tends to transition from dripping to a jetting regime. Weber number is the ratio of inertial forces to surface tension forces and is given by:

$$We = \frac{\rho U^2 D}{\gamma} \tag{4.4}$$

where: ρ is the density of the fluid, U is the velocity, D is the diameter of the orifice or channel, γ is the surface tension between the two phases. At higher We, inertial forces of the fluid overcome the surface tension, favoring the formation of a stable jet [78]. In my experimental setup, the system operates in the jet regime to give continuous long tubular flow, with careful tuning of the fluid phase flow rate, selection of the different fluid phases, and channel geometry.

4.2 Choice of LCO mixture and polymer solutions

Aqueous phase and middle phase preparation

All polymer solutions were prepared at a 10 wt% concentration by dissolving commercially available polyvinylpyrrolidone (PVP, $M_w = 1.3 \cdot 10^6$ g/mol) and poly(acrylic acid) (PAA, $M_w = 4.5 \cdot 10^5$ g/mol) in distilled water. These solutions were stirred at 80°C for two days to ensure complete dissolution. The prepared PVP and PAA solutions along with 2 wt% of surfactant Tween 20 were used as the inner and outer phases, respectively, to form isotropic solutions suitable to flow through the microfluidic device.

For preparing middle phase, the LCOs were synthesized with excess acrylate end to ensure that there is enough reactive ends for the potocrosslinking during tube production. Although the LCOs exhibit a nematic phase at room temperature, their viscosity is too high to flow through microfluidics. For this reason they were dissolved in DCM at a concentration of 33-40%, giving a solution that is viscous enough but not too resistant to flow in microfluidic device. To complete the LCE precursor solution, 4 wt% of the photoinitiator Irgacure 819 (Ciba, >95%) was added, along with 2 wt% of the surfactant Span 80 (Fluka). Since we use solution of LCO in DCM, we now

have an isotropic state rather than nematic state. This DCM has to be removed from the LCO at later stage to obtain nematic LCE tubes.

4.2.1 Reducing interfacial tension

By increasing viscosity

One of the major constraints while using this setup is to overcome the droplet or shell formation by the coaxial jet of the inner phase and LCE precursor due to Rayleigh-Plateau instability [79]. This can be achieved by increasing the viscosity of one or both of the immiscible liquid phases. An increase in viscosity causes greater resistance to perturbations. In other words, any deformation or disturbances at the interface are dampened as the viscous force counteracts the surface tension forces that drive these instabilities.

In this study, inner and outer phases were chosen as 10 wt% aqueous solution of high molar mass polymers (PVP And PAA) that exhibit strong non-Newtonian properties [80]. Non-Newtonian fluids are fluids that do not follow Newton's law of viscosity. Their viscosity can change when shear stress or strain is applied. Highly viscous LCO solution (33 wt% of LCO1 in DCM) is used as the middle phase. Polymer chain entanglements in the isotropic state, along with the high viscosity of the LCO solution, work together to reduce interfacial tension. This combined effect minimizes any interface perturbations and effectively delays the onset of Rayleigh-Plateau instability. With PVP solution as inner and outer phase, a stable coaxial jet of upto 1 cm is seen in figure 4.2a. While with PAA solution as inner and outer phase, the coaxial jet collapses to shell within 2 mm due Rayleigh-Plateau instability but the LCE precursor jet is seen to extend 1 mm further (figure 4.2b). This early breakage of coaxial jet can be due to the low molar mass of PAA compared to PVP as well as the high persistence length of PAA due to it's nature as a polyelectrolyte. Polyelectrolytes are polymer chains that can dissociate into ions in solvents, giving rise to a charged chain. This results in Coloumbic repulsion between like charged chain segments, causing the polymer to stretch out and become stiffer.These aspects of PAA causes less effective delaying of Rayleigh-Plateau instability.

To address this coaxial breakage, a co-solvent, acetic acid, was added to the PAA solution. The idea of adding a co-solvent to the inner and outer phase is that, since it is soluble in both the immiscible phases-DCM and aqueous phase, it can diffuse from one phase to its neighbor phase, causing the interface to blur which in turn diminishes the interfacial tension and thus stabilizing the interface for stable flow as reported in [81]. Additionally, acetic acid's miscibility in DCM provides the advantage of facilitating the extraction of DCM from the LCO phase into the surrounding aqueous phases, a process favorable for promoting the nematic phase formation in the LC system.

This approach has helped to extend the coaxial jet up to 5 cm downstream from the jet's origin as illustrated in figure 4.3a. However, the PAA solution is turbid and very viscous and contrary to the expectations, the acetic acid did not extract DCM sufficiently to induce nematic ordering within the middle phase. Consequently, further experiments with PAA solution were not carried out.

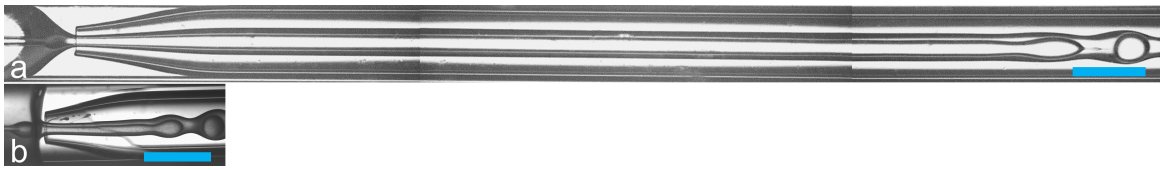

Figure 4.2: Comparative analysis of coaxial jet stability using a) 10 wt% PVP and b) PAA aqueous solutions as inner and outer phases, where 33 wt% of LCO1 in DCM is used as the middle phase in both the cases. The experiment is carried out at ≈ 22°C and the volumetric flow rates used are a) $\phi_i = 4.0$ mL/h, $\phi_m = 3.0$ mL/h and $\phi_o = 8.0$ mL/h and b) $\phi_i = 8.0$ mL/h, $\phi_m = 5.0$ mL/h and $\phi_o = 10.0$ mL/h. Panel (a) provides an approximate representation of the complete jet length, created by stitching together several frames from the tube production video while the device was moved along the tube. [Scale bar: 1mm] Reproduced from [70].

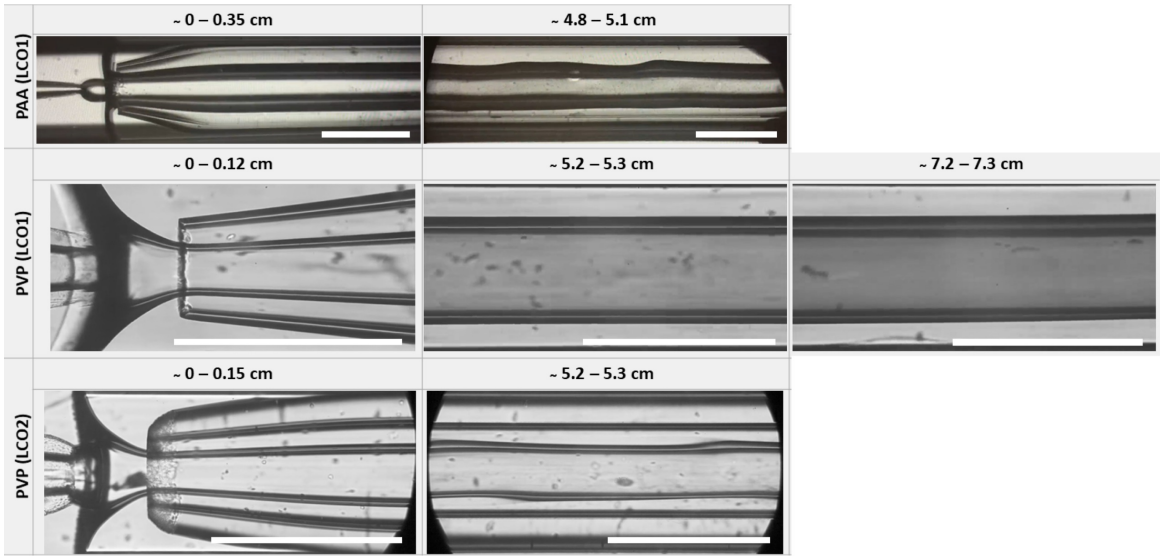

Figure 4.3: Coaxial jet extension observed using different isotropic aqueous phases with LCO precursor solutions. a) Configuration with 10 wt% PAA solution in a solvent of 90 wt% water and 10 wt% acetic acid as inner and outer phases, with a 40 wt% LCO1 solution in DCM as the middle phase. b) and c) Configurations using 10 wt% PVP solution with 2 wt% Tween 20 as inner and outer phases; the middle phase is 40 wt% of either LCO1 (b) or LCO2 (c) in DCM, with 2 wt% Span 80 added. The experiments are carried out at room temperature (∼ 22°C) and the volumetric flow rates are (top) $\phi_i = 10$ mL/h, $\phi_m = 5$ mL/h and $\phi_o = 13$ mL/h; (middle) $\phi_i = 7.5$ mL/h, $\phi_m = 5$ mL/h and $\phi_o = 10$ mL/h; and (bottom) $\phi_i = 5$ mL/h, $\phi_m = 2.5$ mL/h and $\phi_o = 6$ mL/h, respectively. [Scale bar is 1 mm]. Reproduced from [70]

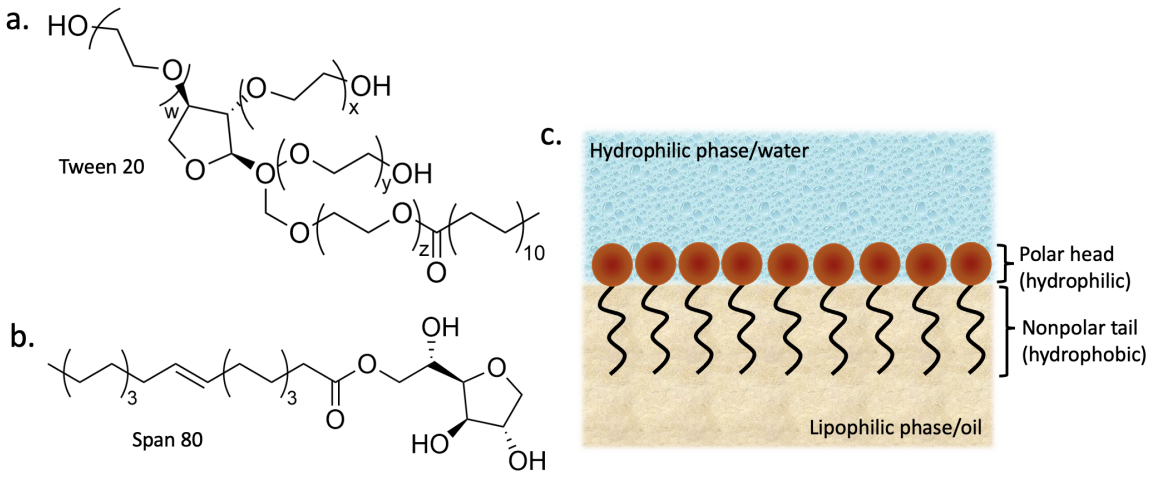

Figure 4.4: Chemical structures of a) Tween20 and b)Span80. c) Schematic representation of surfactant alignment at water-oil interface.

By adding surfactants

Another approach to delay the onset of Rayleigh-Plateau instability involves minimizing interfacial tension in all liquid compositions through the use of surfactants. The approach was inspired from the Hashimo et al. work, where Span 80 and Tween 20 surfactants were used in 2wt% concentration to reduce the hexadecane-water interfacial tension from $\gamma \approx 43$ mN/m to $\gamma \approx 0.01$ mN/m [82]. Accordingly, 2 wt% of Span80 (figure 4.4b) was added to the LCO solution and 2 wt% of Tween 20 (figure 4.4a) was added to the PVP solution. This enabled to reduce the interfacial tension substantially and the coaxial jet was extended up to 7 cm from the jet's origin in case of LCO1 (figure 4.3b). While in case of LCO2, perturbations began to appear around 5 cm downstream from the jet's origin (figure 4.3c).

Surfactants are amphiphilic molecules that adhere to the surfaces or interfaces of the system and alter the cohesive forces at the interface, causing significant reduction in the degree of interfacial tension [83]. When a surfactant is introduced to the system, the molecules migrate to the interface. The molecular structure of surfactant involve, a *lyophobic* group that has very little attraction for the solvent, and a *lyophilic* group that is solvent loving (figure 4.4c). Span 80 is a non-ionic surfactant that is suitable for water-in-oil emulsions. It has strong affinity for liquid crystal phases. It aligns at the interface between LC oligomer and aqueous polymer phase. This alignment at the interface reduce interfacial tension thus delaying the onset of Rayleigh-Plateau instability and promoting stable tubular flow in the microfluidic channel. Tween 20, in contrast, is a non-ionic surfactant that is suitable for reducing interfacial tension in oil-in-water emulsions. It has strong affinity for hydrophilic polymer solutions. It adsorbs at the interface between aqueous medium and LC phase, thus stabilizing the flow in microfluidic channel and preventing the collapse of the coaxial jet into shells or drops. Thus surfactants create smoother interfaces, reducing the flow resistance. This is particularly beneficial when working with viscous solutions such as LC oligomers that are prone to instabilities when flowing in micro-channels.

In this study, the addition of surfactants did not cause any destabilization, and the isotropic nature of LCO solution ensured that the presence of surfactant did not

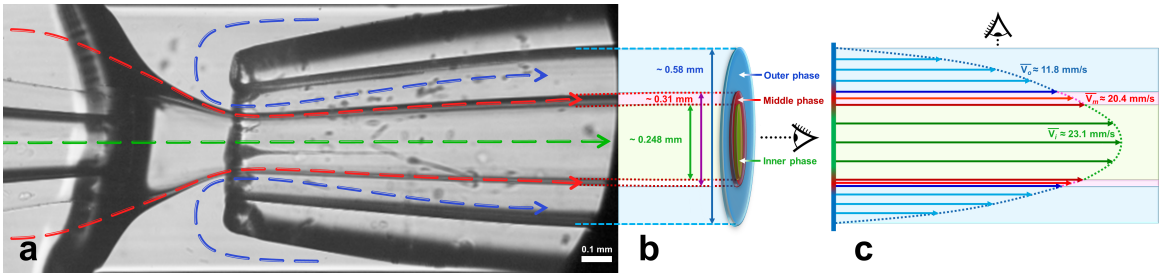

Figure 4.5: a) LCE tube production screenshot with arrows showing the flow of each phase (green arrow indicates inner phase flow, red indicates middle phase flow and blue indicates outer phase flow). b) Schematic representation of the flow cross-section with inner phase in green, middle phase in red and outer phase in blue color. c) Estimated flow profile of the corresponding tube production. Reproduced from [70].

affect the alignment of **n**. Since LCO2 demonstrates greater biocompatibility [47], most of our work is based on LCO2. From here on, we use 10 wt% PVP solution and surfactant addition for all future experiments.

4.2.2 Linear flow rate calculation and shear strain

The next constrain to overcome in producing LCE tubes is defining the ground-state alignment **n**, which determines the tube's actuation behavior. To address this, the LCE precursor solution is subjected to shear flow within the microfluidic device before photocrosslinking, creating a controlled ground-state alignment. The flow velocity profile across the three phases is analyzed by examining the jet geometry and comparing the volumetric flow rates.

The cross sectional area A_p of each phase p is calculated from the radius measured for each phase. The average linear flow rate of each phase was calculated using the formula $\bar{v_p} = \phi_p / A_p$. Flow profile analysis was conducted for a specific tube production experiment shown in Figure 4.5. Due to minor asymmetry in the coaxial capillary setup, the outer and middle phases appear slightly thicker at the top of the jet than at the bottom (see figure 4.5a). For simplicity, we ignore it and consider all boundaries between the phases are circular as shown in the schematic diagram, figure 4.5b.

The inner phase's cross sectional area is calculated as $A_i = \pi r_i^2 \approx \pi \cdot 0.1238^2 \approx 0.0482$ mm^2, where $r_i \approx 0.1238$ mm represents the radius of the inner phase in the jet (obtained from the measured inner phase diameter (green double arrow) in figure 4.5b). For the middle phase, the cross sectional area is given by $A_m = \pi r_m^2 - A_i$, where r_m is the outer radius of the middle phase (the diameter shown by red double arrow in the same figure). This yields $A_m \approx \pi \cdot 0.155^2 - 0.0482 \approx 0.0273$ mm^2. Similarly, the outer phase's cross sectional area is calculated as $A_o = \pi r_o^2 - A_m - A_i$ with r_o is the inner radius of the collection capillary (diameter shown as blue double-arrow in the same figure) resulting in $A_o \approx \pi \cdot 0.29^2 - 0.0273 - 0.0482 \approx 0.1887$ mm^2.

In this experiment, volumetric flow rates were set to $\phi_i = 4.0$ mL/h, $\phi_m = 2.0$ mL/h and $\phi_o = 8.0$ mL/h. These flow rates, along with the above cross sectional areas, gives linear flow velocities of $\bar{v_i} = \phi_i / A_i \approx 4.0 \cdot 10^3/3600/0.0482 \approx 23.1$ mm/s, $\bar{v_m} = \phi_m / A_m \approx 2.0 \cdot 10^3/3600/0.0273 \approx 20.4$ mm/s and $\bar{v_o} = \phi_o / A_o \approx 8.0 \cdot 10^3/3600/0.1887 \approx 11.8$ mm/s.

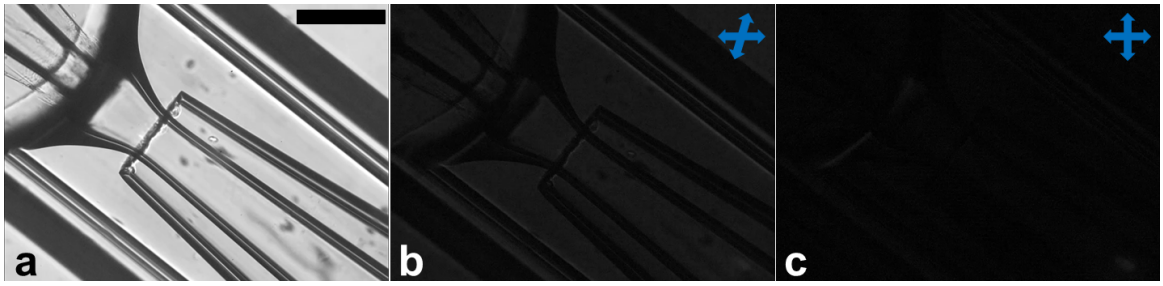

Figure 4.6: Coaxial jet tube production (same condition as in Figure 4.3 middle row) viewed a) without analyzer, b)between slightly decrossed polarizers and c) between fully crossed polarizers. [Scale bar in a) 0.35 mm, blue crosses in b) andc) indicate direction of polarizers], reproduced from [70]

Based on these values the flow velocity profile is sketched in Figure 4.5c, illustrating how the LCO solution experiences shear between the highest linear velocity in the inner phase and lowest in the outer phase. While this provides an approximate flow profile that meets the no-slip boundary conditions at each interface and reflects average flow velocities in each phase, a detailed calculation of the exact velocity variation across each phase has not been performed.

Since the middle phase is sheared between the inner and outer phase, and with a sufficiently high shear rate, a transition from isotropic to paranematic (shear induced long-range orientational order) is expected. To evaluate this, the coaxial jet was analyzed between cross-polarizers as shown in figure 4.6. The shear rate appears to be too weak to induce long-range orientational order in the solvent-rich LCO solution, which remains isotropic. This is evident in Figure 4.6, where the coaxial jet appears dark between de-crossed polarizers and remains completely dark with fully crossed polarizers (figure 4.6b and c respectively).

4.3 Polymerization of coaxial tubular jet into crosslinked LCE tubes

Once a stable tubular flow of the coaxial jet is established, the next step is to photopolymerize and crosslink the LCOs at the jet's downstream end within the microfluidic device. To accomplish this, the LCO solution in the middle phase must include photoinitiators that, upon UV irradiation, generate radicals and initiate radical polymerization at the acrylate termini of the oligomers. Irgacure 819 was used in our case (see figure 4.7).

On UV irradiation, the photoinitiators generate highly reactive radicals with unpaired electrons. These radicals readily react with the oligomers' acrylate end groups (double bonds), forming a new radical at the acrylate carbon. This initiates a chain reaction, where these radicals react with the neighboring acrylate ends of the monomer or oligomer to form a new radical. As the process continues, the polymer chain grows to form polymer networks. Crosslinking also occurs when the growing polymer chains interact with other oligomers, creating a 3D network of LCE with customizable mechanical and optical properties.

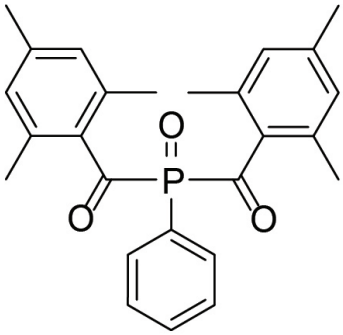

Figure 4.7: Chemical structures of the photoinitiator Irgacure 819

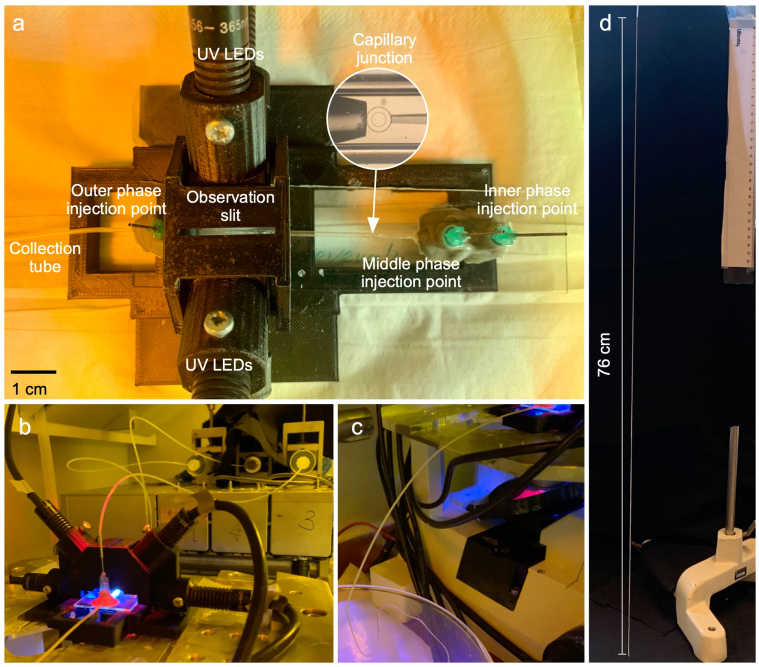

Figure 4.8: Macroscopic images of tube production set up, crosslinking of tubes and LCE tube. a) shows the UV-LED holder with the LEDs and the microfluidic device inserted in to the set-up.b) UV irradiation during LCE tube production. c) Collection of the polymerized tubes in a water bath. d) an LCE tube of $\approx 76\ cm$ long, suspended from a capillary mounted on a lab stand. Reproduced from [70]

In our study, polymerization is achieved through localized UV irradiation at a point further downstream from the origin of the stable coaxial tubular jet (figure 4.8). Maintaining this distance is crucial because the middle phase containing the LCO can act as a light guide if it has a higher refractive index than the surrounding phases. This effect is possible due to the aromatic structure (from RM257) present in LCO but absent in the inner and outer phases. If UV light is transmitted from the irradiation point to the jet origin, it can cause clogging. However, since the LCO solution contains photoinitiators and absorbs UV light, maintaining adequate distance between the jet origin and the UV irradiation point can attenuate the UV intensity at the origin, thereby preventing device clogging.

The polymerized tubes exit the collection tube at a rate of approximately 1 cm/s and can be collected continuously as long as the three syringes are loaded with their respective phases. However, production must be paused after some time due to overheating of the UV setup because the UV-LEDs lack a cooling mechanism.

The crosslinked LCE tubes are collected in a distilled water bath to prevent them from sticking to the glass slides. When collecting the tubes in air, beads form on the surface of the tube due to the Rayleigh-Plateau instability affecting the outer PVP solution, causing the cylindrical PVP coating around the LCE tube to break up. A white, sticky, but stable shape retaining tube is collected. Figure 4.8d shows an LCE tube of $\approx 75\ cm$ long collected. If collected for a longer time, the sticky nature of the tube causes it to coil, making it challenging to disentangle them in the water bath using basic methods. To address this issue in the future, lubricants or releasing agents like magnesium stearate can be used to coil or roll the tube around a spool.

4.3.1 Solvent-rich and solvent-lean phase separation

UV polymerizing the tubes induce phase separation. During polymerization, the miscibility of the polymer chains in the solvent (DCM) decreases due to increased molecular weight of the the network. At a certain point, phase separation occurs via either nucleation and growth or by spinodal decomposition mechanism where it separates into two co-existing phase where each is rich in one phase and lean in other. With further polymerization, the morphology further evolves until complete network is formed. The separated states have lower entropy. The minimum entropy is reached during polymerization as polymer domains are formed that have lower degrees of freedom. In nucleation and growth mechanism, phase separation occurs when the mixture is directed into a metastable region due to thermodynamic fluctuations. The metastable phase starts to separate into droplets or cavities of a phase which grows over time (there is a nucleation point). In contrast, spinodal decomposition occurs when the system becomes unstable and separates into two distinct phases without nucleation. This happens when there is no thermodynamic barrier to cross for phase separation.

When the SEM images of the cross-section of the LCE tubes were analyzed (figure 4.9), the walls show spherical cavities of diameter around 10 μm suggesting that UV polymerization induced phase separation has occurred (figure 4.9a-c). The cavities can be an indication of nucleation and growth phase separation, where the cavities can be DCM-rich phase that evaporated later to form them and the other phase to be nematic-rich and DCM lean. Higher magnification SEM images show, undulated

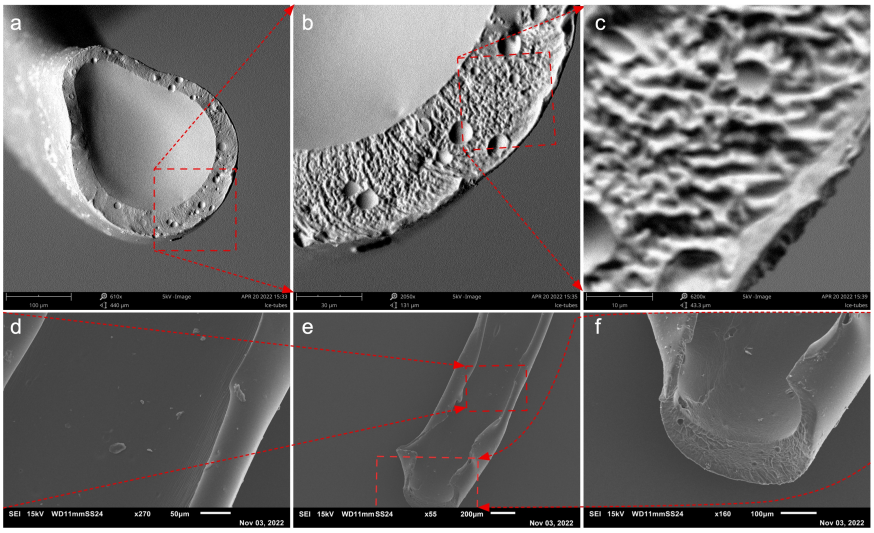

Figure 4.9: SEM images of two LCE tubes, each prepared through different cutting methods, are presented. The transverse cross-section images, with increasing magnification from (a) to (c), clearly demonstrate the occurrence of phase separation during the photocrosslinking process of the LCE precursor. In contrast, a second tube section was examined with both longitudinal and transverse cuts. At higher magnification, some areas of the tube exhibit striations oriented along the length of the tube (d), while other sections show striations that are perpendicular to the tube (f). Reproduced from [70].

pattern on a small scale which also suggest phase separation might have occurred by spinodal decomposition (figure 4.9d and f). Hence, we hypothesize that the early stages of polymerization have rapidly reduced the solvent compatibility, creating a driving force for phase separation in to polymer-rich and solvent-rich regions through spinodal decomposition. Since both the newly formed phases are liquid phases, coarsening into larger domains could only take place locally in regions with few crosslinks. This process explains the mixed SEM images of cavities as well as the undulating phases. We also conclude that, the polymerization induced phase separation partially aligns the middle phase of the coaxial jet into nematic. As shown in the figure 4.9d-f, transverse and longitudinal striations along the tube suggest that domain orientation may vary along the tube, with these striations likely marking the boundaries of phase separated domains.

4.4 POM characterization of LCE tubes

4.4.1 Ground state characterization

Different sections (end and middle section) of the LCE tubes were analyzed between cross polarizers immediately after production before the DCM leaves the system completely. In figure 4.10 a and e, weak birefringence is observed in the solvent-swollen state, appearing gray-white. When λ plate is inserted into the microscope, as shown in figure 4.10 b and f, the central part of the tube exhibits an orange color when aligned perpendicular to the optic axis of the λ plate. In contrast, when the tubes are aligned parallel to the λ plate optic axis, the color shifts to blue. This behav-

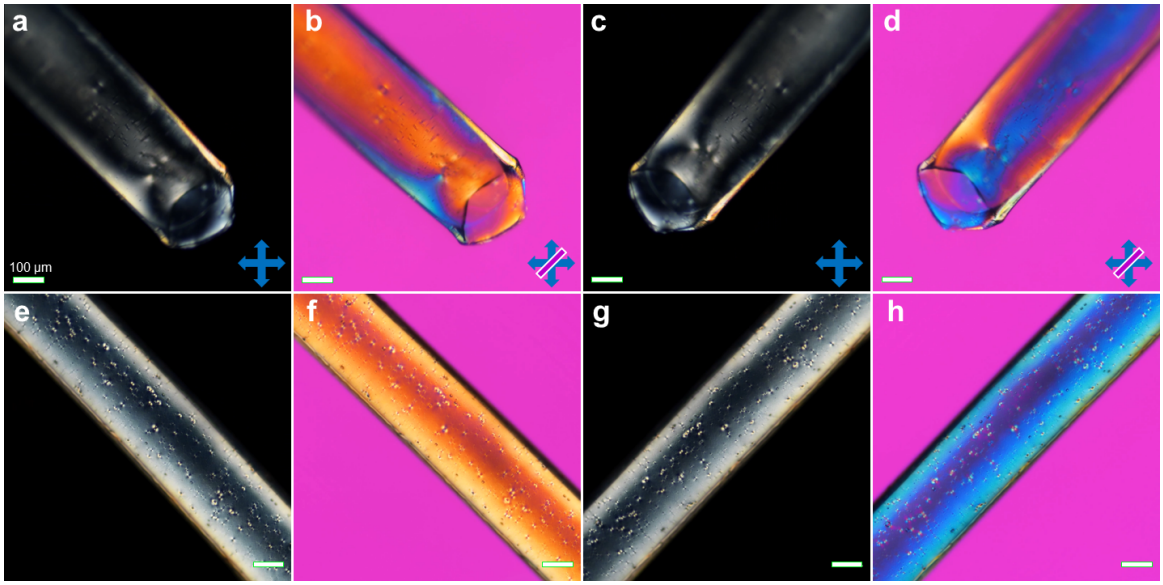

Figure 4.10: (a) An LCE tube with residual DCM content directly after production is examined by POM in transmission mode. Frames (a, c, e, g) show images without the first-order λ plate, while frames (b, d, f, h) include the λ plate for enhanced birefringence contrast. The orientation of the polarizers is marked by blue crosses, and the λ plate optic axis is indicated with a purple bar. Reproduced from [70]

ior indicates positive birefringence ($S > 0$) with the director $\mathbf{n}(\mathbf{r})$ oriented along the tube. But in figure 4.10 a-d, the tube also displays a blue color along the edges when aligned perpendicular to the λ plate optic axis and changes to orange color when aligned parallel to the λ plate optic axis. This indicates that structural changes occur or starts at the end of the tube, where extraction of DCM occurs more rapidly. On observing a tube of about 10 cm after production, it was seen that the initial sections of the tube showed birefringence behavior similar to that shown in Figure 4.10 a-d. However, as one moves along the length of the tube, the color varies to yellow in the center and green at the edges, eventually shifting to green and then blue. This is an indication of lowering in birefringence that the tube adds to that of the λ plate plate. Further along the tube, the negative optical character begins to dominate. From the color changes, we can conclude that the optical character can shift between positive and negative birefringence at different sections along the tube.

Figure 4.11; shows tube sections after one day of production between the cross polarizers. All the DCM has been extracted or diffused from the tube. The birefringence is now stronger giving a yellow-orange color along the edges of the tube (Figure 4.11a and b). The texture of the tube is less smooth compared to right after production and much darker on the outside compared to inside. One major change occurred to the tubes now is that the colors have reversed compared to the tube right after production. Now the tube turns blue when it is aligned perpendicular to the λ plate optic axis and orange when aligned parallel (Figure 4.11 c and d).

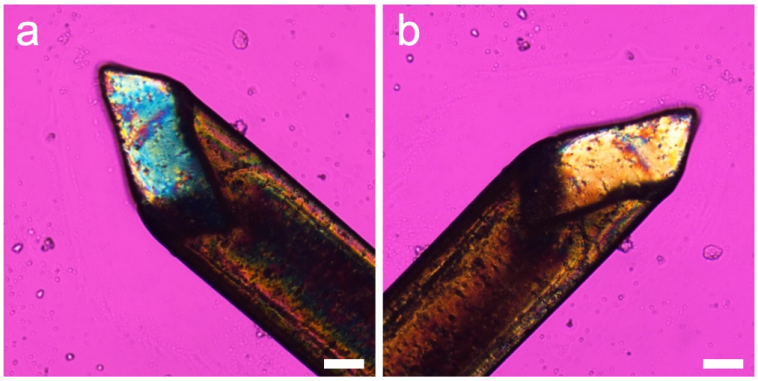

Figure 4.11: Transmission POM images with a first-order λ plate, capturing the opposite end of the same tube depicted in the upper row of Figure 4.10. These images were taken one day post-production, after the complete evaporation of DCM from the tube, which had been stored in distilled water throughout. The polarizer, analyzer and λ plate directions are similar as in Figure 4.10. In (a), the tube axis is perpendicular to the λ plate optic axis, while in (b), it aligns with it. [Scale bar: 100μm].

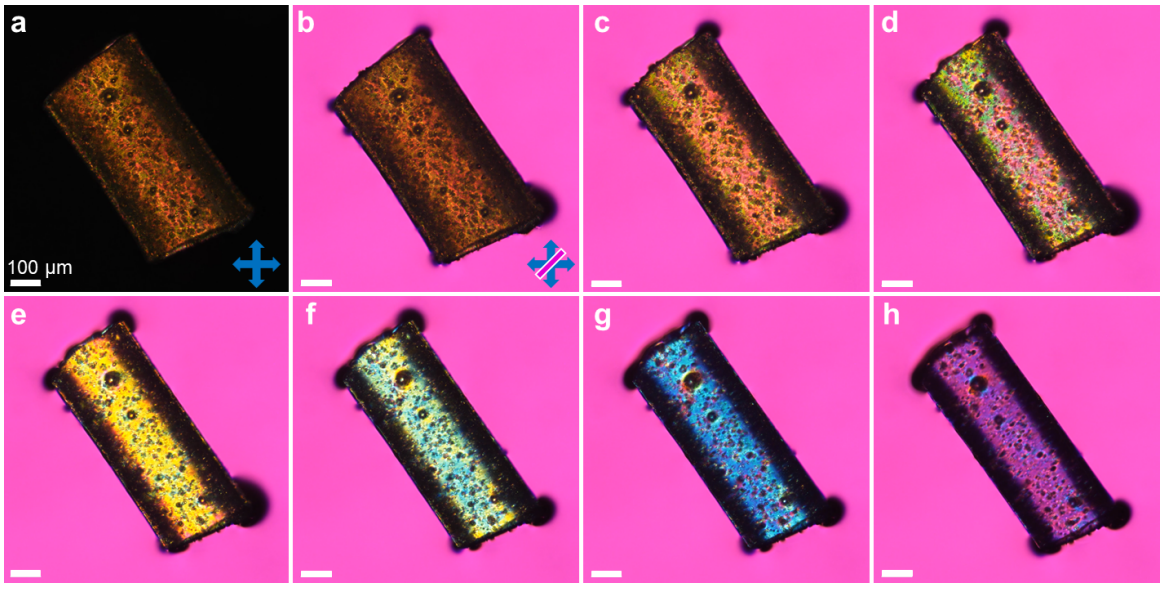

Figure 4.12: (a–h) Sequential frames showing the actuation process of a longitudinal LCE tube section observed in transmission POM as the temperature increases from (a) 23 °C to (h) 50 °C. Image (a) is captured with crossed polarizers (indicated by blue double arrows), while the remaining frames include a first-order λ plate with its optic axis orientation marked in (b). The actuation is reversible; however, complete relaxation back to the ground state requires a longer period (up to 1 hour or more) if heated to the isotropic phase. If heating is limited to 43°C (around panel (g)), relaxation occurs more rapidly. The dark spheres near the ends of the tube during actuation are air bubbles that are expelled from the tube's interior.

4.4.2 LCE tube actuation

Actuation along the longitudinal tube section

To study the actuation of the tube in more detail, a longitudinal section was cut from the more uniform part of the tube. The sample is kept in glycerol and observed between cross polarizers (figure 4.12). When the tube is heated from 23 °C to 50 °C, it visibly elongates while its radius decreases. Additionally, black spheres (air bubbles) appear at the ends of the tube as it heats up, suggesting that the tube is expelling fluid as its internal volume shrinks. Upon cooling, the air bubbles are drawn back into the tube's core. On analyzing at the microscopic level, the color of the tube changes during actuation. Comparing these colors with a Michel-Lévy chart, we see that initially the tube displays a third-order yellow and moves through second-order color purple fig. 4.12(d), yellow (e), green (f) and blue (g), ultimately approaching the purple color of the λ plate in (h). The final purple color indicates that the tube has very little birefringence left.

Here the tube is oriented in such a way that the long axis of the tube is perpendicular to the λ plate optic axis. For LCEs that have positive birefringence ($\Delta n > 0$) with the optic axis aligned along the tube, one would expect a reduction in birefringence compared to the contribution of the λ plate. However, the observed behavior is different: the LCE always adds birefringence, the contribution getting continuously smaller as it heats up to a temperature where the tube becomes nearly isotropic. This observation might suggest that the alignment (director) of the LC molecules in the tube is not along the tube's length but is instead arranged in a radial pattern, which would explain why the tube behaves as it does. A typical LCE contracts along the director and expands perpendicular to it, so if the director is radial, the tube would lengthen, and its radius would decrease when heated, which matches our observations. However, it is unclear why the director would take on a radial configuration in the tube.

Actuation across the cross-section of the tube

To test the configuration of the director in the tube, we cut a 120 μm section of the central part of the tube. We examined its actuation using POM while being observed both along the tube axis and perpendicular to it (figure 4.13). If the director were radially oriented, strong birefringence would be expected when viewing this thick sample along the tube axis, except at locations where the director aligns with either the polarizer or analyzer (such as top, bottom, left, and right edges of the ring-shaped cross-section). However, in the observed cross-section, there is almost uniform weak birefringence around the entire ring in its ground state (figure 4.13a-e), showing no correlation to the polarizer and analyzer directions. This suggests that the director is not oriented radially.

Additionally, the cross-section is noticeably non-circular, indicating that cutting the section released substantial residual stress. When heated to 40°C which is below the full actuation threshold, the birefringence along the tube axis increases (figure 4.13b). At this temperature, the cross-section becomes slightly more circular, and the enclosed area becomes smaller than in its initial state. Once cooled back to 23°C, both the original shape and birefringence are quickly restored (figure 4.13c). At 60°C (fig-

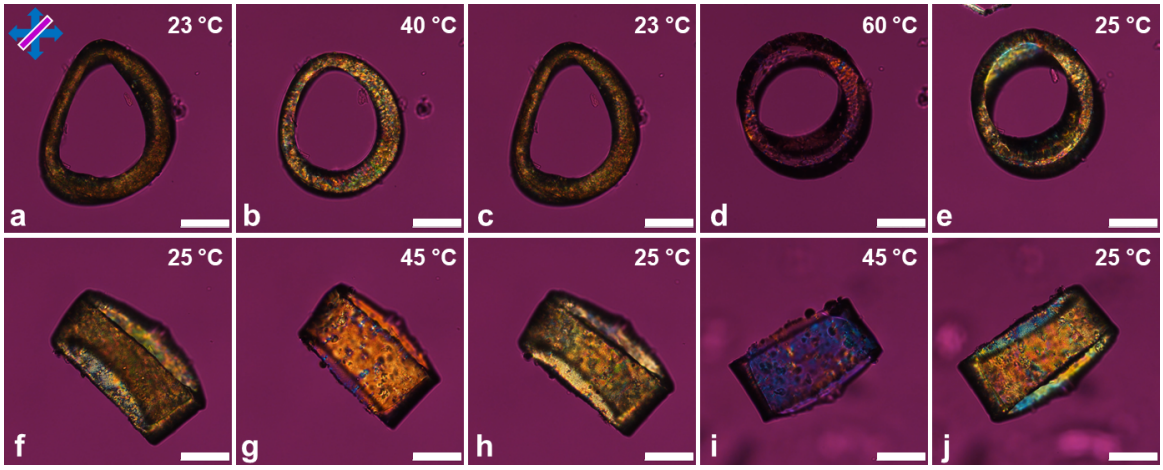

Figure 4.13: An LCE tube cross section is observed in transmission between crossed polarizers with a first-order λ plate (orientation directions shown in (a)). When heated from 23° to 40° (panels a–b), the section becomes more circular in shape, reverting quickly to its original form upon cooling (c). Heating further to 60 °C (c) results in a smoother, circular shape; however, the initial shape only gradually reappears as the tube cools. In (e), the nearly circular shape is maintained for around an hour despite cooling again. Panels (f–j) display the actuation and relaxation of the same section in a direction perpendicular to the tube axis, with the axis aligned along (f–h) and perpendicular to the λ plate optic axis in (i–j). [Scale bar: 0.1 mm], reproduced from[70]

ure 4.13e), the section becomes fully isotropic, indicating complete actuation. An area decrease of approximately 5% is estimated based on approximating the initial shape as an ellipse. When the sample is cooled back to room temperature, the circular shape is initially retained, and the birefringence increases significantly (figure 4.13f). Over time (about an hour), the tube gradually relaxes back to the ground state. Figure 4.13a-f, shows actuation of the same cross-section when the tube axis is in the sample plane and perpendicular to the λ plate optic axis. So, these results indicate that the tube is not radial in its ground state, as previously hypothesized.

A possible explanation for the observed behavior of the tube we propose is that the director is indeed aligned along the tube axis but with the global orientational order parameter of the fully relaxed, solvent-free tube being negative ($S < 0$). When $S < 0$, it indicates that the molecules or mesogens align perpendicular to the director ($\mathbf{n}$), with no preferential direction within that plane. This leads to negative birefringence, which could explain the reversed color shift we observe in the POM images despite the director being oriented along the tube axis. In addition, this negative order parameter would account for the actuation behavior of the tube. An LCE with $S < 0$ in its ground state behaves in a way that is opposite to conventional LCEs: it expands along the director($\mathbf{n}$) and contracts perpendicular to it when $S \to 0$ upon heating. This behavior matches our observations, where the tube extends lengthwise and narrows in radius as it is heated.

The hypothesis of a negative order parameter also clarifies the lack of brightness modulation observed in the transverse cross-section of the tube when viwed on POM, as seen in (figure 4.13a). Since we are observing the structure along the director, which

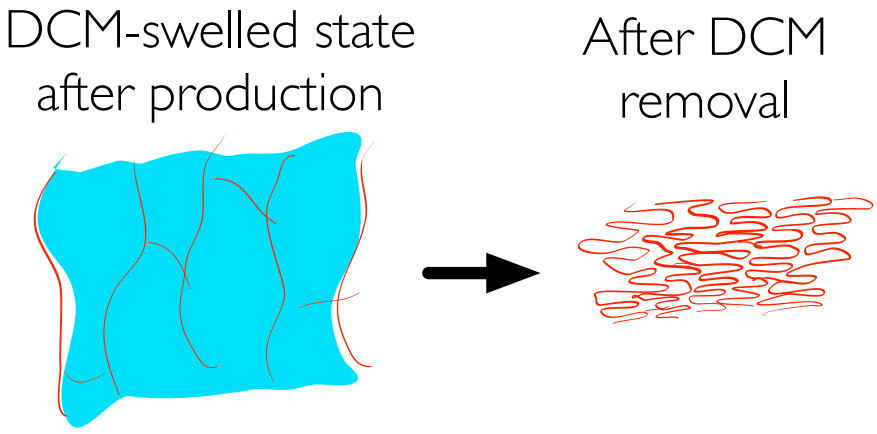

Figure 4.14: Schematic 2-D representation of suggested DCM swollen state colliding to negative order parameter LCE tube structure on DCM removal. The LCE network is shown in red and the solvent rich domain in blue, reproduced from[70].

coincides with the global optic axis, the expected modulation relative to the polarizer and analyzer directions is absent. If the director were perfectly aligned along the tube axis, no birefringence would be expected; however, the presence of slight birefringence indicates some local deviations in the director's orientation around the tube axis. This type of negative order seems to dominate the behavior throughout the tube under study. However, other sections of the tube showed positive order parameter along with negative order parameter. This suggests that the exact configuration and behavior of the LC tube depend sensitively on the production conditions and parameters. Such variability in the molecular order could also explain the different orientations of the striations seen in the SEM images in different sections of the tube, as shown in fig. 4.9d–f. These results highlight the importance of production methods in influencing the LCE's molecular arrangement and resulting physical properties.

Origin of negative order parameter

We suggest that during the phase separation process by spinodal decomposition, the shear flow disrupts symmetry and causes each phase to stretch along the flow direction, which aligns with the tube axis. Due to the significant amount of DCM present in the tube during the crosslinking stage, channels are formed along the tube, filled initially with a DCM-rich, LCO-deficient phase. As the crosslinked tube stabilizes over several days, the DCM gradually diffuses through the surrounding aqueous environment and evaporates once it reaches the surface. As the DCM exits the tube, capillary forces cause the remaining LCE to contract, aiming to minimize void formation. This contraction primarily occurs along the tube axis, as the initial DCM-rich channels are oriented along this direction. This contraction forces the mesogen network- initially oriented along the tube axis due to the shear flow- to buckle and reorient in random directions perpendicular to the tube axis. The reorientation is schematically depicted in figure 4.14. This buckling and subsequent reorientation might lead to a negative order parameter ($S < 0$), potentially explaining the behavior observed in figure 4.12a-h and 4.13. The notable soft mechanical properties exhibited by the tubes can also be explained using this hypothesis.

In this negative order parameter configuration, the mesogens can easily extend along

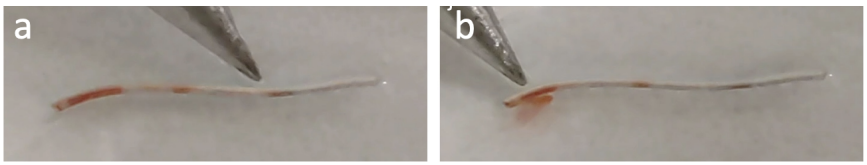

Figure 4.15: Demonstration of peristaltic pumping using an LCE tube segment, partially filled with red-dyed water kept on a drop of glycerol. The pointed end of a heated soldering iron is positioned in the glycerol near the tube and then moved along its length, inducing a peristaltic motion that expels the red-dyed water from the tube, as shown in (b).

the tube axis with minimal resistance. This mechanism bears resemblance to the supersoft elasticity found in typical LCEs with $S > 0$, where isotropic genesis results in a polydomain ground state and strain rotates the director at very low energy costs [84]. However, in our tubes, which start with isotropic genesis but undergo shear-induced alignment during crosslinking, the director does not rotate with strain. Instead, the transition from $S < 0$ to $S > 0$ happens via a similarly low-energy pathway. This proposed explanation also clarifies the tube's high elongation at break. On realigning the polymer chains from perpendicular to the tube axis to parallel, substantial extension without breaking covalent bonds is possible. Consequently, the observed softness does not imply structural weakness; it suggests flexibility in regions where $S < 0$, enabling significant elongation along the tube axis.

4.4.3 Dye pumping across the tube section and porosity

In figure 4.12a-h, we see that black spheres (air bubbles) at the tip of the tube become larger and larger as we heat the tube from 23°C to 50°C. Upon cooling to room temperature, the tube relaxes to ground state and the air bubbles are retracted by the tube to its hollow core. This indicates that during actuation, LCE tubes propel liquids to the surroundings mimicking a pumping action. To confirm this, we observe an approximately 1 cm long tube section filled with Congo-Red dye colored water kept on a drop of glycerol at microscopic level (figure 4.15). When a sharp tip of of hot soldering iron is moved along the tube, the dye is expelled out of the tube, confirming a peristaltic pumping action. Even though the pumping is fast, it takes a lot of time for the tube to relax back to its initial ground state. This experiment demonstrates that with optimizing the chemistry and processing of the tube, they can be used as peristaltic pumps for different applications.

To demonstrate that the LCE tube has a continuous hollow core, an end of a ≈ 21 cm long tube section was connected to a tapered capillary with an outer orifice diameter matching the inner diameter of the LCE tube (100μm). The opposite end of the the capillary was connected to a PTFE tube, which was then connected to a syringe containing Congo-red dyed water. The whole set up was mounted vertically on a pole with a petridish positioned below the lower end of the tube as shown in figure 4.16. As the piston is pressed, the dyed liquid travel from the syringe through the capillary and enters the LCE tube to exit as droplet on the other end and fall into the petridish. As the dyed liquid passes through the tube, it turns red colored. The tube section we chose to do this experiment has an outer diameter of $\approx 300\mu$m and

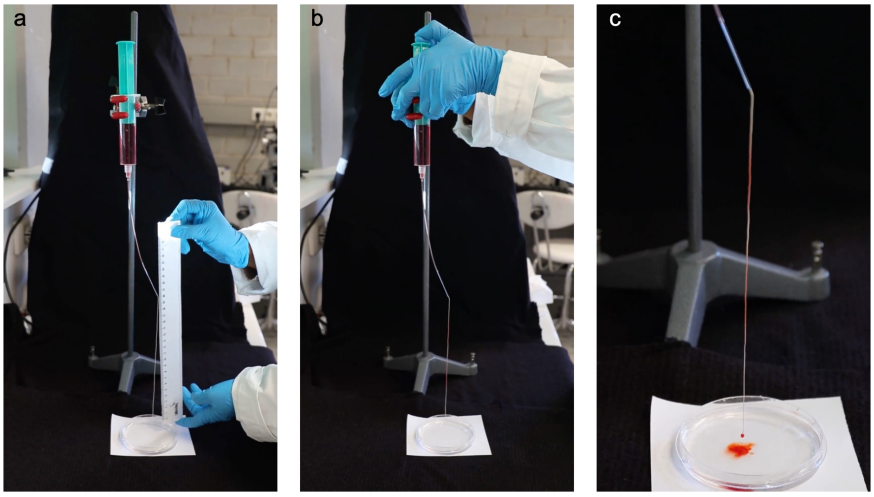

Figure 4.16: (a) An LCE tube is mounted vertically by securing one end to a tapered capillary, which is connected to a PTFE tube that is attached to a syringe via a Luer lock. The syringe is filled with Congo red-dyed water. (b) Demonstrates the process of pushing the dyed water through the tube, and (c) shows the dyed water exiting the tube and dripping into a petridish.

the length through which the liquid travels through the tube proves the hollow core continuity across a length of ≈ 800 diamaters.

4.5 Mechanical testing of LCE tubes

To assess the stress-strain relationship of the LCE tubes produced, tube sections were mounted vertically using tape at both ends on a Mark-10 F105-IMTE Advanced Test Frame, coupled with FS05-05 Tension and Compression Force Sensors. The tensile strain along the tube was calculated using the equation $\epsilon = \frac{\Delta L}{L_0}$, where ΔL is the extended length and L_0 is the tube's original length before force application. The tensile stress was calculated with $\sigma = F/a$, where a is the dynamic cross-sectional area of the tube and F is the force recorded by the instrument. The original cross-sectional area a_0 was measured as $a_0 = 0.7$ mm^2 using the POM, and the dynamic value during testing was calculated as $a = \frac{L_0 a_0}{\Delta L + L_0}$. Figure 4.17 shows the stress-strain curves obtained for three different sections of LCO2-based LCE tube, each stretched until breaking.

As seen from the stress-strain curves, a Young's modulus of $\approx 0.3kPa$ is reported which indicates that the LCE tube is extremely soft and flexible and confirms their elastomeric behavior. Such a low modulus also indicates that material can be undergo reversible deformations under minimal stress. It can undergo substantial stretching and bending without breaking, making it suitable for applications in soft robotics, biomedical applications and as actuators.

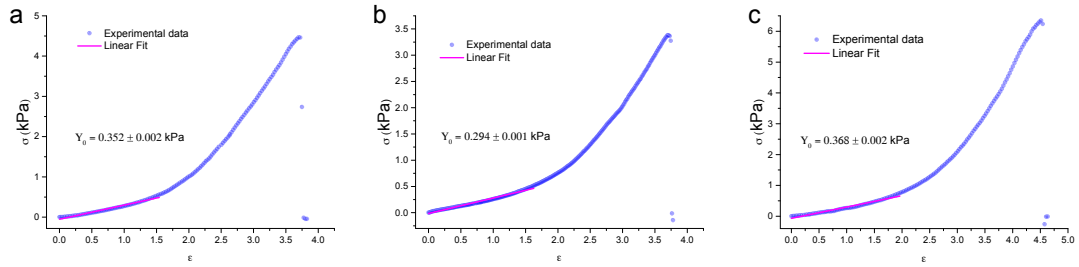

Figure 4.17: Stress-strain curves of three sections of LCO2 based LCE tube section upon stretching until break point.

4.6 Paving the way for artificial vasculature with LCE tubes

The successful realization of arbitrarily long LCE tubes with micrometer diameter, through continuous coaxial flow represents a substantial step toward scalable, bio-integrable actuator systems. These tubes are soft, flexible, and capable of reversible deformation under mild heating— expanding along their length and contracting radially. This actuation pattern enables peristaltic pumping, making the tubes promising candidates for fluid transport in biological systems such as artificial vasculature for organoids.

Most tube sections show conventional LCE behavior, with alignment along the tube axis due to flow-induced shear during polymerization. However, certain regions exhibit an inverted optical character and opposite actuation response. This suggests a structural rearrangement during solvent removal, potentially linked to phase separation into solvent-rich and solvent-lean domains. The collapse of these domains could result in a network where mesogens align predominantly perpendicular to the tube axis, leading to a negative order parameter ground state. Such alignment may result from polymerization-induced phase separation under shear flow that is triggered by the in-situ UV polymerization done to convert liquid LC precursor into LCE.

These variations in behavior raise fundamental and practical questions. Quantifying the order parameter at different locations and stages of actuation will be key to understanding the underlying structure. Techniques such as polarized Raman spectroscopy or wide-angle X-ray scattering may provide insight. Addressing this will also involve improving control over the tube's internal morphology during fabrication and studying how tube geometry, like wall thickness and diameter, affects actuation performance.

Thermal actuation leads to longitudinal extension and radial compression, resulting in net volume reduction. If this deformation is translated along the tube, it creates a peristaltic pumping effect. To improve the responsiveness of this mechanism, especially relaxation speed, modifications to the network structure are essential. Strategies include increasing crosslink density by incorporating multifunctional monomers and reducing residual solvent by producing the tubes at higher temperatures. These changes may help retain a stable nematic state and enhance mechanical robustness, but they also require careful evaluation, as they affect the tube's overall behavior and

performance.

To enable real-world biological applications, especially in sensitive environments like organoids, actuation must be achieved without relying on bulk heating. Strategies such as incorporating infrared-responsive dyes, using photoisomerizable groups, or tailoring the material chemistry to trigger shape change near body temperature are promising routes to achieve this. Functionalizing tube surfaces, particularly those exposed during solvent removal, can allow for controlled permeability and enhance compatibility with aqueous systems. These directions, which aim to extend both the versatility and biocompatibility of LCE tubes, are explored in the following chapters through material design and biological integration studies.

Chapter 5

Towards Biocompatible Photoresponsive Liquid Crystal Elastomers: An Oligomeric Approach

This chapter presents the synthesis of an azobenzene-incorporated main-chain LCE film designed to actuate at temperatures closer to physiological conditions (around 37°C), which are lower than typical actuation temperatures observed in conventional LCE systems. Two azobenzene homologues with varying alkyl chain lengths are investigated to assess their effects on transition temperatures using POM and DSC, along with the influence of UV irradiation in further reducing these temperatures. The selected homologue is then used to create a monodomain LCE sheet via oligomer method and stretching. Both thermal and UV-driven actuation of the monodomain LCE film is investigated. This study aims to determine optimal conditions to enhance actuation efficiency, directing efforts toward developing photoactuated LCEs suitable for use in organoids.

5.1 POM Insights into the Transition Temperatures of Liquid Crystal Oligomers and Elastomers

Unless explicitly stated, PETMP is not included in the formulations of azo-LCOs and LCEs discussed in sections 5.1-5.3.

With and without UV irradiation

To test the relationship between alkyl chain length and the stability of the *cis* isomer in azobenzene-containing LCEs, two homologues of the azobenzene moiety were selected: 9-azo and 6-azo shown in figure 5.1. The hypothesis was that when incorporated into the LCE network, a shorter alkyl chain, such as in 6-azo, would result in a shorter *cis* lifetime and faster relaxation back to the *trans* state, while a longer alkyl chain in 9-azo would lead to slower relaxation from *cis* state. This is because longer alkyl chains can reduce the electron donor-acceptor pull in the azobenzene structure, potentially increasing the *cis* lifetime. As the azobenzene revert from the bent *cis* conformation

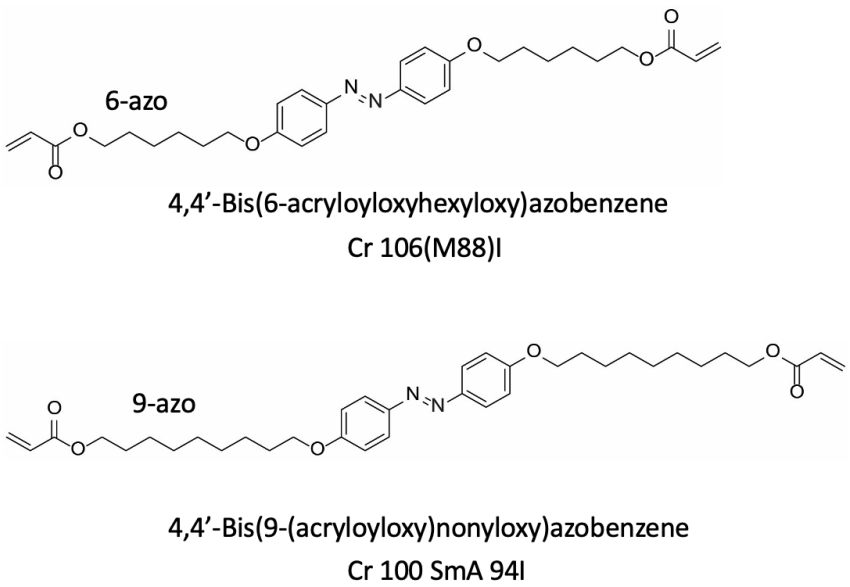

Figure 5.1: Chemical structure of 6-azo and 9-azo compounds with their IUPAC names.

to the extended *trans* form, they induce a macroscopic response in the LCE network.

To evaluate this, I analyzed the nematic-isotropic transition temperature (T_{NI}) of both 9-azo and 6-azo LC oligomers (LCOs) and LCEs. The samples were spin coated onto glass slides into 100 μm thick films, followed by solvent evaporation. In case of LCE preparation, the spin coated oligomers with Sn784 photoinitiator were then photopolymerized by exposure to blue light (wavelengths greater than 450 nm) for 30 minutes. Bar coating was chosen to achieve uniform samples to ensure uniform light absorption throughout the sample. This is important because, without uniform coating, light irradiation on LCEs containing azobenzene can cause a non-uniform distribution of light-absorbing azobenzene units along the thickness of the material.

Once the samples were prepared, the T_{NI} values were analyzed by heating and cooling the samples on a hot stage (Linkam) mounted on the POM from 20°C to 60°C at a rate of 1°C/min. The samples were then cooled back to the initial temperature at the same rate. To check the effect of UV light irradiation on the T_{NI}, a similar heating and cooling cycle was performed, but during the heating cycle, the samples were also irradiated with UV light (5.5 mW/cm^2) using an LED source to induce the *trans-cis* photoisomerization of azobenzene.

From the POM analysis, all LCOs and LCEs show a single LC phase with a grainy texture, which is a typical texture of an unaligned nematic phase. The T_{NI} of 9-azo-LCO was found to be $\approx$ 56°C , while that of 6-azo-LCO was higher, $T_{NI} \approx 63$°C (figure 5.2). In case of LCE, the T_{NI} of 9-azo-LCE was lower, $T_{NI} \approx 42$°C, compared to 6-azo-LCE, which had a T_{NI} of $\approx$ 47°C (figure 5.3). Under UV irradiation, the T_{NI} values for both LCOs and LCEs decreased compared to their respective T_{NI} values without irradiation. This drop in transition temperature is attributed to the photoisomerization effect of the azobenzene molecules incorporated in the samples. On irradiating with UV, the *trans* form of azobenzene moieties photo-isomerized to

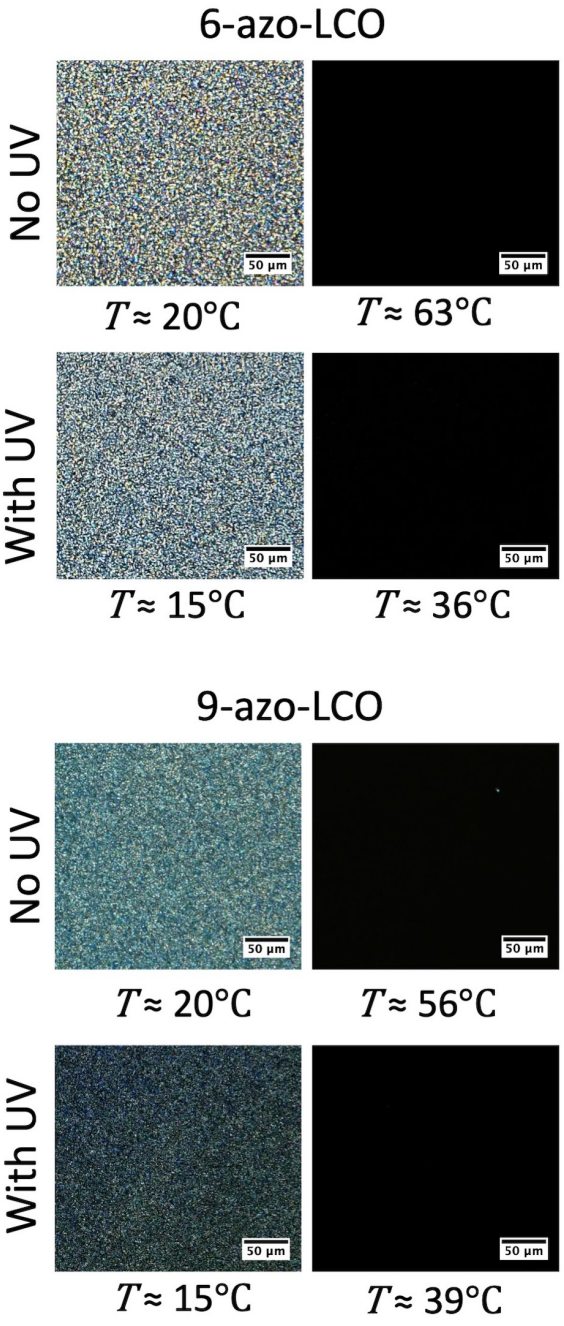

Figure 5.2: POM images with crossed polarizers, of 6-azo and 9-azo LCO samples in the nematic state (left column) and just above their respective clearing temperature to isotropic phase (right column), recorded both without (upper row of each section) and with UV irradiation (lower row of each section).

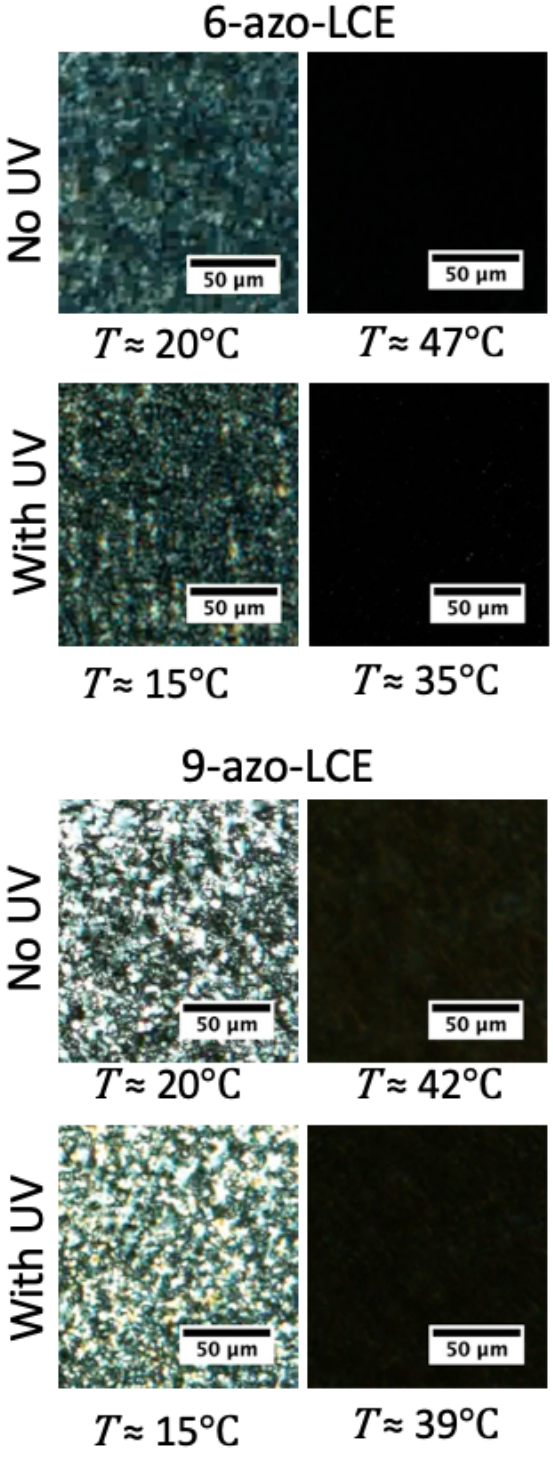

Figure 5.3: POM images with crossed polarizers, of 6-azo and 9-azo LCE samples in the nematic state (left column), and just above their clearing point to isotropic phase (right column), recorded both without (upper row of each section) and with UV irradiation (lower row of each section).

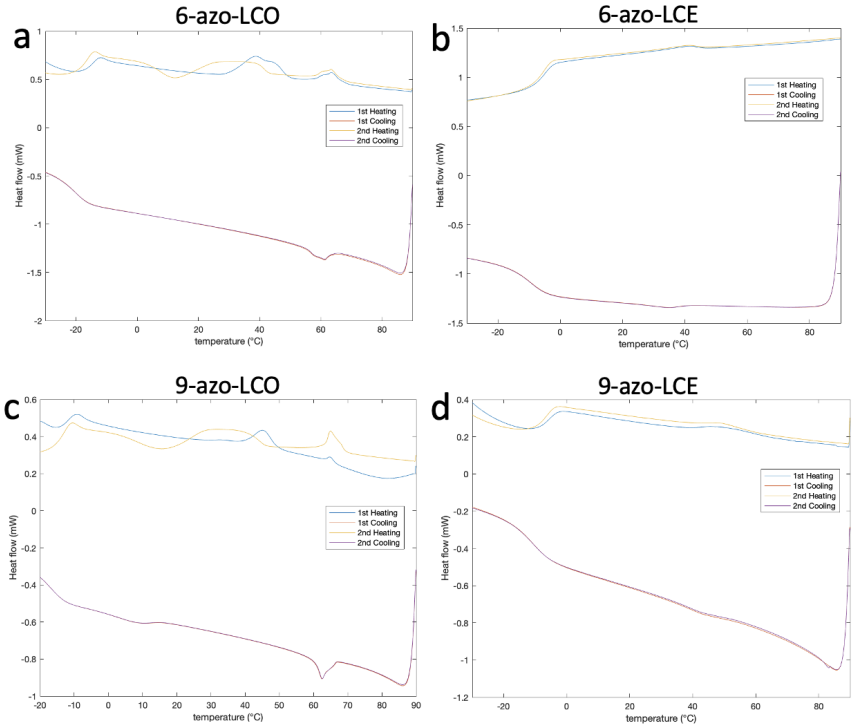

Figure 5.4: DSC thermograms are shown for (a) 6-azo-LCO, (b) 6-azo-LCE, (c) 9-azo-LCO, and (d) 9-azo-LCE, with each sample undergoing both the first and second heating and cooling cycles. The analysis was conducted over a temperature range from -40°C to 90°C at a rate of 5°C/*min* and cooled back.

cis form. This causes the liquid crystal order to be reduced resulting in a lower T_{NI}.

While the initial hypothesis predicted a higher T_{NI} for the longer alkyl chain derivative (9-azo), the observed trend showed that the 6-azo variants had consistently higher T_{NI} values in both LCOs and LCEs. One possible reason for this deviation could be the sample preparation process. During synthesis, the materials were dissolved in DCM and bar-coated onto glass slides before allowing the solvent to evaporate. Incomplete removal of DCM may have led to residual solvent being trapped within the material, disrupting local order and effectively lowering the observed T_{NI}, particularly in the 9-azo systems.

5.2 Differential Scanning Calorimetry analysis of LCOs and LCEs

To understand the thermal behavior, I performed DSC on all samples of LCOs and LCEs. The DSC measurements were done by first cooling the samples to -40°C at a rate of -5°C/*min*, followed by heating to 90°C at a rate of 5°C/*min* to acquire the first heating data. The samples are again cooled to -40°C and then re-heated to 90°C to attain the second heating data (figure 5.4).

The DSC data for LCO reveal two notable thermal peaks during the first heating runs (figure 5.4a and c). In addition to the high temperature endothermic peak with onset at 60°C for 6-azo-LCO and 65°C for 9-azo-LCO- which corresponds to the nematic-

isotropic transition observed in POM results (without UV exposure), a broader peak also appears in a lower temperature range. This broader peak is detected around 40°C for 9-azo-LCO and around 30°C for 6-azo-LCO during their respective heating cycles. The origin of such a peak in DSC typically corresponds to an enthalpic change associated with a phase transition or molecular rearrangement, such as the relaxation of kinetically trapped structures or reorganization of isomers.

The appearance of the the lower temperature peak indicates that the sample exists in a mixed state of trans and cis isomers. That is, the lower-temperature peak likely reflects the thermal relaxation or reorganization of a population of azobenzene moieties that exist in the *cis* form due to partial photoisomerization or residual effects from sample preparation and handling. This endothermic process reflects the absorption of heat as the system reorganizes into a more thermodynamically stable, ordered *trans*-dominated state. However, these broader peaks are absent during the cooling cycles, because no new *cis* isomer formation occurs thermally in the dark; the system simply undergoes conventional phase transitions. Interestingly, the low-temperature peak reappears during the second heating cycle, though it becomes more smeared out across a wider temperature range and with onset shifted to lower temperatures, around 20°C for both oligomers. Since the sample remains inside the DSC instrument throughout and is not exposed to light, the reappearance of the peak cannot be attributed to new *cis* formation. One possible explanation is that, during cooling, kinetically trapped or glassy states form, and their relaxation upon reheating produces a similar enthalpy peak. This remains an open point of interpretation, and further investigation would be required to fully resolve the origin of this recurring thermal event.

For LCEs, the DSC recorded T_{NI} peak for 6-azo-LCE is: 45°C and 50°C for 9-azo-LCE. The T_{NI} peaks detected for both LCEs seem less distinct, with lower intensity and broader shape compared to LCOs, likely because the crosslinked network limits the mobility and alignment of the mesogens, making the phase change more gradual. Importantly, although the network limits large-scale motion, the mesogenic units still retain enough local freedom to undergo orientational disordering, which allows the nematic–isotropic transition to be observed in DSC, albeit in a suppressed form.

A key observation from the DSC data is the absence of broader peaks at lower temperatures in LCEs which are present in LCOs. These peaks in LCOs were assigned to the thermal relaxation of residual *cis* isomers. In LCEs, however, the permanent crosslinked structure likely inhibits large-scale molecular rearrangements, reducing the ability of the system to relax in the same way upon heating. The network constrains both the azobenzene units and the polymer chains, thereby suppressing the enthalpic events related to isomer relaxation that are evident in the more flexible LCOs. Finally, the glass transition temperatures of the LCOs are lower in comparison to those of LCEs, indicating the flexibility of the chains in oligomers that require less energy to move. Due to crosslinks in LCEs, they have restricted movement, and thus T_g is higher.

Unlike the POM study, the DSC analysis did not require dissolving the samples in DCM. This difference could explain the slight variation in the clearing points observed between the two methods, potentially due to residual DCM present to varying degrees in the 6- and 9-azo-LCO samples analyzed by POM. As a result, the tran-

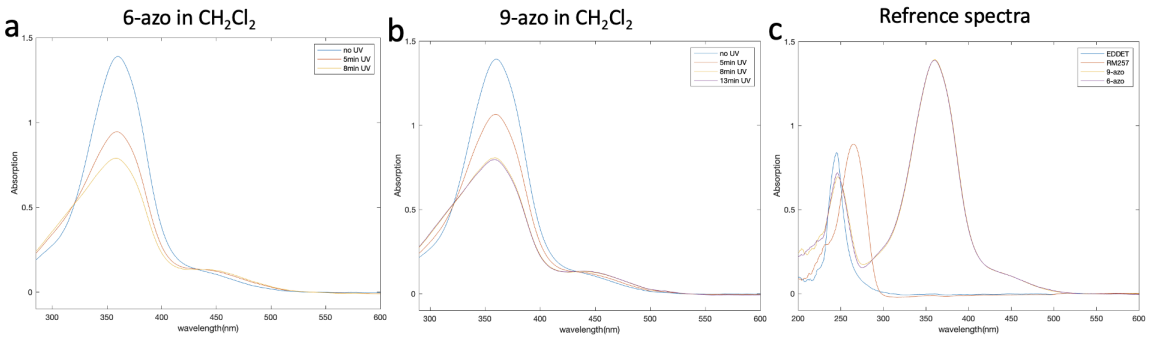

Figure 5.5: UV-Vis spectra are shown for: (a) 6-azo in DCM, (b) 9-azo in DCM, and (c) individual monomers RM257, EDDET, 6-azo, and 9-azo in DCM before and after UV irradiation.

sition temperatures measured by DSC are considered more reliable indicators of the material's thermal behavior. Based on these findings, it is evident that 9-azo-LCO exhibits a slightly higher clearing temperature in the trans state compared to 6-azo-LCO. Consequently, 6-azo-LCO was selected for the remaining experiments in this study.

5.3 Uv-vis spectroscopy analysis of LCOs and LCEs

UV illumination and absorption spectra and back-relaxation kinetics

UV-Vis spectroscopy experiments were conducted to determine the optimal illumination time for the complete photoisomerization of azo-LCOs and azo-LCEs, using a fixed UV light intensity of 5.5 mW/cm^2. Before analyzing these samples, it is essential to record reference spectra for all of the monomers present in the system. Recording the reference spectra will help us to understand how the peaks of the other components in the system will affect the azo peaks and also to better understand the photoisomerization behavior without the constraints of the polymer network.

I recorded the spectra of the individual monomers RM257, EDDET, 4-azo, and 6-azo in dichloromethane as shown in figure 5.5. In these spectra, both 6-azo and 9-azo showed a prominent absorption peak with a maximum at a wavelength of about 365 nm, characteristic of the π–π^* transition in the *trans* form of azobenzene. When these solutions of 6-azo and 9-azo are illuminated with UV light for varying time intervals of 5, 8 and 13 min, a gradual decrease in the peak at $\lambda_{max} = 365\ nm$ is observed. This shift indicates the ongoing photoisomerization in azobenzene units. During this process, the stable *trans* form of azobenzene becomes converted to the *cis* form and a weak peak around $\lambda_{max} = 450\ nm$ grows instead, corresponding to the n–π^* transition of the *cis* isomer.

Although the cis form is already the higher-energy configuration, it still absorbs light via the n–π^* transition. Here, an electron is excited from a non-bonding (n) orbital, typically localized on the nitrogen atom, to an anti-bonding π^* orbital. In contrast, the stronger π–π^* transition seen in the trans form involves excitation of an electron from a bonding π orbital to an anti-bonding π^* orbital—this transition is generally more allowed and appears at shorter wavelengths (higher energy). The energy ab-

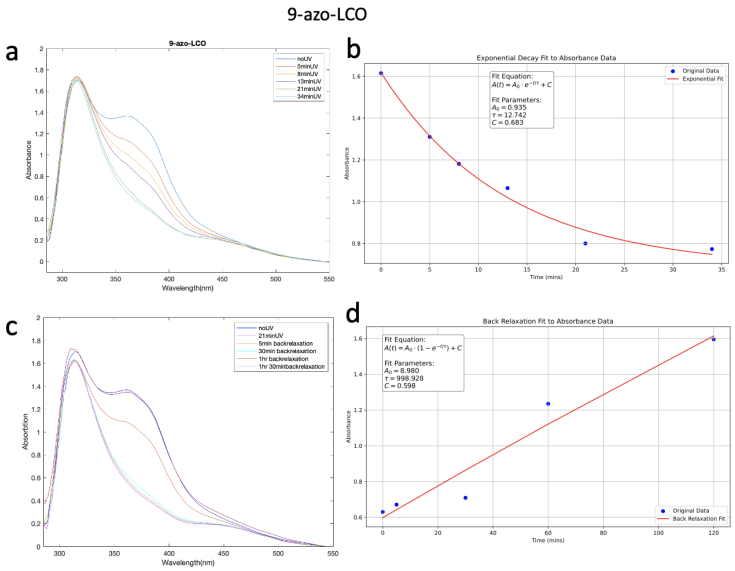

Figure 5.6: (a) UV-visible absorption spectra of 9-azo-LCO showing changes in absorbance with no UV irradiation and at successive intervals of UV exposure. (b) Corresponding plot of absorbance versus time at λ_{max}= 365nm under UV irradiation, indicating the progressive photoisomerization of the sample.(c) UV-visible absorption spectra illustrating the back relaxation of 9-azo LCO after 21 minutes of UV exposure, captured over various time intervals. (d) Corresponding plot of absorbance versus time for the back relaxation at λ_{max}= 365nm showing the gradual return to the initial state following UV-induced isomerization.

sorbed by the cis isomer via the n–π^* transition does not typically lead to further photoisomerization, but is instead dissipated non-radiatively as heat or vibrational relaxation. The appearance of this peak confirms the accumulation of the cis isomer in the system and reflects the approach to a photostationary state under continued UV exposure.

Since our primary interest is studying the photoisomerization behavior in the solid state, thin films of azo-LCOs and azo-LCEs were prepared on glass slides using the spin coating method. After coating, the solvent was evaporated under vacuum to ensure dry solid-state samples. LCOs and LCEs were irradiated with UV light (λ_{max}= 365nm, 5.5 mW/cm^2) for different time intervals, and their absorption spectra were recorded. To study the back-relaxation, all samples were shone with UV light (intensity as above) for 21 minutes and then the samples were left in the dark to see the *cis*-form converting back to *trans*-form. The absorbance peaks at 365 nm and 450 nm are monitored to track the photoisomerization and back-relaxation processes, respectively.

Both 9-and 6-azo-LCOs (figure 5.6 and 5.7), took around 21 minutes as optimal UV exposure time for the peak at 365 nm to completely disappear, which should ideally indicate complete conversion of *trans* to *cis*. To quantitatively analyze the kinetics, the decay in absorbance at 365 nm was fitted to an exponential decay model:

$$A(t) = A_0 \cdot e^{-t/\tau} + C \tag{5.1}$$

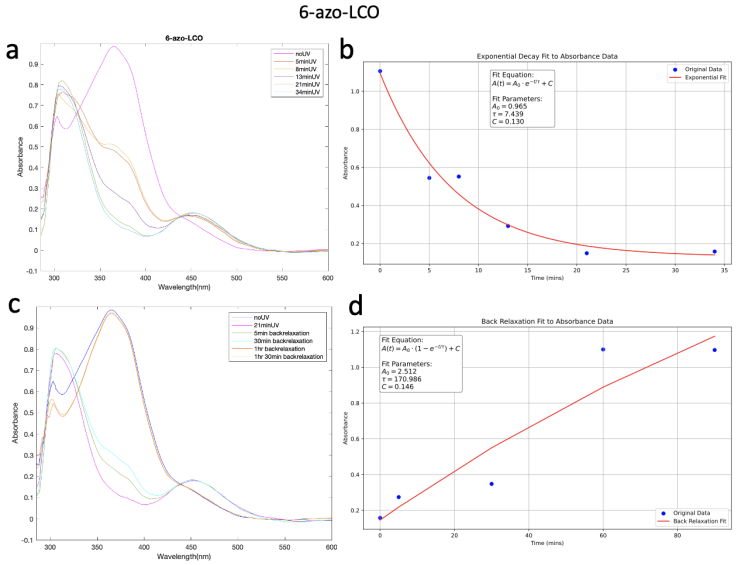

Figure 5.7: (a) UV-visible absorption spectra of 6-azo-LCO showing changes in absorbance with no UV irradiation and at successive intervals of UV exposure. (b) Corresponding plot of absorbance versus time at λ_{max}= 365nm under UV irradiation.(c) UV-visible absorption spectra illustrating the back relaxation of 6-azo-LCO after 21 minutes of UV exposure, captured over various time intervals. (d) Corresponding plot of absorbance versus time for the back relaxation at λ_{max}= 365nm.

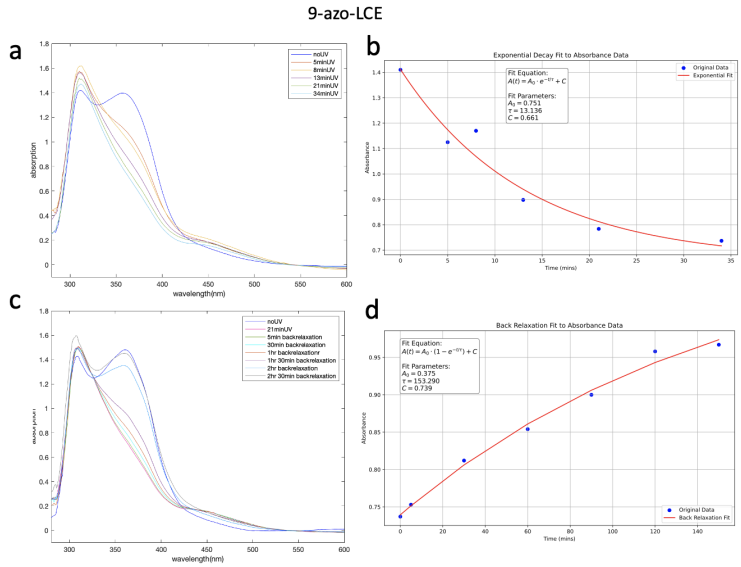

Figure 5.8: (a) UV-visible absorption spectra of 9-azo-LCE showing changes in absorbance with no UV irradiation and at successive intervals of UV exposure. (b) Corresponding plot of absorbance versus time at λ_{max}= 365nm under UV irradiation.(c) UV-visible absorption spectra illustrating the back relaxation of 9-azo-LCE after 21 minutes of UV exposure, captured over various time intervals. (d) Corresponding plot of absorbance versus time for the back relaxation at λ_{max}= 365nm.

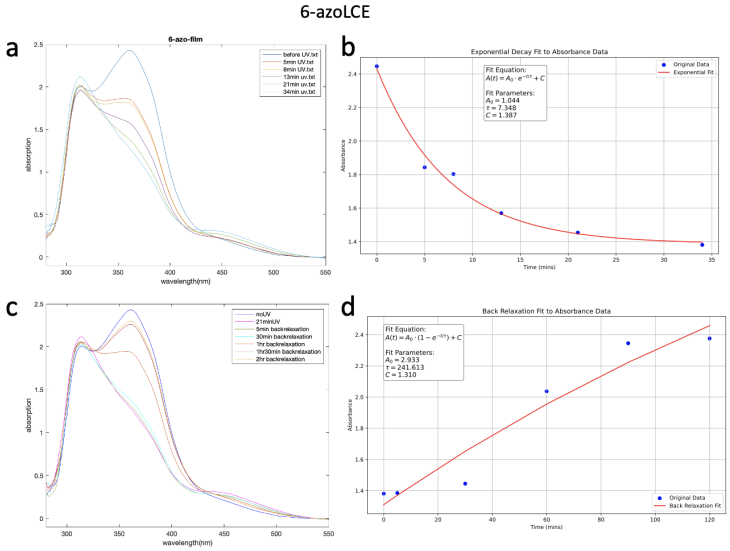

Figure 5.9: (a) UV-visible absorption spectra of 6-azo-LCE showing changes in absorbance with no UV irradiation and at successive intervals of UV exposure. (b) Corresponding plot of absorbance versus time at λ_{max}= 365nm under UV irradiation.(c) UV-visible absorption spectra illustrating the back relaxation of 6-azo-LCE after 21 minutes of UV exposure, captured over various time intervals. (d) Corresponding plot of absorbance versus time for the back relaxation at λ_{max}= 365nm showing the gradual return to the initial state following UV-induced isomerization..

Here, $A(t)$ is the absorbance at time t, A_0 is the amplitude of the decay, τ is the time constant that characterizes the rate at which the absorbance decays and C is a constant representing the baseline offset. In this context of photoisomerization, τ provides a measure of how quickly the system undergoes *trans*-to-*cis* isomerization. A smaller τ value indicates a faster response, meaning the azobenzene system reaches its new state more rapidly. In contrast, a larger τ corresponds to slower kinetics.

For 9-azo-LCO, the fit yielded a time constant $\tau \approx 12.74$ *minutes*, while for 6-azo-LCO $\tau \approx 7.44$ *minutes* . These values suggest that 6-azo-LCO undergoes a faster *trans*-to-*cis* under UV light compared to 9-azo-LCO.

The back relaxation in the dark was modeled using the exponential growth function:

$$A(t) = A_0 \cdot \left(1 - e^{-t/\tau}\right) + C \tag{5.2}$$

Here, $A(t)$ is the absorbance at time t during relaxation, A_0 is the amplitude of recovery, τ indicates how quickly the thermal back-relaxation occurs and C is the baseline absorbance at the starting point of the recovery. A smaller τ means the *trans*-form reappears more quickly, while a larger τ indicates a slower recovery. However, in both 9-azo- and 6-azo-LCOs, the back-relaxation process did not fit the exponential growth model particularly well. One possible reason for this is the solid state of the samples: the oligomers are spin-coated onto glass slides. In the solid state, the mobility of the oligomer chains are limited compared to solution-phase environments. This restricted mobility can cause slower or more variable relaxation rates, leading to deviations from ideal exponential behavior. Additionally the molecular packing

and, the interaction with the glass substrate may introduce heterogeneity in the local environments, resulting in a broader distribution of relaxation time constants. These factors could collectively contribute to the poor fit and suggest more complex kinetic models might be required for describing back relaxation in these solid-state LCO systems.

In contrast to the LCOs, LCEs showed an optimal UV irradiation time of 34 minutes for the absorbance peak at 365 nm to fully disappear (figure 5.8-5.9). This extended exposure time suggests a slower isomerization process in the crosslinked network compared to the oligomer systems.

The exponential decay fitting (Eq.5.1) yielded a $\tau \approx 7.35$ *minutes* for 6-azo-LCE and $\tau \approx 13.14$ *minutes* for 9-azo-LCE. As with the LCOs, the 6-azo-LCE exhibited a faster isomerization rate. Despite the longer total irradiation time required for LCEs to reach equilibrium, the fitted time constants indicate that photoisomerization proceeds relatively quickly once it begins within the LCE network.

Back-relaxation in the dark was modeled using Eq.5.2 and, unlike the LCOs, the data for both LCEs fit this model more better. For 6-azo-LCE, the fit yielded $\tau \approx 241.6$ *minutes*, while for 9-azo-LCE it was $\tau \approx 153.3$ *minutes*. The improved fit quality suggests that the crosslinked network in LCEs facilitates more uniform relaxation behavior. Although both LCEs and LCOs are spin-coated onto glass substrates, the key difference lies in their bulk chain structure. LCEs possess a covalently crosslinked network that distributes mechanical strain and molecular motions more evenly throughout the film, minimizing local heterogeneities. In contrast, LCOs, lacking such crosslinking, exhibit greater molecular packing disorder and are more susceptible to heterogeneous relaxation dynamics. This results in a distribution of relaxation times and poor fitting to a simple exponential model.

5.4 Actuation studies in 6-azo LCE sheet

5.4.1 Preparation of LCE sheets for actuation

In order to achieve good orientation and monodomain formation of a 6-azo-LCE sheet, I barcoated highly concentrated 6-azo-LCO solution in DCM on a glass slide that was pre-coated with PVA. This bar-coated glass slide was then kept in the oven to evaporate the solvent from LCO for 30 minutes. The LC precursor solution also contained a photoinitiator, Sinocure 784 (Sn784), which absorbs light at around 490 nm. After drying, the coated LCO film was irradiated with blue light (emission above 450 nm) for 10 minutes to initiate weak crosslinking. Following this initial photopolymerization step, the edges of the LCE sheet were carefully cut with a scalpel and only the part of the sheet with a uniform thickness was secured. This is then transferred in to a water bath to facilitate the removal of LCE sheet from the glass slide. As the glass slide is coated with PVA, it gets dissolved in water making it easier to detach the LCE sheet from the glass. Once detached, The LCE sheet was dried, stretched, and exposed to a second irradiation of >450 nm for about 30 minutes. The second photo-polymerization helps to lock the LCE sheet in its stretched state, ensuring that the LCE forms a approximate monodomain structure. A segment of LCE sheet prepared were observed with POM to ensure monodomain sheets are formed. By rotating

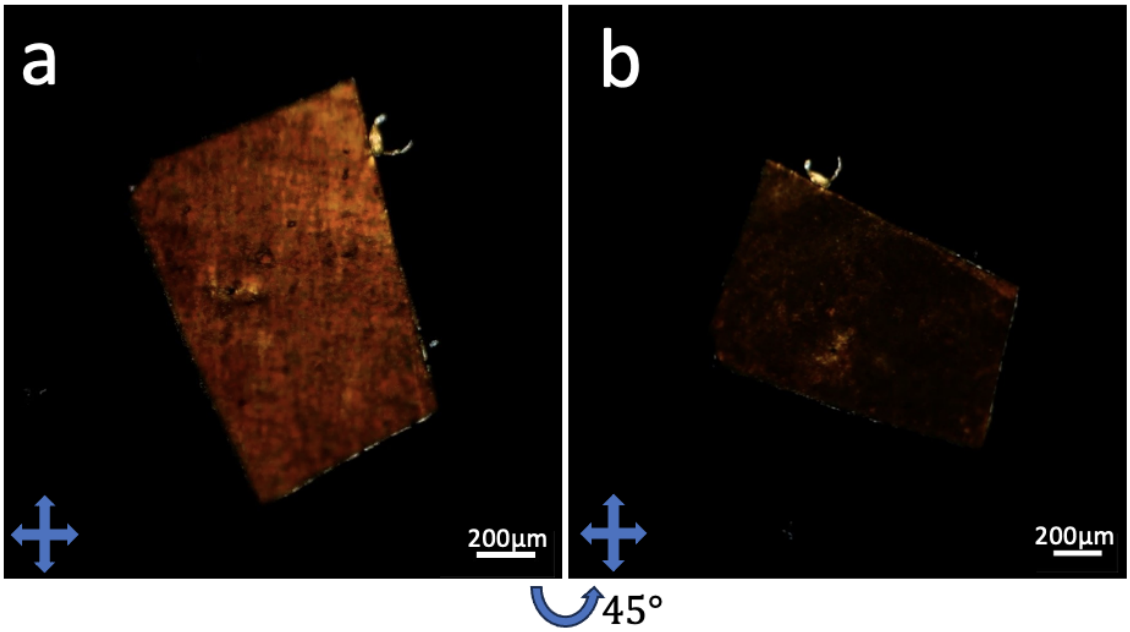

Figure 5.10: POM images of the monodomain sheet between cross-polarizers. a)shows birefringent image, b)shows when the film is rotated 45°.

the LCE film by 45°from its highly birefringent position, I checked whether the film became dark when rotated, and the results, as seen from figure 5.10, confirmed the average monodomain structure of the LCE sheet.

However, these LCE films were transitioning to the polydomain state within the nematic phase on repeated heating and cooling cycles. Strong actuation under UV radiation is observed in fresh samples with monodomain alignment as a result of the initial well-ordered structure, but fatigue was observed over multiple cycles. The likely reason for this behavior lies in the network memory established during the first crosslinking step. Although the sample was dried before polymerization, it is possible that residual solvent remained in the system, and since the film had not yet been stretched at that stage, the network may have been fixed in a relaxed, polydomain-like configuration. The subsequent stretching and secondary crosslinking step, though aimed at locking in alignment, may have only partially overwritten the original network structure. Consequently, on thermal cycling, the system tends to revert to its initially imprinted, lower-energy polydomain configuration rather than maintaining the stretched alignment.

5.4.2 Monodomain azo-LCE films

To address the fatigue of above prepared azo-LCE films, the cross linking density was increased by introducing a tetra-thiol crosslinker, pentaerythritol tetrakis(3-mercaptopropionate) (PETMP), into the synthesis. The modified process, described in detail in Chapter 3 and summarized in figure 5.11, employed two thiol-Michael addition reactions following the protocols of He et al. [10] and Jeong et al [17]. The first reaction linked mesogenic monomers containing azobenzene and phenyl benzoate cores to chain extenders (EDDET) in the presence of triethylamine (TEA) as a catalyst. This step produced LCOs with functional acrylate end groups.

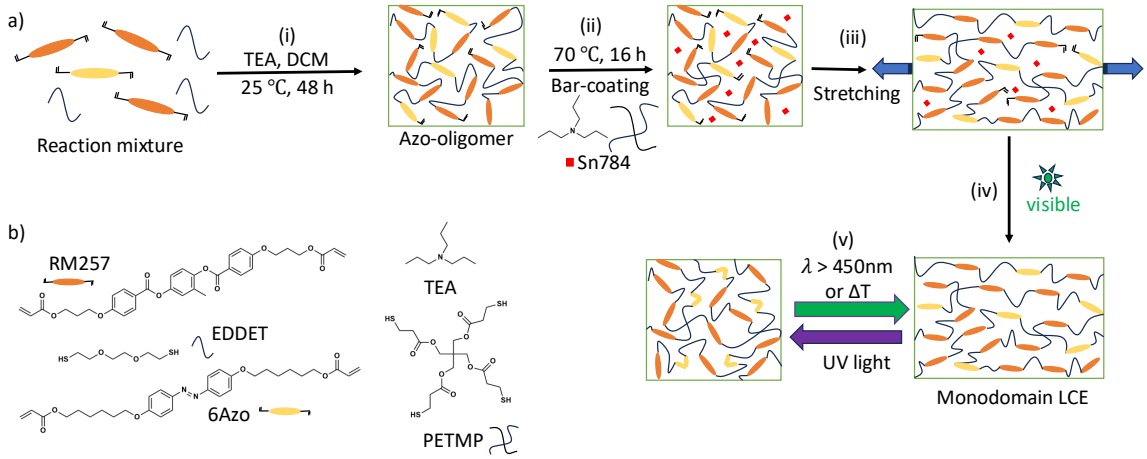

Figure 5.11: a)Schematics of: (i) first Michel-addition reaction using TEA as catalyst and DCM as solvent to form azo oligomers. (ii) Second thiol-Michel addition reaction by adding PETMP, Sn784 and catalyst to the oligomer followed by barcoating on a PVA coated glass slide. (iii) Uniaxial stretching of the first weakly crosslinked network followed by (iv) blue light irradiation for 12 hours in the stretched state. (v) Shows the photoactuation in monodomain azo-LCE film by UV irradiation and back relaxation triggered by visible light. b) Chemical structures of the reactants used in the preparation of azo-functionalized LCEs.

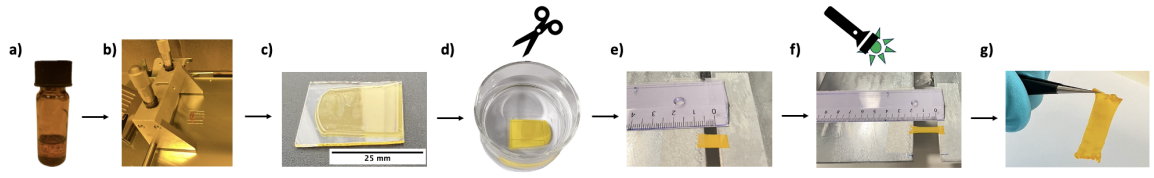

Figure 5.12: Photographs showing key steps in monodomain LCE preparation. a) Vial containing azo oligomer+PETMP+TEA+Sn784+DCM. b)Bar coating of the reaction mixture on a PVA coated glass slide. c) Cured film after annealing at 70°C for 16 hours. d) LCE films in hot water bath to facilitate removal of film from the glass followed by cutting the edges with a scalpel. e) Unstretched film placed on the stretching device by securing both the ends using tapes. f) Mechanically stretched film to 300% of its original length and irradiated with visible light for 12 hours to lock in the alignment by photo-crosslinking. g) Monodomain azo-LCE sheet after removing from the stretching device.

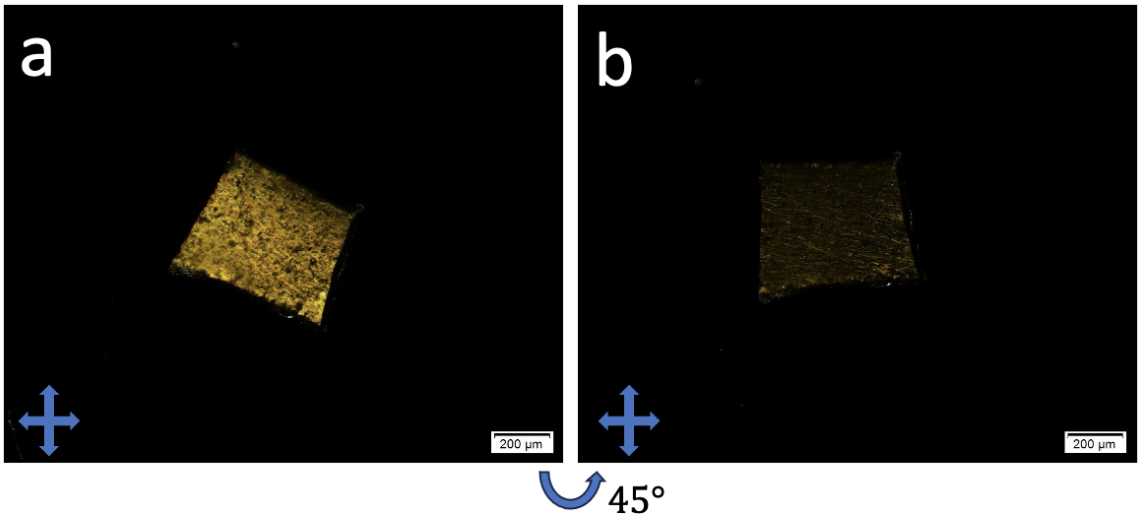

Figure 5.13: POM images of the monodomain LCE sheet between cross-polarizers at room temperature with the sheet being rotated by 45°.

To enable crosslinking without triggering *trans-cis* isomerization of the azobenzene moieties, Sn784 was added. Sn784 absorbs maximally around 490 nm and initiates free radical polymerization of excess acrylate bonds upon exposure to blue light (emission above 450 nm). Without further alignment, this process would result in polydomain LCEs. To achieve monodomain alignment, a second thiol-Michael addition reaction was performed, combined with mechanical alignment. The process involved dissolving LCOs and Sn784 in DCM for easier handling. PETMP was added to this mixture along with TEA dissolved in DCM to initiate the second thiol-Michael addition reaction. This step created a lightly crosslinked first network, allowing for mechanical stretching before final crosslinking. The LCO and PETMP mixture was stirred thoroughly to ensure homogeneity and then immediately bar-coated onto a PVA-coated glass slide to 130μm thickness. The film was cured at 70°C for 16 hours in a vacuum oven to remove DCM and complete the first network formation. During this process, the film transitioned from the isotropic DCM-swollen film to a polydomain LCE.

To release the film, the glass slide was immersed in hot water, dissolving the PVA layer. After drying, the film was attached to a uniaxial stretching device, where it was stretched to 300% of its original length. The low PETMP concentration ensured sufficient flexibility for this stretching process, aligning the liquid crystal network uniformly along the stretching direction. This step was essential for creating a macroscopically ordered structure, following the dual-network principle established for aligning conventional LCEs by Küpfer and Finkelmann [36]. The key steps of the above mentioned LCE preparations are shown in figure 5.12. The prepared photocrosslinked films were observed between cross polarizers using transmission POM with **n** around 45° from the polarizer and along the polarizer, to confirm uniform alignment of the director **n** along the stretching direction in figure 5.13.

5.4.3 Thermal actuation study with and without irradiation

To study thermal actuation, small pieces of LCE film (30μm thickness) were cut into rectangular pieces and placed on a drop of glycerol on a glass slide placed on a Linkam

hot stage which is mounted on a POM. A series of heating and cooling cycles, first without and then with UV were conducted to analyze the change in width of the film during these thermal cycles.

In the first cycle, the film was heated from 8°C to 80°C at a rate of 2°C/min, reaching a temperature above the clearing point. To account for potential non-equilibrium distortions caused by mechanical stretching during the LCE preparation, we heated the LCE film to the isotropic state. Three complete heating-cooling cycles were conducted to ensure removal of any distortions and stabilize the material structure before the film was exposed to UV light (see figure 5.14). The actuation during this process is quantified by calculating the relative change in the width w of the film along $\mathbf{n}$. The relative width was calculated by dividing the width after deformation w by the reference width w_0, which is the width prior to the first heating. In the temperature versus relative width plot (figure. 5.15), the corresponding LCE actuation function:

$$T \leq T_{NI} : w/w_0 = w^*/w_0(T_{NI} - T)^\gamma + C \tag{5.3}$$

$$T > T_{NI} : w/w_0 = C$$

was fitted to the experimental data. Here w^*/w_0 represents the amplitude, and C is an offset representing the value of w/w_0 during saturated actuation in the fully isotropic state. This function models the actuation as based on the temperature dependence of the nematic order parameter S. To improve the reliability of the fitting results, a preliminary fit is performed on the first heating run with all parameters left free. This step helps determine the appropriate range of the exponent, resulting in $\gamma \approx 0.33$. Using this value, the fit is then refined, and all subsequent fits to data without UV irradiation are carried out with $\gamma \approx 0.33$. The fits closely match the experimental data, except near the transition region, where the smeared-out nature of the transition cannot be accurately captured by the above equation. This behavior is commonly observed in LCEs and was originally described by Schätzle and Finkelmann [85] as an artifact caused by the LCE acting as a mixture of LC mesogens and a polymer network.

During the first heating of the pristine sample, the clearing temperature appears slightly higher than expected ($T_{NI}^{t\uparrow} = 46.6 \pm 0.3$°C), as shown in the red data set in figure 5.15. This indicates a small deviation from the equilibrium configuration that remains from the stretching process prior to crosslinking, causing the first heating run to be used as an annealing step. In the first cooling run (blue data set in figure 5.15), the transition temperature to the nematic state decreases ($T_{NI}^{t\downarrow} = 42.1 \pm 0.1$°C), and the final cooled width is slightly smaller than the initial width w_0 confirming that this represented the initial non-equilibrium state. After the first heating run to the isotropic state, the width of the film reduces to 62% of its initial width, while upon cooling it recovers about 92% of its initial width. Subsequent heating and cooling cycles ($T_{NI}^{t\uparrow} = 44.3 \pm 0.2$°C and $T_{NI}^{t\downarrow} = 42.5 \pm 0.2$°C respectively) follow nearly identical curves, showing slight thermal hysteresis, with slightly lower transition temperatures during cooling.

Now the width after the first two heating-cooling cycles is treated as the new reference width w_0, representing the annealed ground-state width. The response from the third cycle, normalized to this ground state is considered as the pre-UV response in

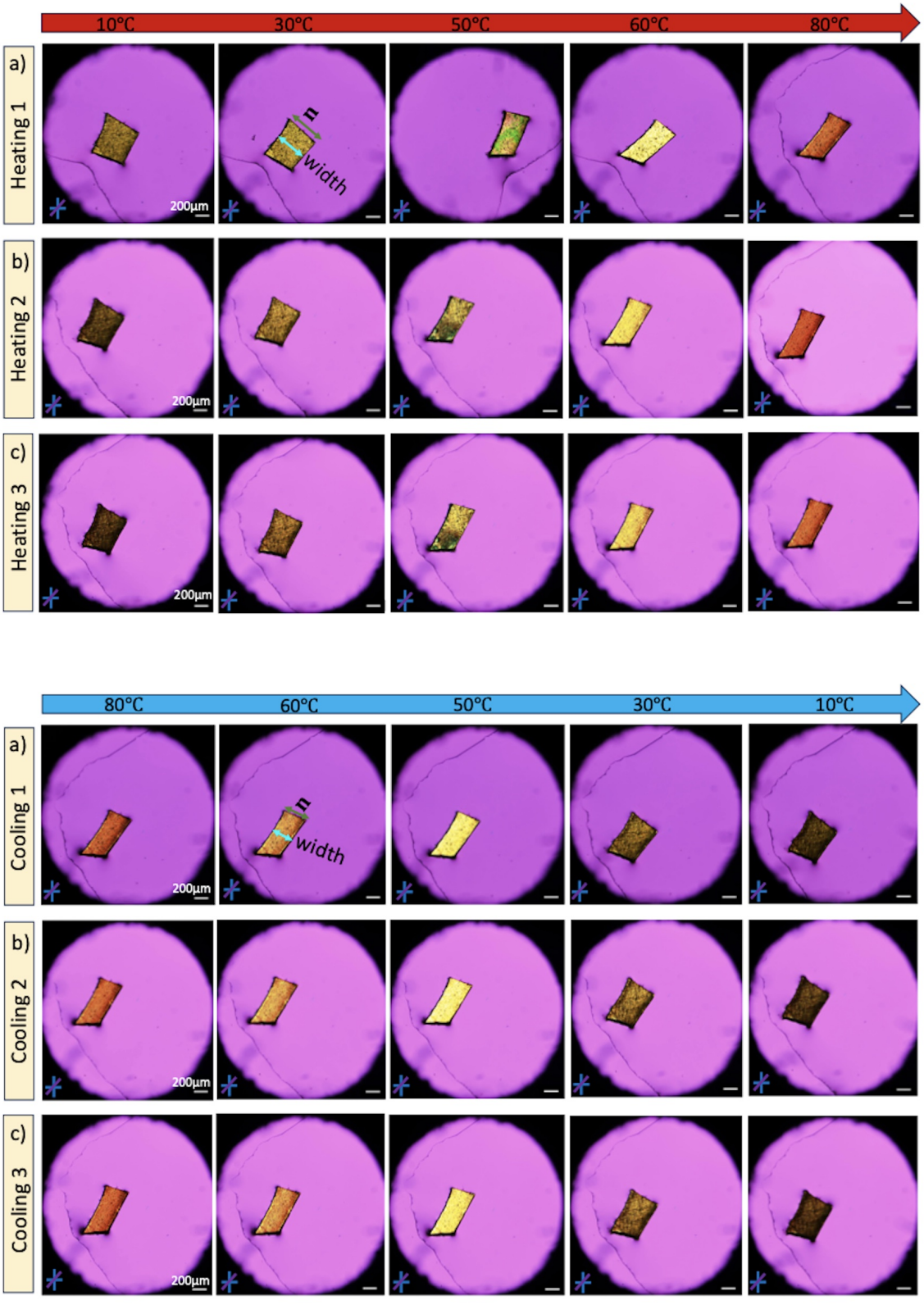

Figure 5.14: POM transmission images of 6-azo-LCE film on glycerol at different temperatures (extracted from the three consecutive heating cycles (top) and respective cooling cycles (bottom)) between crossed polarizers with λ-plate inserted. The width of the sheet and the director alignment are indicated with double arrows.

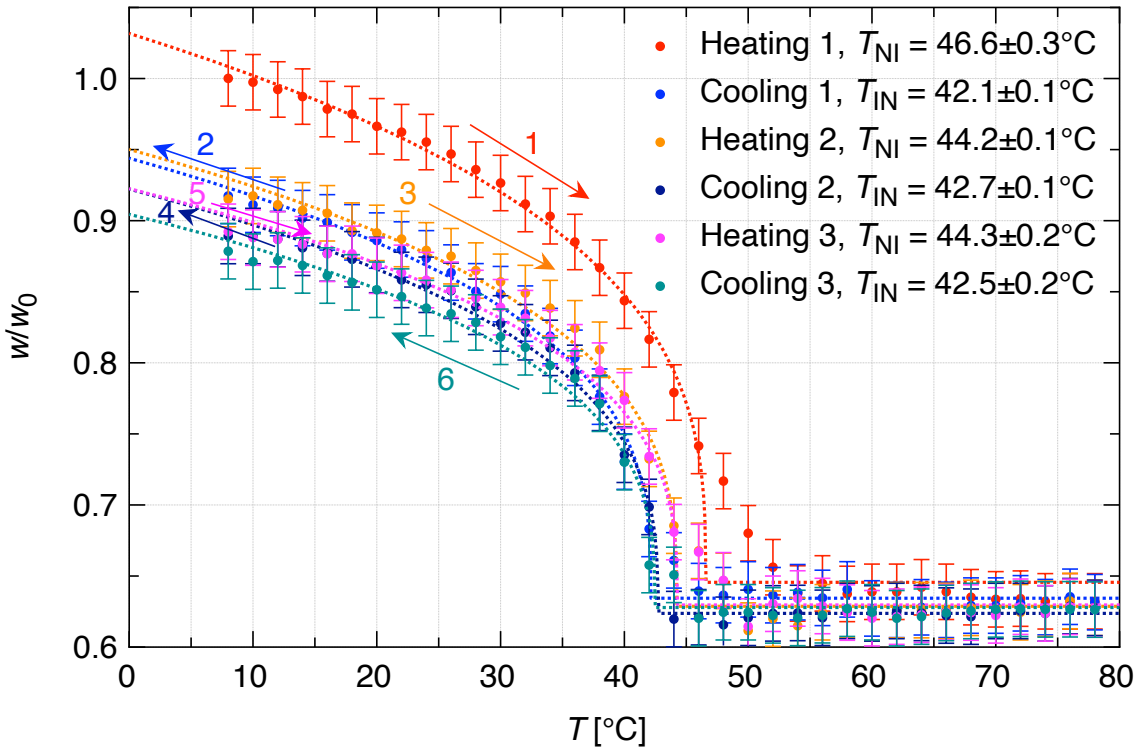

Figure 5.15: Relative width change as measured along **n**, upon the first three consecutive heating and cooling cycles on the LCE film. Error bars reflect the accuracy in relative width determination

figure 5.16c along with the fitting results. The heating run is then repeated while the film is exposed to UV light with an intensity of 5.5 mW/cm^2 placed at ≈ 4 *cm* from the sample. After this UV exposure, the film was cooled back to lower temperatures without any UV. As seen from figure 5.16a-b, The POM observations reveal that, as we heat the film above T_{NI}, it contracts along the **n**, and expands in the perpendicular in-plane direction.

From figure 5.16c, for thermal actuation with UV, we see that the relative width decreases almost linearly until the temperature reaches about 15°C. As heating with UV further continues, the behavior aligns well with the trajectory that can be effectively modeled with the equation 5.3. However, the exponent is increased to $\gamma = 0.5$ to obtain a good fit. Interestingly, now for the heating during UV exposure the T_{NI} is determined to be $T_{NIc}^{\uparrow UV} = 26.7 \pm 0.3$°C. UV irradiation causes *trans-cis* isomerization of the azobenzene moieties in the system. As the population of *cis* isomers increases, the order within the liquid crystal phase is reduced, which results in a decrease in T_{NI} by about 17.6°C. The UV light is then turned off and the cooling behavior without UV is then monitored. The cooling curve post UV exposure recovers the transition temperature of $T_{NIt}^{\downarrow post} = 41.5 \pm 0.7$°C. As expected, the cooling curves shifted compared to the heating curves due to hysteresis.

Above the clearing temperature, the film transitioned into an isotropic state, characterized by weak birefringence shown in figure 5.16a, preventing further actuation. This weak birefringence above T_{NI} suggests that the crosslinks are locked in some long-range order. Further heating to ≈ 80°C is required to decay this birefringence,

but there is no change in the shape of the film.

5.4.4 Athermal Photoactuation of the 6-azo-LCE film

To test the optimum operation temperature of the annealed LCE film used in figure 5.16, photoactuation experiments (UV intensity same as above) were conducted at a series of different temperatures and the results are shown in figure 5.17. Now, the relative width is calculated as w^c/w^t, where w^c is the width along the director

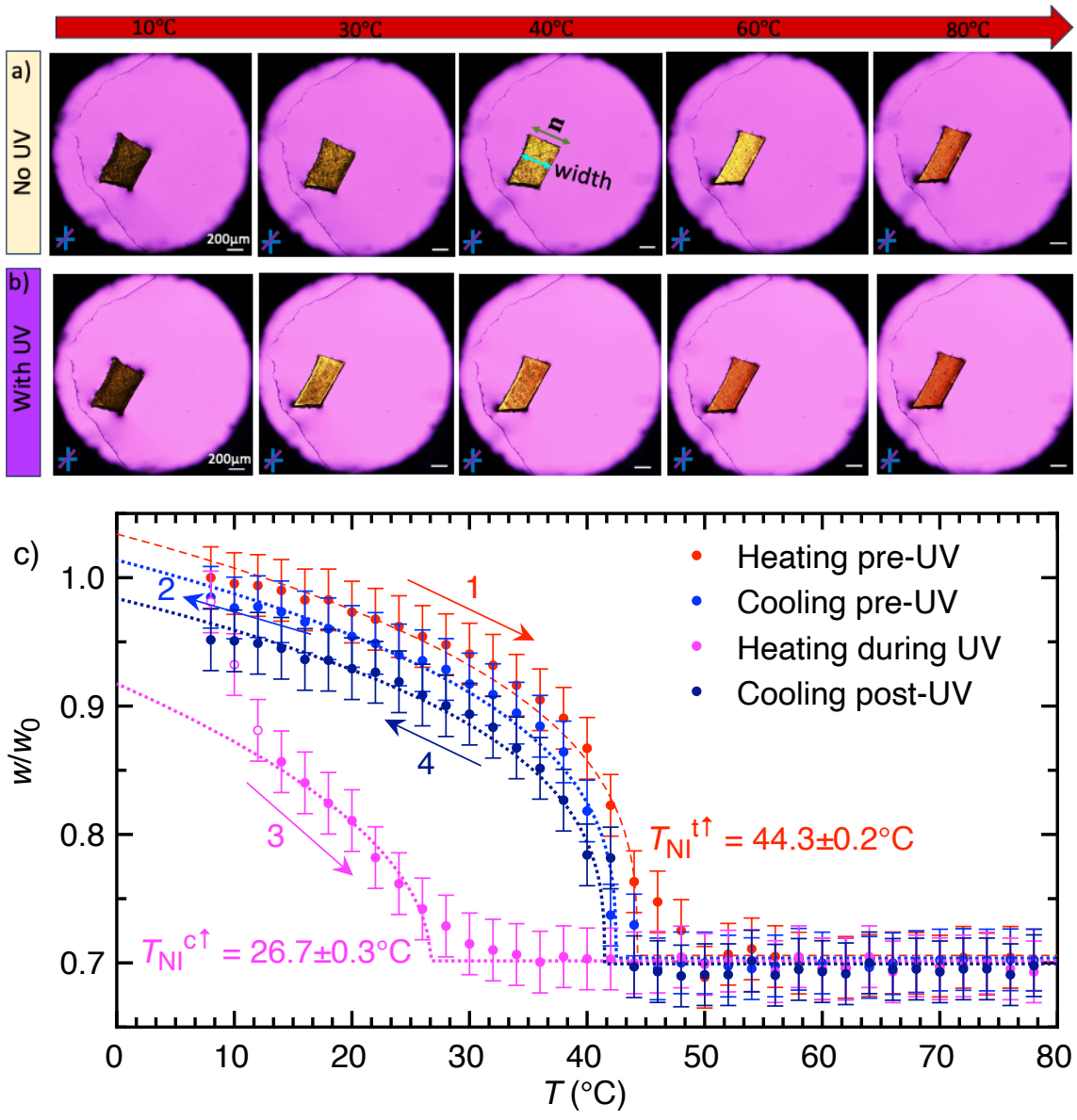

Figure 5.16: Thermoresponsive behavior of an LCE film of thickness 30 μm floating on glycerol.(a)POM transmission images of 6-azo-LCE film at different temperatures between crossed polarizers with λ-plate inserted (a)without and, (b) with UV irradiation. The width of the sheet and the director alignment are indicated with double arrows. (c) Relative width change of LCE film as measured along **n**, upon heating and cooling after annealing, without and during UV irradiation. Error bars reflect the accuracy in relative width determination

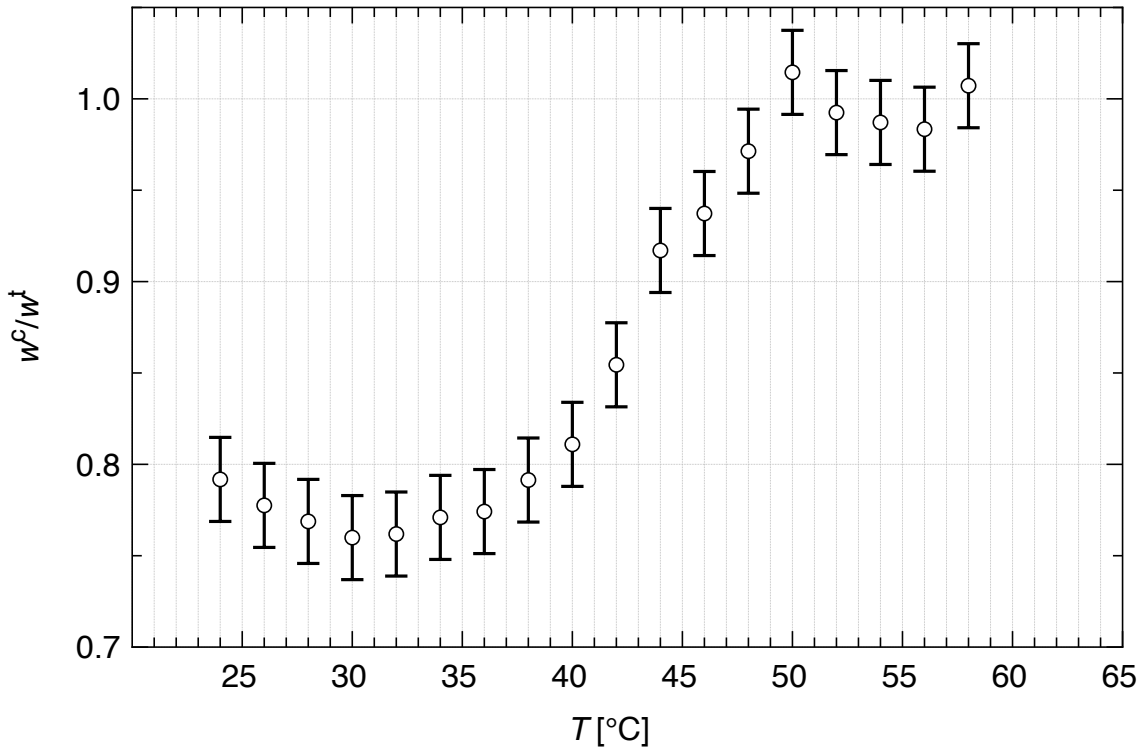

Figure 5.17: Photoactuation of annealed LCE film at different temperatures, quantified using w^c/w^t as metric. Error bars reflect the accuracy in the relative width measurements.

during UV exposure with the azo-moities in *cis*-state and w^t is the corresponding width before UV exposure with the azo-moities in *trans*-state, both measured at the particular temperature of interest. To ensure light induced heating is not affecting the experiments, sufficient time interval (30 s) is given after UV exposure for 15 s before measuring the width. Also, the glycerol bed on which the film is placed helps in effectively dissipating any heat caused by UV light.

In figure 5.16c, the strongest photoactuation is obtained around the operating temperature $T^c_{NI} = 27°\text{C}$. From figure 5.17, we see a minimum w^c/w^t at $T = 30°\text{C}$, with similar values for $T = 27°\text{C}$ and $T = 37°\text{C}$. While fitting suggests $T^c_{NI} = 27°\text{C}$ as the ideal operating temperature, experimental data reveal that the film's contraction has not fully saturated at this point. By $T = 35°\text{C}$, the contraction is complete but the film's pre-UV size is slightly smaller than at $T = 27°\text{C}$, reducing the overall effect. At $T = 30°\text{C}$, the difference in the film's width between its *trans*- ans *cis*- form (influenced by UV) is at its maximum, making this temperature the most effective for operation. The findings match well with the expectation based on the theory that the optimum operation temperature for photoactuated LCEs in which only UV-induced reduction of T_{NI} is active should be equal to T_{NIc} as proposed by Lagerwall in [15]. This is because T_{NIc} is the lowest temperature where the material has maximum order S before UV exposure, allowing UV light to fully reduce the order to zero. At higher operating temperatures, the film starts with less order, so UV light has a smaller overall effect. At lower operating temperatures, the film has higher S initially, but UV light cannot reduce the order to zero, again limiting the impact.

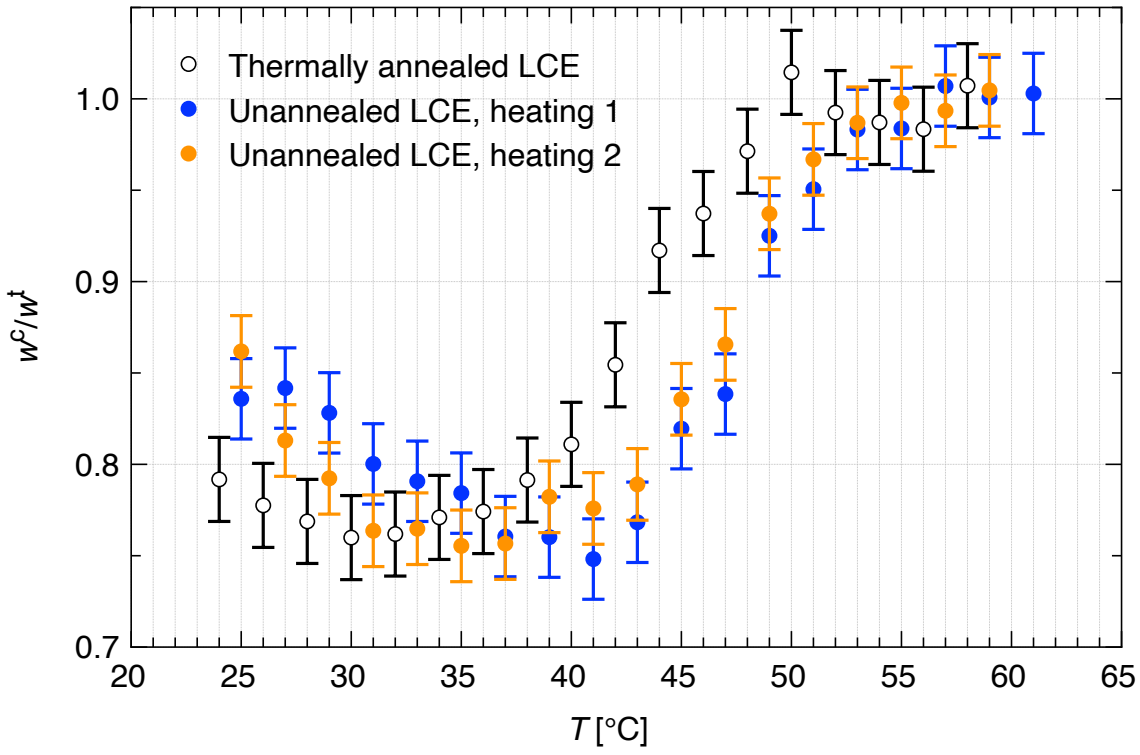

Figure 5.18: Comparison of photoactuation of annealed and unannealed LCE films at different temperatures, quantified using w^c/w^t as metric. Error bars reflect the accuracy in the relative width measurements.

When analyzed how the efficiency of LCE's photoactuation changes on either side of the T_{NIc} it is seen that: On the lower temperature side (below T_{NIc}), the material does not entirely switch to an isotropic state during UV exposure (figure 5.16b-c), leading to a more rapid reduction in actuation efficiency. In contrast, on the higher temperature side (above T_{NIc}), the material switches to an isotropic state during UV exposure, resulting in a slower initial decline in actuation efficiency. This behavior is observed within a range of ± 7°C probed on either side of T_{NIc} in figure 5.17. On the high temperature side, beyond $T_{NIc} + 10$°C, the efficiency drops rapidly, and by $T_{NIc} + 20$°C, the photoactuation is entirely lost as the $w^t \approx w^t$. My project is mainly aimed at using these photoactivated LCEs in biological systems, especially organoids, and needs an operation temperature of $T = 37$°C. At this temperature, the actuation efficiency is $w^c/w^t \approx 0.775$, slightly lower (about 6%) than the maximum efficiency of ≈ 0.76 seen at $T_{NIc}+3$°C . Adjusting the dose of UV can shift the optimal temperature close to $T = 37$°C which could help achieve near-optimal efficiency along with reducing UV intensity that can cause potential harm to living tissues.

To test the photoactuation behavior of an unannealed LCE film, the photoactuation experiments were conducted on a pristine film directly after stretching and photocrosslinking (figure 5.18). For the unannealed LCE, the strongest photoactuation is observed at an elevated temperature ($T^c_{NI} = 41$°C) than the annealed sample. On cooling the film back to 25°C, the photoactuation experiment is repeated to resemble the annealed condition, shown by the orange data set in figure 5.18. Now, the optimum temperature has lowered to 35°C. While this does not reproduce the op-

timum temperature obtained for the thermally annealed LCE, the variation in the optimum photoactuation could reflect differences between individual samples or suggest that thermal annealing alone is more effective in eliminating the non-equilibrium configuration resulting from the mechanical alignment before photocrosslinking.

5.5 Limitations of the photoactuated LCEs

One of the significant challenge in photoactuated LCEs is their narrow operational temperature range [86]. As seen in this study, the maximum effective actuation occurred in a tight window between 27°C and 37°C, a range that is narrow for practical applications where temperature control may be difficult. Moreover, the actuation efficiency drops significantly when the material operates above the transition temperature T_{NIc}. Fine-tuning the crosslinking density may help further to increase the transition temperature to the desired range.

Additionally, another limiting factor is the sample thickness. While increasing the azobenzene content in the LCE can improve photoactuation, it often results in longer response times or limits the sample thickness [38]. The photoisomerization of azobenzene from the *trans*- to *cis*- form happens first at the surface, with the deeper layers responding more slowly. This delay occurs because the UV light must penetrate the entire sample depth, which can lead to inefficient actuation in thicker samples. Therefore, while increasing the azobenzene content offers more strong actuation, it compromises the overall efficiency and speed of response due to the slower light penetration across the material.

Chapter 6

LCEs in organoids: cell viability

6.1 Role of LCE tubes in organoid growth

The responsiveness of LCE to external stimuli such as light and heat can be harnessed to create a dynamic vascular system within organoids that adapts on the basis of environmental needs. As introduced in Chapter 2, their hollow, tubular architectures make them particularly promising for mimicking vasculature and enhancing nutrient and oxygen transport in dense, three-dimensional tissue models. In this chapter, we move from conceptual motivation to experimental validation by assessing how LCE structures with different geometries—tubes, fibers, and sheets—interact with organoids. Specifically, we examine their biocompatibility and how surface curvature affects cell attachment and organoid formation.

6.2 Organoid growth on LCEs with different surface curvature

The LCE precursor solution used for preparing all: LCE sheets, tubes and fibres are identical to that used for LCO2, following the one-pot synthesis detailed in Chapter 3. Briefly, RM257 and EDDET are taken in a vial in the molar ratio 1.1 : 1 and dissolved in dichloromethane (DCM). Dipropylamine (DPA) is then added as a catalyst, and the mixture is kept for reaction $\approx$ 12 hours at 28°C. Once the reaction is complete, 4 wt% of Irg 819 is added into the precursor solution as a photoinitiator, and mixed well. The solvent is subsequently removed using a rotary evaporator. In case of LCE tubes and fibres, 10 wt% aqueous solutions of PVP with 2 wt% Tween 20 are used as inner and outer phases.

6.2.1 LCE sheet preparation

To fabricate the LCE sheet, 40 wt% of LCO2 is dissolved in DCM and bar coated on a glass slide pre-coated with PVA (figure 6.1a). The PVA coating facilitates the easy removal of the LCE sheet from the glass slide post-polymerization. The bar coating technique enables to produce thin uniform LCE films of $\approx$ 30 μm thickness. Following this, the solvent is evaporated by keeping the bar coated glass slide in vacuum oven

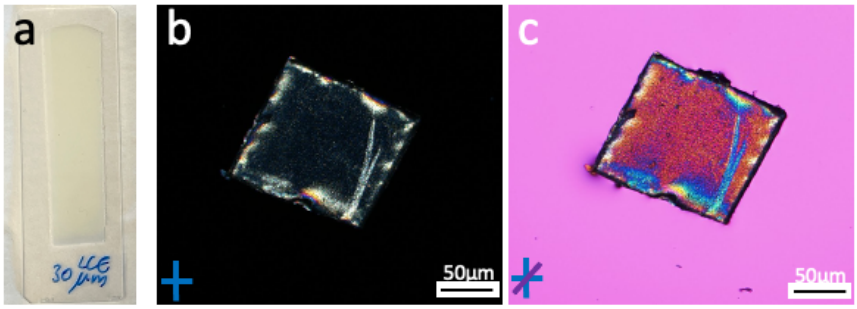

”

Figure 6.1: a) Macroscopic view of LCE sheet barcoated on a glass slide. b) POM image of LCE sheet between crossed polarizers. c) POM image of unaligned LCE sheet with a λ-plate inserted.

for 30 minutes at 40°C. After this, the film is photopolymerized in a UV box for 10 minutes.

The resulting LCE sheets are then cut into small 2x2 cm long sheets and analyzed using POM to examine its alignment. To facilitate cutting, the barcoated LCE sheet on the glass slide is first frozen at -20°C and then cut into desired size using a scalpel while in the glassy state. POM analysis is performed once the LCE sheets return to their normal temperature. Between cross polarizers, as shown in figure 6.1b, the sheets show weak birefringence. The variation in brightness across the field of view suggests the sheet has polydomain alignment. To confirm this, the sheet was also observed between crossed polarizers with λ-plate inserted (figure 6.1c). Interference colors confirm LC domain showing variation in orientation across the sample.

6.2.2 Production of LCE tubes with reduced diameter

LCE tubes were produced using 40 wt% LCO2 in DCM as detailed in Chapter 4. LCE tubes approximately 300 μm were used for cell viability tests.

6.2.3 Production of LCE fibres with reduced diameter

In this case, the nested capillary setup was modified as illustrated in figure 6.2a. The microfluidic setup was simplified to include only two injection points: one for the LCO precursor solution and one for the PVP solution. The interstitial channel previously used for injecting the middle phase in the original nested capillary set up was sealed with epoxy glue.The two phases here are flown in opposite directions until they meet at the capillary junction, where the outer phase flow-focuses the inner phase to create a stable flow. The inlet orifice diameter is chosen as 90 μm, while the outlet orifice has a diameter of 350 μm. To produce fibres with a diameter of approximately 20 μm, an inner phase flow rate of $\phi_i = 2$ mL/h and outer phase flow rate of $\phi_0 = 25$ mL/h were used.

Here, the linear flow velocity of the inner phase -comprising LCO mixture- is increased to achieve thinner fibres. Although this method results in a greater initial jet diameter, the higher flow velocity of inner phase in jetting mode, will delay the Rayleigh-plateau instability, ultimately allowing the formation of thinner fibres. As shown in figure 6.2b,

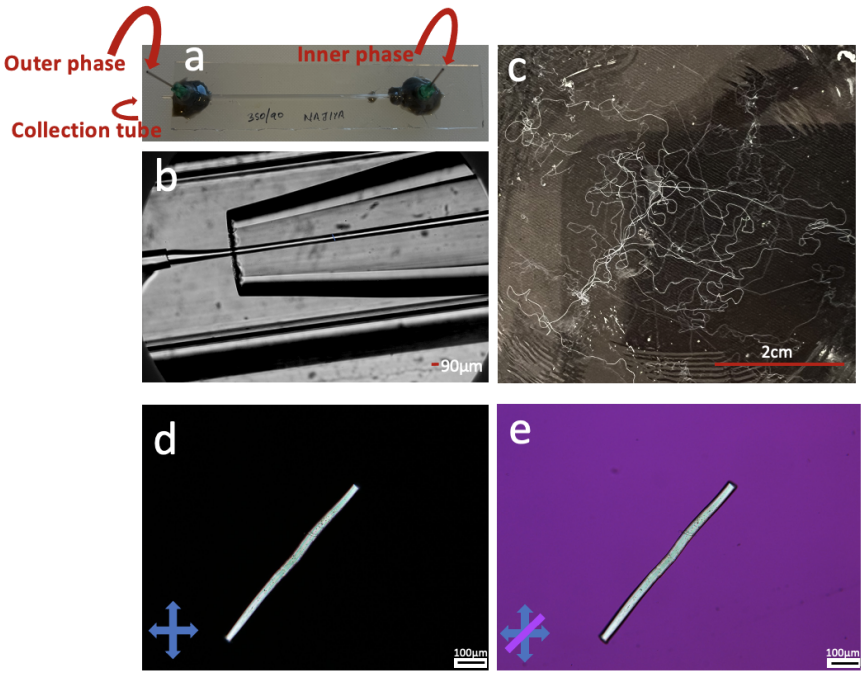

Figure 6.2: a) Microfluidic device used for the production of LCE fibre, b) Microfluidic device junction viewed without analyzer, c)Macroscopic view of long fibres collected in a water bath, d)and e) sections of same LCE fibre observed with POM between cross polarizers and λ-plate inserted.

this method results in the formation of narrow LC jet. This is then polymerized in situ using UV light and collected in a water bath, as shown in figure 6.2c.

Figure 6.2 d and e show POM images of a section of LCE fibre immediately after production, still containing DCM. Between cross polarizer the middle part of the fibre predominately displays greenish color corresponding to first order birefringence on Michel-Levy chart. This indicates that the optical path difference is moderate, and the director alignment in this region is fairly uniform and aligned predominantly along the flow direction. The top and bottom borders appears to have pinkish hues that is found in the second-order region of the Michel-Levy chart, corresponding to a higher optical path difference. This increased birefringence at the edges is due to greater extension of the material along the viewing direction at the sides of the fibre.

When a lambda plate is inserted, the green hue shifts towards turquoise when the fibre is aligned parallel to the optic axis of the λ plate (figure 6.2e), a transition indicative of positive birefringence. Additionally, the faint pink lines observed near the top and bottom borders in the figure 6.2e, confirms the increased birefringence at the edges, consistent with the cross-polarizer observations. Together, these results suggest a non-uniform director alignment across the fibre's cross-section, with a well aligned central region and higher strain or molecular orientation at the edges. These variations in the birefringence and director alignment reflects the interplay between the shear alignment and boundary effects during the microfluidic fabrication of the fibre.

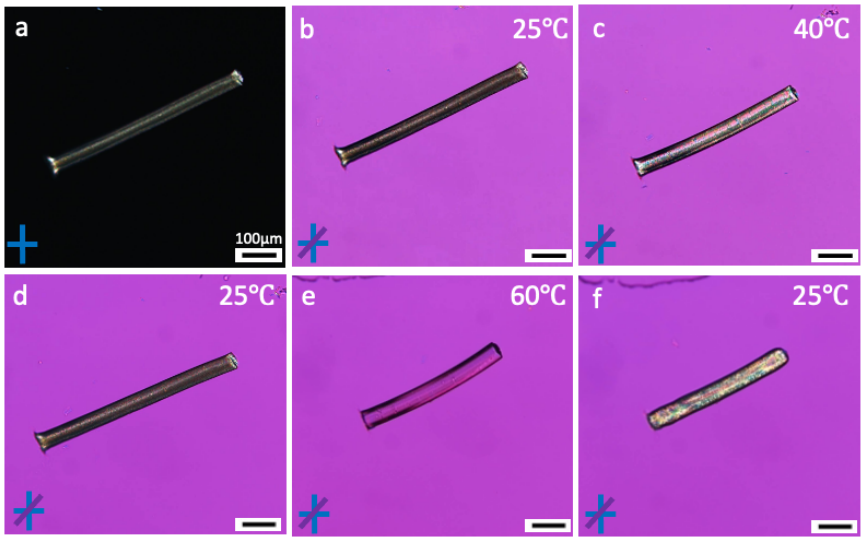

Figure 6.3: Actuation of a longitudinal LCE fibre section observed in transmission POM during heating and cooling. Panel (a) is obtained between crossed polarizers and all other panels have λ plate inserted with the optic axis indicated in (b). Upon heating from 25 to 40 °C (b, c), the section relaxes back to the original shape upon cooling (d). Heating to 60 °C, the section completely turns isotropic and the original section is recovered only very slowly after cooling (e).

POM characterization of LCE fibres during actuation

To study the actuation in LCE fibres, a section of LCE tube fibre was cut and then heated while kept in glycerol and studied using POM, figure 6.3. As the fibre id heated from 25 °C to 40 °C, the fibre reduces in length and expands its diameter. The color of the fibre changes on heating and cooling. The fibre appears to show golden yellow (third order color on Michel-Levy chart) at 25 °C corresponding to high birefringence and high retardation, indicating the fibre is higly aligned in the nematic phase. At 40 °C the color shifts to pink or purple color indicating a reduction in retardation. As the fibre is heated, the alignmnet of LC mesogens becomes less ordered, reduing the birefringence. At 60 °C, the fibre reaches the isotropic phase, where the fibre no longer contributes to birefringence, leaving the magenta color of the λ plate as the color observed. Here the fibre is oriented with its long axis parallel to the optic axis of the λ plate, reducing the overall birefringence compared to the contribution of the λ plate on heating.

As we heat from 25 °C to 40 °C, since the director is oriented along the fibre axis, we also observe the contraction along **n** and expansion perpendicular to it causing the fibre to reduce in length and increases the radius. Upon cooling back to 25 °C, the original length is retained quickly (Figure 6.3d. If we heat the fibre now to 60 °C making the fibre to completely isotropic and then cool back to room temperature (figure 6.3f), it initially does not completely recover it's original length (figure 6.3a and b), but gradually relaxes back to the ground state over time.

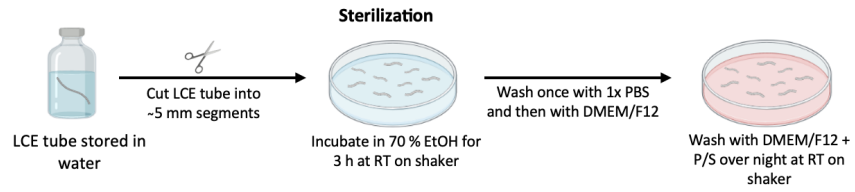

Figure 6.4: Schematic represenation of LCE material preparation before introducing to midbrain organoid culture.

6.2.4 Cell viability test on LCE tubes

After production, all LCE materials were washed in a mixture of 60 vol% ethanol and 40 vol% DCM three times to remove any unreacted oligomers or excess photoinitiators. For each wash, 5 mL of the mixture was placed in a small petri dish, and the LCE materials were immersed for 2 minutes. Afterward, the materials were rinsed twice with distilled water, each time immersing them for 5 minutes. Finally, the cleaned LCE materials were stored in vials containing distilled water. No physical agitation were employed during any of the above washing steps to ensure the LCE materials did not coil over each other. The prepared LCE samples were then handed over to Anna Sophie Zimmermann for cell viability testing, all the results presented in this section are based on her experiments conducted at Luxembourg Centre for Systems Biomedicine (LCSB).

For the cell viability tests, these LCE tubes and fibres were cut into segments of approximately 5 mm in length and the LCE sheets were cut into 5 mm$\times$5 mm squares. These segments were sterilized by incubating them in 70 % ethanol in water (10 mL) for 3 hours at room temperature on a shaker. After sterilization, the segments are washed once with 1X phosphate buffer saline (PBS), followed by a rinse in a medium of DMEM/F12– a type of nutrient-rich solution used to grow and maintain cells. The medium provides a balanced mix of essential nutrients, vitamins, amino-acids, sugars and minerals that cells require for growth. A second wash with DMEM/F12 was done overnight on a shaker. The above mentioned LCE preparation steps are shown in figure 6.4.

To better understand the results presented later, it's important to grasp the process of culturing midbrain organoids (MOs). The process begins with specialized cells called human ventral midbrain neuroepithelial stem cells (hvNESCs), which are a type of early-stage stem cell that can develop into various brain cells. These cells are first grown in a dish with a nutrient-rich solution until they reach approximately 80% confluency. Once the cells are ready, they are detached using an enzyme called Accutase, which gently separates them from the dish. The detached cells are then transferred to a tube containing a cell culture medium called DMEM/F12.

Next, the cell mixture is centrifuged to collect the cells at the bottom of the tube. The liquid above is carefully removed, and the concentrated cells are re-suspended in fresh medium. These cells are then seeded into ultra-low adhesion 96-well plate (Merck, CLS3474) designed to encourage the formation of 3D clusters. After seeding, the plates are gently spun to help the cells settle at the bottom, forming small spherical clusters known as spheroids.

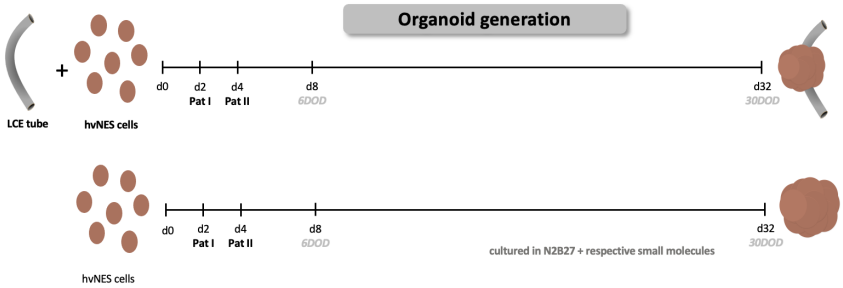

Figure 6.5: Schematic representation of organoid culturing from day 0 to day 32.The first panel illustrates the introduction of LCE tubes to stem cells on day 0. Key stages are marked, showing the timing of patterning and maturation solutions introduced to the culture. The final panel shows growth progression of control midbrain organoids.

On day 2 and day 4, the medium is replaced with patterning solutions, which are mixtures of signaling molecules and growth factors designed to support the cells' growth and guide their development into midbrain structures. By day 8, the medium is switched to a maturation solution, which supports the final stages of development into midbrain-like organoids. This maturation medium is refreshed regularly until day 32, when the organoids are considered fully developed. A schematic representation of the above process is given in figure 6.5.

LCE materials were introduced to the culture of organoids during the seeding stage, and everything was spun down together. By day 30 of differentiation, six out of eight MOs cultured with LCE tube were attached to them (figure 6.6).

In figure 6.6a, the organoids appears to have grown adjacent to the LCE tube section. In contrast, figure 6.6b shows a control organoid without an LCE tube. MOs with LCE tubes have about 48% of the volume of the control MOs. The size comparison in figure 6.7c confirms that the control organoids are significantly larger than the organoids grown with LCE tubes. The statistical significance is indicated by four asterisks (****), which correspond to a p-value of less than 0.0001. The p-value represents the probability of observing the size difference purely by chance if there were no real effect. A smaller p-value indicates stronger evidence against this idea of random chance, and four asterisks denote an extremely small p-value, signifying the difference in size between the control MOs and MOs with LCE tubes is extremely unlikely to be due to random variation, showing a very strong effect caused by the presence of the LCE tube. The LDH (lactate dehydrogenase) analysis measures cell membrane integrity to assess cell viability, a common method for assessing cell viability. LDH is an enzyme released into the extracellular space when cells are damaged or undergo lysis, making its concentration a marker for cellular damage. Higher LDH release typically implies more cell damage or stress. The results in figure 6.7d show that LDH levels of control organoids are lower compared to those with LCE tubes. Although LDH levels are slightly elevated in organoids grown with LCE tubes, the difference is not statistically significant, denoted by "ns" (not significant). To determine statistical significance, a t-test was conducted. The t-test compares the average LDH levels between the two groups and helps determine whether the difference is large enough to be considered unlikely to have happened by chance. Since the graph indicates "ns" for no significant difference, it suggests that while LCE tubes may cause

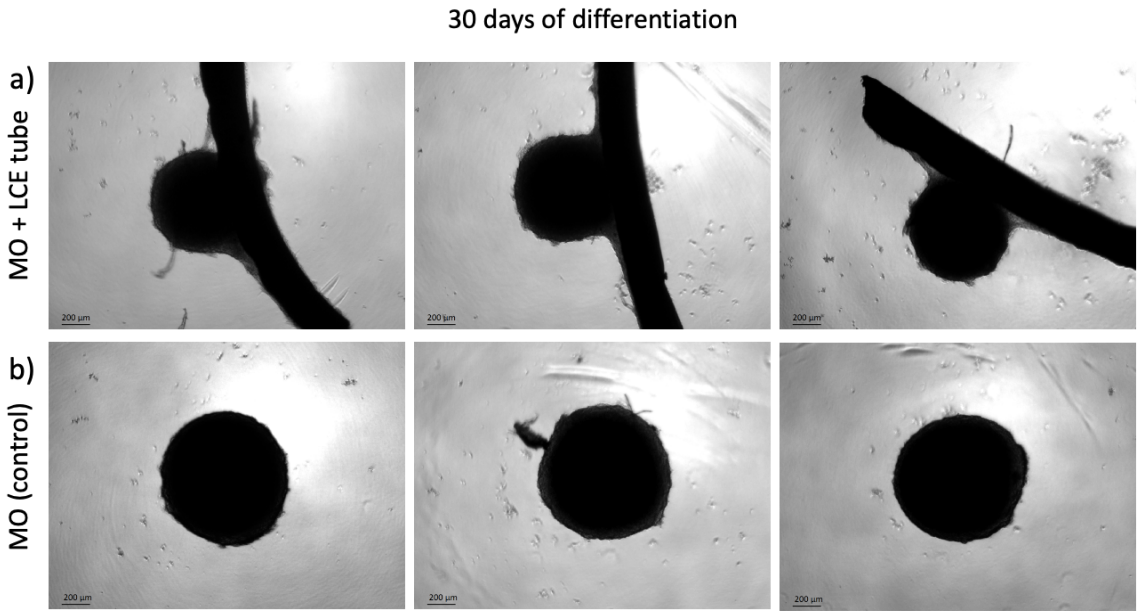

Figure 6.6: Microscopic images of LCE tubes in MOs after day 30 of differentiation. The second panel shows control MOs.

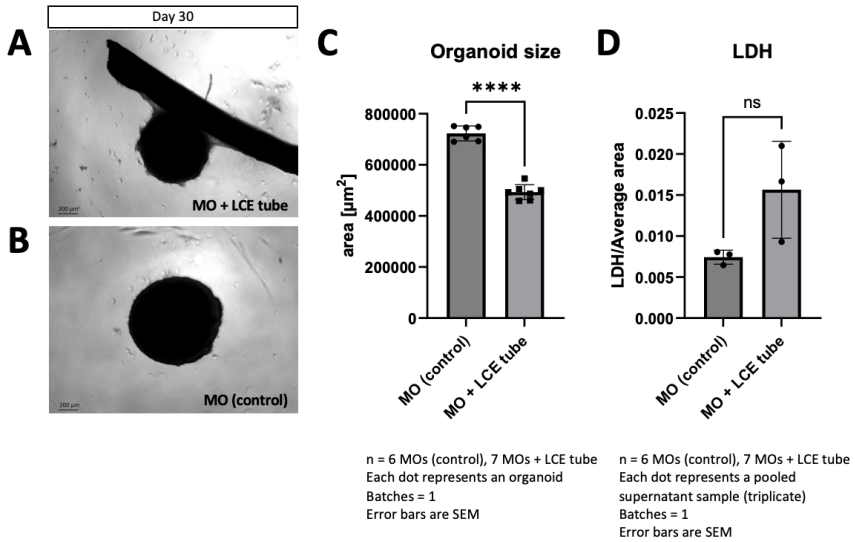

Figure 6.7: Microscopic images of a)MO cultured with LCE tubes and b)control MO on day 30 of organoid culturing. c)Organoid size analysis and, d)LDH analysis of MO with LCE tube and MO control.

a slight increase in cell damage or stress, it is not enough to significantly affect cell viability.

Overall, large-diameter LCE tubes influence the size and maybe the morphology, but they do not drastically affect the cell health or viability.

6.2.5 Cell viability test on LCE tubes, sheets and fibres

To understand how different LCE geometries influence the cell behavior, organoid formation and overall viability, LCE tubes (new set but from the same batch mentioned in the previous section), fibres and sheets were cultured with the organoids. The same protocol that is detailed in above section is followed here. The LCE tubes were cut into smaller segments to prevent it from clustering during centrifuge step. The LCE fibres are thin and flexible making it difficult to cut in smaller pieces compared to tubes. As a result, fibres which are approximately 5 mm in length tend to aggregate. This occurs because the LCE materials, being denser than the aqueous medium, do not remain suspended and instead sink to the bottom of the well, forming a clump due to their increased density and tendency to adhere to each other.

In contrast, the 5 mm long LCE hollow tubes do not experience this clustering issue. While both structures have cylindrical outer geometries, the tube's hollow architecture may influence their behavior in suspension. One possible explanation is that the tubes, being larger in diameter and lower in mass density per unit length, sediment differently under centrifugation compared to the thinner, denser fibers. This difference could potentially reduce their tendency to settle quickly or cluster to itself.

When cultured on flat LCE sheets, the cells tend to form multiple smaller organoids rather than a single larger one. This may reflect the influence of geometry: the flat sheet offers a large, continuous surface for cell attachment but lacks the three-dimensional curvature that could support wrapping or encapsulation by the organoid. While the LCE surface appears conducive to cell adhesion and growth, feedback from Anna indicated that the sheet segments used were still too large for cells to grow around and form a single complete organoid. Therefore, although curvature may not be essential for cell adhesion itself, it likely plays a key role in enabling cells to wrap around organize into three-dimensional, compact organoid structures.

In contrast, cells cultered on highly curved surfaces, like thin fibres and tubes, the cell culture behaved very differently. In these, the cells showed a tendency to remain as more compact clusters resulting in single larger organoids. This indicate that high curvature LCE substrates may serve as a way to form single larger organoids. Also, some LCE fibres were found integrated into the MOs after 30 days of culturing.

The results described above are based on a single experiment involving 16 wells with LCE sheets, 16 wells with LCE tubes and 16 wells with fibers. To confirm these observations, additional tests are currently underway using three batches of LCE tubes, sheets, and fibers, each containing 60 loaded wells. The results of these trials are awaited and could not be included as part of this thesis. For these new trials, the LCE sheet dimensions were reduced to 2 mm $\times$ 2 mm to minimize the chance of the 30 μ sheets rolling over themselves and sticking. The fiber length was also shortened to approximately 2 mm to reduce clumping during centrifugation.

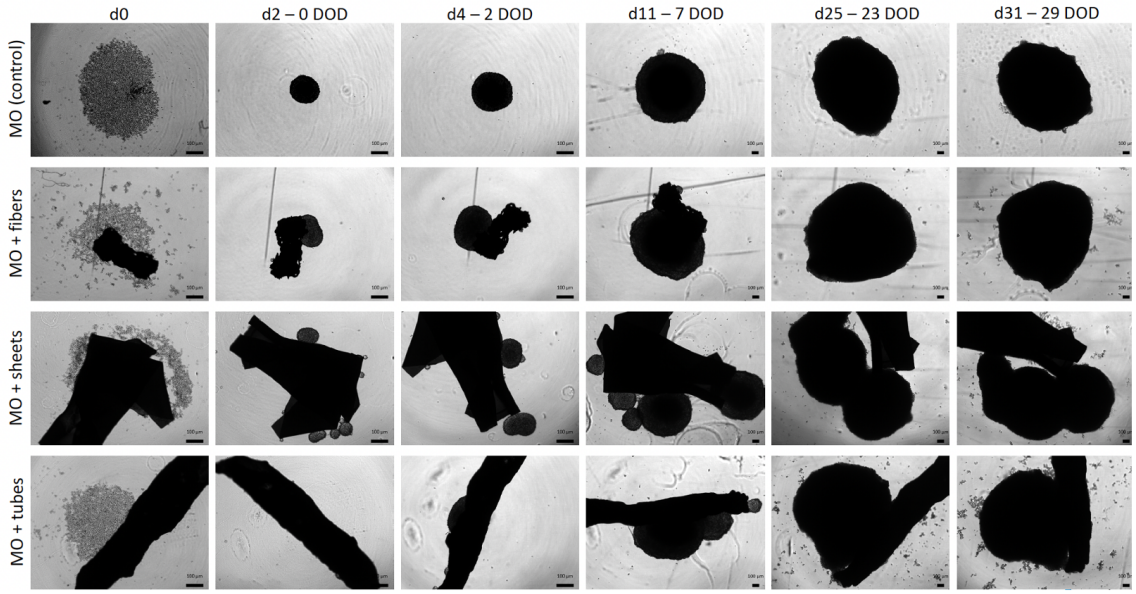

Figure 6.8: a) MO control. b)MO and fibres. c)MO and sheets d)MO and tubes. The images are from day 0 of differentiation to day 29.

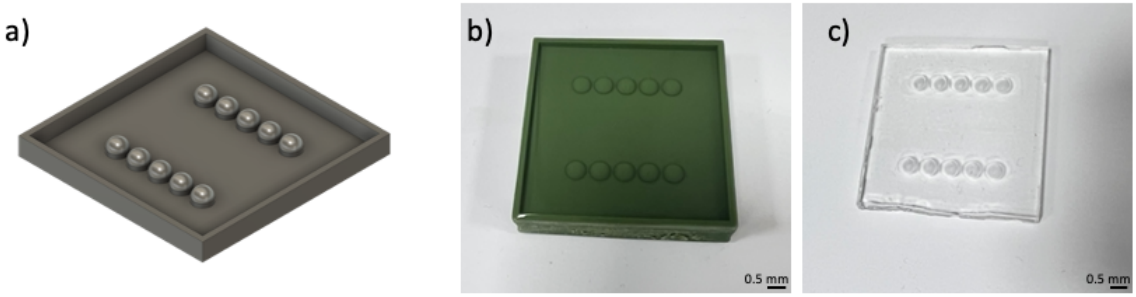

Figure 6.9: a) 3D print of the ice cube holder mold. b)PDMS filled in the mold c)The final PDMS ice cube holder taken out of the mold.

Transferring small 2 mm fibre snippets into cell plates posed a significant challenge because the fibres, only 20 μm in diameter, are difficult to see with the naked eye. Additionally, sterile conditions required the fibres to remain in 70% ethanol. To address this issue, I used a 3D-printed mold made of soft PDMS with the help of my colleague Deniz Avsar, to create mini ice cubes.

The mold contained hemispherical cavities with a 5 mm diameter, slightly smaller than the opening of a well plate as shown in figure 6.9. Each cavity was filled with 30 µL of water, ensuring the water level was flush with the mold's surface. A single long fiber was laid across multiple hemispheres, with one end positioned just before the first well and the other beyond the last (fifth) well. During this process, the fibre was slightly stretched due to the soft nature of the fibre, as it was laid over the mold's hemispheres. The mold was frozen at $-20°$C to encapsulate the stretched fiber within the ice cubes. At this temperature, which is below the glass transition temperature of the LCE material, the frozen fiber was cut using a scalpel at the diameter of each hemisphere. The mold was then placed upside down over the wells, and one ice cube

was punched into each well, carrying a 5 mm snippet of LCE fiber. After transferring the fiber snippets, 70 µL of 100% ethanol was added to each well, ensuring the solution reached a final concentration of 70% ethanol.

Chapter 7

Towards organoid growth supported by LCE tubes

7.1 LCE tubes with reduced transition temperature

7.1.1 Reduction of transition temperature using C6BAPE in LC oligomers

Based on literature study[87], (1,4-bis-[4-(6-acryloyloxyhexyloxy)benzoyloxy]-2-methylbenzene) (C6BAPE) was selected to decrease the transition temperature (T_{NI}) in liquid crystal oligomers (LCOs). The aim was to achieve a reduced transition temperature suitable for subsequent fabrication of LCE tubes. The chemical structure of C6BAPE and RM257 are shown in figure 7.1.

To investigate the effect of C6BAPE on T_{NI}, a modified LCO mixture was prepared by incorporating 10 wt% of C6BAPE into the reference LCO2 formulation. The modified oligomer, termed C6BAPE-LCO, was analyzed using DSC alongside the reference LCO2 to evaluate changes in thermal behavior. The DSC results indicated a significant reduction in T_{NI}, approximately at 35°C when C6BAPE was included. This

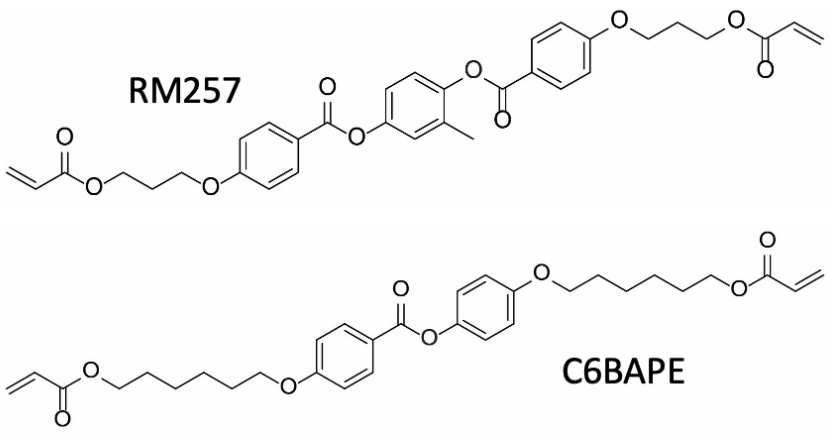

Figure 7.1: Chemical structure of RM257 and C6BAPE

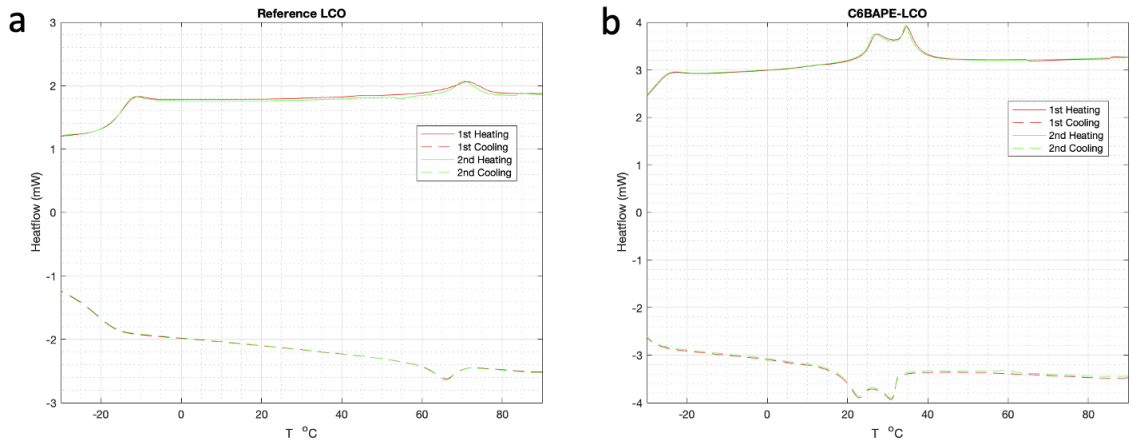

Figure 7.2: DSC data of oligomers: a) LCO2 previously used (reference) and b) C6BAPE-LCO. Both first and second heating and cooling cycles are shown.

reduction in T_{NI} can be attributed to the structural differences between C6BAPE and RM257. While RM257 contains a mesogenic core with three aromatic rings, C6BAPE has a simpler core with only two aromatic groups. This reduction in aromatic content decreases the $\pi - \pi$ interactions that typically strengthen mesogen-mesogen coupling. Consequently, the lower intermolecular forces result in a material leads to easier disruption of nematic ordering, lowering the T_{NI}. Over narrow temperature range ($25-30°C$) C6BAPE exhibits smectic phase upon heating, which was also evident in the heating and cooling run of the C6BAPE-LCO as shown in figure 7.2b.

In efforts to fabricate LCE tubes with reduced transition temperature to actuate in organoids, the modified C6BAPE-LCO was utilized to produce LCE tubes. This involved replacing the reference LCO mixture with the C6BAPE-LCO formulation in the established microfluidic process. For the original reference LCO, a mixture of 40 wt% LCO2 in DCM with Span 80 and 4 wt% of photoinitiator Irgacure 819 served as the middle phase, surrounded by an aqueous 10 wt% PVP solution as outer and inner phases. This configuration had previously yielded stable and elongated LCE tubes. In the modified process using C6BAPE-LCO, the middle phase was altered to 60 wt% C6BAPE-LCO in DCM, maintaining the same outer and inner phases. Despite utilizing the maximum UV intensity available in the setup, the C6BAPE-LCO tubes failed to polymerize effectively. Then the photoinitiator content in the LCO middle phase was increased from 4 wt% to 6 wt%, which also did not yield successful polymerized LCE tubes.

One possible reason for the failure to UV polymerize LCE tubes containing C6BAPE and RM257 can be attributed to their reactivity. In terms of reactivity, RM257 exhibits higher reactivity than C6BAPE. In both, the ester group (–COO–) within the acrylate has an electron-withdrawing inductive effect due to the electronegativity of oxygen in the carbonyl group. This electron density withdrawal increases the reactivity of the acrylate double bond by forming a partial positive charge on the β–carbon. C6BAPE has longer alkyl chains compared to RM257 and this may introduce some steric hindrance, which might reduce the C6BAPE's reactivity. The relatively small alkyl chain near the acrylate group in RM257 minimizes steric hindrance, allowing

radicals and other reactants easy access to the reactive double bond.

During our one-pot synthesis of oligomers, where C6BAPE, RM257, and EDDET were reacted together in the solvent with a catalyst, the higher reactivity of RM257 might have led it to react first with EDDET. This rapid reaction could have consumed all the available RM257 in the system, leaving the free acrylate ends of C6BAPE available for radical formation. To enhance the efficiency of polymerization, a more effective approach would be to allow C6BAPE to react with EDDET first, ensuring complete consumption of C6BAPE. After this step, we could introduce RM257 to react with the remaining thiol groups. This sequential strategy would yield oligomers with free acrylate ends derived from RM257, allowing us to exploit the more reactive acrylate end to facilitate rapid radical formation. This, in turn, would enable quicker initiation and propagation during the polymerization process. By understanding these factors, we can better strategize our synthesis processes and enhance the efficiency of UV polymerization in future experiments.

7.2 Light actuated tubes

7.2.1 An outlook towards modification of azobenzene moieties used in the LCEs.

In Chapter 5, the incorporation of azobenzene into the reference LCO system was explored, aiming to develop photoactivated LCE tubes that could operate at an optimal temperature of 37°C for use in organoids as peristaltic pumps. The initial approach yielded LCE films that actuate at optimal temperature of 30°C, showing slightly reduced actuation performance at 37°C. To shift the optimal actuation temperature closer to 37°C, one potential solution involves reducing the intensity of UV light used for actuation, thereby tuning the transition temperature to achieve peak performance at the desired 37°C.

Another approach to fine-tune the transition temperature is to vary the concentration of azobenzene in the system. Currently, azobenzene constitutes 10 wt% of the RM257 in the formulation. Tailoring the concentration of azobenzene moieties help achieve a desired transition temperature. Additionally, blending the azobenzene-containing system with C6BAPE-LCO oligomers could further tune the transition temperature of the azo-LCE. While these modifications may help in achieving the desired transition temperature, it is essential to consider the viability of the LCE system within organoids. Therefore, simultaneous experiments to assess cell viability alongside each system modification are crucial.

Assuming these systems are cell-compatible, another challenge arises: the use of UV light to actuate the azobenzene-LCE system could potentially harm the cells. This calls for the urgent need to transition from UV light to the visible spectrum for actuating the LCEs. Studies [88, 89] suggest that substituent groups can be introduced into azobenzene to facilitate photo-isomerization under visible light. Exploring these modifications may lead to the development of a more organoid-friendly LCE system while maintaining effective actuation.

7.2.2 Initial attempt to fabricate azo-LCE tubes using current azo-LCO formulation.

An initial attempt to fabricate light-actuated azo-LCE tubes was carried out using the azo-LCO formulation used in Chapter 5 and the microfluidic coaxial set-up used in Chapter 4 except for changing the UV-LEDs with four visible green-LEDs. For this experiment, 60 wt% azo-LCO in DCM was used as the middle phase and 10 wt% PVP aqueous solution was employed as both inner and outer phases. Although the middle phase contained visisble-light photoinitiaor Sn 784 and, the in-situ photopolymerization was attempted using a visible range LED source, challenges arose during polymerization.

Specifically, despite the intended use of visible light, the LED source emitted minor UV components. These residual UV wavelengths initiated trans-to-cis photoisomerization of the azobenzene moieties rather than generating the radicals necessary for photopolymerization. Furthermore, the intensity of the LED setup was likely insufficient to drive effective photopolymerization, even in the presence of the visible-light photoinitiator. As a result, no crosslinked azo-LCE tubes were produced in this attempt.

To overcome this limitation, future work must focus on ensuring strict wavelength control during photopolymerization. Using optical filters to eliminate any UV component and restricting the illumination strictly to the visible spectrum will help prevent unwanted photoisomerization and enable effective crosslinking. Another potential approach involves increasing the concentration of the photoinitiator to accelerate the rate of radical formation. In this initial trial, 4 wt% photoinitiator was used; increasing this amount could enhance polymerization efficiency. However, care must be taken not to exceed a critical threshold, as higher photoinitiator concentrations can alter the viscosity of the middle phase. This, in turn, could interfere with the Rayleigh–Plateau instability that can lead to breakage of the jet.

7.3 Further reduced tube diameter

7.3.1 Factors determining the diameter of the tubular flow

The LCE tube we tried to incorporate into organoids are on an average 300-400 μm in outer diameter. This could potentially disrupt the initial cell aggregation if it occupies too much space relative to the initial cell cluster. Our preliminary cell viability results have shown that, this has lead to uneven cell distribution around the tube and this can be the reason that the organoids are not integrating the tube segments completely rather shows an attaching on one side style. Hence there is a critical need of reducing the size of the LCE tubes by 20 folds so that the tubes can be integrated by the organoids.

To control the diameter of the LCE tube, fine tuning the flow rates of the different phases in the microfluidic process is essential. Adjusting the outer phase flow rate (PVP solution with Tween 20) has a direct impact: a higher outer flow rate is seen to cause the LCO phase to narrow and form thinner tubular structure. Figure 7.3 shows tubes with different diameters produced using the same microfluidic device

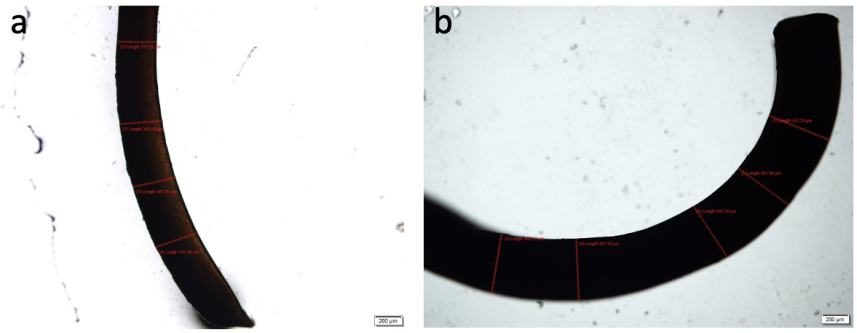

Figure 7.3: Two tube segments that are produced with different flow rates of the outer phase in the same microfluidic device keeping inner and middle phase flow rates the same, $\phi_i = 8.0$ mL/h and $\phi_m = 2.0$ mL/h respectively. The outer flow rates are: a)$\phi_o = 15.0$ mL/h; and b)$\phi_o = 9.0$ mL/h.

and keeping the inner and middle phase flow rates constant ($\phi_i = 8.0$ mL/h and $\phi_m = 2.0$ mL/h respectively) while varying the outer phase flow rate. At an outer flow rate of $\phi_o = 15.0$ mL/h (figure 7.3a,) the tube diameter was around 350 μm, whereas at $\phi_o = 9.0$ mL/h (figure 7.3b), it was about 500 μm. However, increasing the outer phase flow rate higher than $\phi_o = 15.0$ mL/h caused breakage of tubular flow, setting a practical limit. Additionally, keeping the middle phase flow rate very low will also help to decrease the diameter of the tube by limiting the amount of LCO solution available for tubular flow. Combining a low middle flow rate with a higher outer phase flow rate can help to achieve smaller diameter tubes.

Adjusting the viscosity and composition of each phase offers another path to control the diameter of the tubes. Increasing the viscosity of the middle phase delays the Rayleigh-Plateau instability, maintaining tubular flow. Also the viscosity of inner and outer phase can be increased to induce more shearing, helping narrow the middle phase further. Carefully tuning surfactant concentration can also help to balance the interfacial tension promoting narrow tube formation. However, excess surfactant can destabilize the flow. A systematic study of varying each parameter has to be conducted in the future to achieve the goal of narrower tubes.

7.4 IR-dye incorporated LCE tube production using polydopamine

To achieve actuation of LCE tubes within midbrain organoids (MOs), coating the LCE tubes with an infrared (IR) dye, specifically polydopamine (PDA) is proposed. PDA is an attractive choice due to its stability, biocompatibility, and adhesive functional groups, which enable it to form robust surface coatings across a range of materials [90]. Importantly, PDA can absorb IR light and convert it to heat, which could allow for controlled, localized heating of LCE tubes to induce actuation directly within the organoid culture environment (37°C).

Studies, such as those by Tian et al. [91], have demonstrated that PDA-coated LCE materials can be actuated by a near-infrared (NIR) laser. However, their results indicate that NIR-induced heating can lead to a significant temperature rise, potentially

harmful to cells. For application in MOs, this effect may pose a risk to organoid viability if excessive heating occurs, so careful calibration and control of NIR exposure would be essential if PDA-based actuation is pursued.

Beyond actuation, PDA offers additional benefits for improving cell adhesion and growth on the LCE tubes. Prior studies have shown that PDA enhances cell attachment and proliferation [92], which may promote a more stable and extensive interaction between the organoid cells and the LCE surface. Coating the LCE tubes with PDA may enhance cell adhesion and viability in the MO cultures, potentially enabling the cells to cover more of the LCE surface and foster healthier organoid development. Given PDA's biocompatibility, it is expected to increase the likelihood of cell survival and integration with the LCE material.

This approach may also allow the use of slightly larger-diameter LCE tubes (100–200 µm) rather than aiming for 20 µm tubes. The PDA coating could encourage sufficient cellular attachment and coverage of the tubes, even at these larger diameters. Thus, even if NIR-based actuation is not feasible due to heat concerns, the PDA coating alone could offer substantial benefits by improving the cell adhesion properties of the LCE tubes, supporting better integration and stability of midbrain organoid cultures.

7.5 Porous LCE tubes

The LCE tubes fabricated using the nested capillary setup are currently hollow, soft, and sticky in nature, but lack inherent porosity. To extend the functionality of these tubes in organoids, for nutrient exchange and waste removal in the core, these tubes have to be porous. One potential approach to achieve this could involve the incorporation of porogens during the fabrication process. These are materials or chemicals added to a system during fabrication that, once the process is complete, are removed to leave behind pores.

When selecting porogens for introducing porosity into LCE tubes, several factors must be carefully considered. The porogens must be soluble in the LC oligomer precursor solution dissolved in DCM without affecting the solubility or stability of the material. It is critical that the chosen porogens do not significantly alter the viscosity or surface tension of the precursor solution, as this could trigger Rayleigh-Plateau instability during tube formation. Additionally, the porogen should be removable after crosslinking, either by washing, heating, or dissolution, to ensure the creation of controlled porosity without compromising the integrity of the LCE tubes. A recommended approach is to begin with low concentrations of polymeric or salt-based porogens, closely monitoring the flow behavior to ensure stability in the microfluidic setup. Once stable tube formation is achieved, the porogen can be removed post-crosslinking, leaving behind a porous structure. This process will enable the fabrication of LCE tubes with tailored porosity for enhanced functionality while maintaining structural integrity.

Chapter 8

Conclusion and outlook

This thesis has focused on addressing fundamental and practical challenges in developing LCEs as soft, responsive actuators for potential applications in biointegrated systems, especially organoids. The work begins with the development of long, hollow LCE tubes using a coaxial microfluidic method, followed by the exploration of photoresponsive LCE sheets as a step toward creating light-actuated LCE tubes. Finally, the biocompatibility of these LCE materials was evaluated in midbrain organoid cultures, confirming that, with proper tuning of geometry and dimensions, LCEs can integrate into biological systems without negatively affecting cell viability.

The first major contribution of this work was the successful fabrication of continuous, hollow LCE tubes using a coaxial flow microfluidic setup. Traditional LCE fabrication methods have mostly been limited to flat sheets or short sections of tubes due to challenges in controlling shape, diameter, alignment, and scalability. In contrast, the method developed in this work allows the formation of arbitrarily long tubes, with tunable diameters and improved alignment of the liquid crystalline domains through flow-induced shear. The resulting LCE tubes were thermally actuated and showed reversible shape change upon heating and cooling. Under localized heating, they even demonstrated peristaltic-like motion, which could be harnessed in the future for fluid pumping, potentially serving as artificial vasculature systems. These findings mark a step forward in the realization of dynamic and soft structures that could support fluid transport in confined biological environments.

Following this, the focus shifted toward introducing light-responsive behavior into the LCEs. The aim was to move toward developing photoresponsive tubes that could actuate under light stimuli, without the need for temperature changes, which is important because high heat can damage living cells. By carefully tuning the chemistry and characterizing the response, the range of temperatures and light conditions where actuation works best was identified. A key innovation in this study was the establishment of a robust synthetic pathway using tetrathiol crosslinker in the LCO formulation, that enabled formation of well-aligned LCE network that is capable of reliable actuation at physiologically relevant temperatures.

Critically, a comprehensive investigation into light-driven actuation behavior as a function of temperature revealed that the most effective actuation occurred at 30°C with slightly reduced actuation at 37°C. This isothermal actuation is achieved through

UV-induced *trans–cis* isomerization of azobenzene moieties, which disrupts the nematic phase and lowers the order parameter. The complex interplay between director alignment, phase behavior, and *trans–cis* isomerization was mapped using polarized optical microscopy.

Importantly, these investigations illuminated the operational boundaries for achieving reliable isothermal actuation in biological environments. While limitations remain—especially concerning the mutual interference between photoisomerization and photocrosslinking—this work identified design strategies that mitigate such trade-offs, including optimized chromophore incorporation and using visible photoinitiators. These light-sensitive LCEs are promising for future use in systems that need local, gentle, and reversible actuation.

The final phase of the research focused on evaluating the interaction between the developed LCE materials and biological systems, specifically in the context of midbrain organoids. LCE tubes, fibres and sheets were introduced into the organoid cultures at the early stages of differentiation, and their integration was monitored over time. While LCE tubes and sheets were too large to be embedded effectively, thinner fibres with diameters around 10–20 μm were found to be completely integrated into the organoids. Cell viability assays, including LDH analysis, showed minimal cytotoxicity, confirming the general biocompatibility of the LCE material when the dimensions are appropriate. These results reinforce the importance of size and mechanical properties when designing soft actuators for biointegration.

Looking forward, several promising directions emerge from this work. The miniaturization of LCE tubes to diameters below 100 µm, though technically challenging, remains a key challenge for achieving closer mimicry of vascular capillaries. Addressing this will require further optimization of microfluidic geometries and flow conditions, as well as continued refinement of precursor formulations. Instead of pursuing highly light-sensitive LCEs with novel dyes, a more immediate avenue is the refinement of existing azobenzene chemistries to ensure actuation under visible light with minimal photothermal or phototoxic side effects. This could involve concentration tuning or hybrid dopant strategies.

Porosity engineering represents another frontier. By introducing controlled porosity within LCE walls, possibly through templated phase separation or using porogens, nutrients and oxygen diffusion through the actuator wall can be enabled, bringing the concept of perfusable artificial vasculature closer to reality. Additionally, the incorporation of biochemical functionalization (e.g., peptide ligands or extra cellular matrix-mimetic coatings) could enhance cellular adhesion and signaling at the material-tissue interface, transforming LCEs from passive structures into active participants in cellular development.

Lastly, while this thesis focused on midbrain organoids, extending similar integration studies to other organoid types (e.g., intestinal or hepatic) will test the generalizability of the material design and fabrication strategy. Each system poses unique challenges in terms of mechanical load, curvature response, and biochemical compatibility. Extending this work to tissues with different geometric and mechanical demands will provide deeper insight into the versatility of LCEs in biological applications.

In summary, this thesis provides an experimentally validated foundation for integrat-

ing LCEs into soft, bioengineered environments. Through meticulous integration of chemistry, physics, and biology and by demonstrating scalable fabrication, tailored actuation, and biological compatibility, it opens the door for future development of active materials that can support and interact with living tissues in meaningful ways.

Bibliography

(1) Hines, L.; Petersen, K.; Lum, G. Z.; Sitti, M. Soft actuators for small-scale robotics. *Advanced materials* **2017**, *29*, 1603483.

(2) Hussain, M.; Jull, E. I.; Mandle, R. J.; Raistrick, T.; Hine, P. J.; Gleeson, H. F. Liquid crystal elastomers for biological applications. *Nanomaterials* **2021**, *11*, 813.

(3) Kim, H.; Gibson, J.; Maeng, J.; Saed, M. O.; Pimentel, K.; Rihani, R. T.; Pancrazio, J. J.; Georgakopoulos, S. V.; Ware, T. H. Responsive, 3D electronics enabled by liquid crystal elastomer substrates. *ACS applied materials & interfaces* **2019**, *11*, 19506–19513.

(4) Seok, S.; Onal, C. D.; Cho, K.-J.; Wood, R. J.; Rus, D.; Kim, S. Meshworm: a peristaltic soft robot with antagonistic nickel titanium coil actuators. *IEEE/ASME Transactions on mechatronics* **2012**, *18*, 1485–1497.

(5) Murase, Y.; Maeda, S.; Hashimoto, S.; Yoshida, R. Design of a mass transport surface utilizing peristaltic motion of a self-oscillating gel. *Langmuir* **2009**, *25*, 483–489.

(6) Fung, Y.-C.; Yih, C.-S. Peristaltic transport. *Journal of Applied Mechanics, Transactions ASME* **1968**.

(7) Selinger, R. L.; Mbanga, B. L.; Selinger, J. V. Modeling liquid crystal elastomers: actuators, pumps, and robots. *Emerging Liquid Crystal Technologies III* **2008**, *6911*, 82–86.

(8) Liu, X.; Kim, S.-K.; Wang, X. Thermomechanical liquid crystalline elastomer capillaries with biomimetic peristaltic crawling function. *Journal of Materials Chemistry B* **2016**, *4*, 7293–7302.

(9) Qian, X.; Chen, Q.; Yang, Y.; Xu, Y.; Li, Z.; Wang, Z.; Wu, Y.; Wei, Y.; Ji, Y. Untethered recyclable tubular actuators with versatile locomotion for soft continuum robots. *Advanced Materials* **2018**, *30*, 1801103.

(10) He, Q.; Wang, Z.; Wang, Y.; Minori, A.; Tolley, M. T.; Cai, S. Electrically controlled liquid crystal elastomer–based soft tubular actuator with multimodal actuation. *Science advances* **2019**, *5*, eaax5746.

(11) Wang, Z.; Wang, Z.; Zheng, Y.; He, Q.; Wang, Y.; Cai, S. Three-dimensional printing of functionally graded liquid crystal elastomer. *Science advances* **2020**, *6*, eabc0034.

(12) Braun, L. B.; Hessberger, T.; Pütz, E.; Müller, C.; Giesselmann, F.; Serra, C. A.; Zentel, R. Actuating thermo-and photo-responsive tubes from liquid crystalline elastomers. *Journal of Materials Chemistry C* **2018**, *6*, 9093–9101.

(13) Liu, W.; Guo, L.-X.; Lin, B.-P.; Zhang, X.-Q.; Sun, Y.; Yang, H. Near-infrared responsive liquid crystalline elastomers containing photothermal conjugated polymers. *Macromolecules* **2016**, *49*, 4023–4030.

(14) Ikeda, T.; Mamiya, J.-i.; Yu, Y. Photomechanics of liquid-crystalline elastomers and other polymers. *Angewandte Chemie International Edition* **2007**, *46*, 506–528.
(15) Lagerwall, J. Liquid crystal elastomer actuators and sensors: Glimpses of the past, the present and perhaps the future. *Programmable Materials* **2023**, *1*, e9.
(16) Ohzono, T.; Koyama, E. Optimal conditions for efficient photomechanical response in nematic elastomers. *Macromolecules* **2023**, *56*, 5346–5355.
(17) Jeong, Y.-J.; Park, S.-Y. Light-Responsive Actuator of Azobenzene-Containing Main-Chain Liquid Crystal Elastomers with Allyl Sulfide Dynamic Exchangeable Linkages. *ACS applied materials & interfaces* **2024**, *16*, 2788–2801.
(18) Stephen, M. J.; Straley, J. P. Physics of liquid crystals. *Reviews of Modern Physics* **1974**, *46*, 617.
(19) Maitra, A.; Das, T.; Das, C. K. Liquid Crystalline Polymer and Its Composites: Chemistry and Recent Advances. *Liquid Crystalline Polymers: Volume 2–Processing and Applications* **2015**, 103–131.
(20) De Gennes, P.-G.; Prost, J., *The physics of liquid crystals*; Oxford university press: 1993.
(21) Jampani, V.; Volpe, R. Reguengo de Sousa, K. *Ferreira Machado, J., Yakacki, CM and Lagerwall, JPF,"Liquid crystal elastomer shell actuators with negative order parameter," Sci. Adv* **2019**, *5*.
(22) Pellicer, J.; Manzanares, J. A.; Zúñiga, J.; Utrillas, P.; Fernández, J. Thermodynamics of rubber elasticity. *Journal of Chemical Education* **2001**, *78*, 263.
(23) Treloar, L. G., *The physics of rubber elasticity*; OUP Oxford: 1975.
(24) Gough, J. VII. A description of a property of caoutchouc, or indian rubber; with some reflections on the cause of the elasticity of this substance. In a letter to Dr. Holme. *The Philosophical Magazine* **1806**, *24*, 39–43.
(25) Joule, J. P. V. On some thermo-dynamic properties of solids. *Philosophical Transactions of the Royal Society of London* **1859**, 91–131.
(26) Geethamma, V.; Sampath, V. Rubber as an aid to teach thermodynamics: The discovery by a blind scientist. *Resonance* **2019**, *24*, 217–238.
(27) Rubinstein, M.; Colby, R. H., *Polymer physics*; Oxford university press: 2003.
(28) Warner, M.; Terentjev, E. M., *Liquid crystal elastomers*; Oxford university press: 2007; Vol. 120.
(29) Ohm, C.; Brehmer, M.; Zentel, R. Liquid crystalline elastomers as actuators and sensors. *Advanced materials* **2010**, *22*, 3366–3387.
(30) Ula, S. W.; Traugutt, N. A.; Volpe, R. H.; Patel, R. R.; Yu, K.; Yakacki, C. M. Liquid crystal elastomers: an introduction and review of emerging technologies. *Liquid Crystals Reviews* **2018**, *6*, 78–107.
(31) McCracken, J. M.; Donovan, B. R.; White, T. J. Materials as machines. *Advanced Materials* **2020**, *32*, 1906564.
(32) Wermter, H.; Finkelmann, H. Liquid crystalline elastomers as artificial muscles. *e-Polymers* **2001**, *1*, 013.
(33) White, T. J.; Broer, D. J. Programmable and adaptive mechanics with liquid crystal polymer networks and elastomers. *Nature materials* **2015**, *14*, 1087–1098.

(34) Mayer, S.; Zentel, R. Liquid crystalline polymers and elastomers. *Current Opinion in Solid State and Materials Science* **2002**, *6*, 545–551.
(35) De Jeu, W. H., *Liquid crystal elastomers: materials and applications*; Springer: 2012; Vol. 250.
(36) Küpfer, J.; Finkelmann, H. Nematic liquid single crystal elastomers. *Die Makromolekulare Chemie, Rapid Communications* **1991**, *12*, 717–726.
(37) Verwey, G.; Warner, M. Soft rubber elasticity. *Macromolecules* **1995**, *28*, 4303–4306.
(38) Herbert, K. M.; Fowler, H. E.; McCracken, J. M.; Schlafmann, K. R.; Koch, J. A.; White, T. J. Synthesis and alignment of liquid crystalline elastomers. *Nature Reviews Materials* **2022**, *7*, 23–38.
(39) Dey, S.; Agra-Kooijman, D. M.; Ren, W.; McMullan, P. J.; Griffin, A. C.; Kumar, S. Soft elasticity in main chain liquid crystal elastomers. *Crystals* **2013**, *3*, 363–390.
(40) Küupfer, J.; Finkelmann, H. Liquid crystal elastomers: Influence of the orientational distribution of the crosslinks on the phase behaviour and reorientation processes. *Macromolecular chemistry and physics* **1994**, *195*, 1353–1367.
(41) Clarke, S.; Terentjev, E.; Kundler, I.; Finkelmann, H. Texture evolution during the polydomain-monodomain transition in nematic elastomers. *Macromolecules* **1998**, *31*, 4862–4872.
(42) Warner, M.; Bladon, P.; Terentjev, E. "Soft elasticity"—deformation without resistance in liquid crystal elastomers. *Journal de Physique II* **1994**, *4*, 93–102.
(43) Finkelmann, H.; Kock, H.-J.; Rehage, G. Investigations on liquid crystalline polysiloxanes 3. Liquid crystalline elastomers—a new type of liquid crystalline material. *Die Makromolekulare Chemie, Rapid Communications* **1981**, *2*, 317–322.
(44) Thomsen, D. L.; Keller, P.; Naciri, J.; Pink, R.; Jeon, H.; Shenoy, D.; Ratna, B. R. Liquid crystal elastomers with mechanical properties of a muscle. *Macromolecules* **2001**, *34*, 5868–5875.
(45) Zeng, H.; Wani, O. M.; Wasylczyk, P.; Kaczmarek, R.; Priimagi, A. Self-regulating iris based on light-actuated liquid crystal elastomer. *Advanced materials* **2017**, *29*, 1701814.
(46) Ohm, C.; Serra, C.; Zentel, R. A Continuous Flow Synthesis of Micrometer-Sized Actuators from Liquid Crystalline Elastomers. *Advanced Materials* **2009**, *21*, 4859–4862.
(47) Yakacki, C.; Saed, M.; Nair, D.; Gong, T.; Reed, S.; Bowman, C. Tailorable and programmable liquid-crystalline elastomers using a two-stage thiol–acrylate reaction. *Rsc Advances* **2015**, *5*, 18997–19001.
(48) Ware, T.; White, T. Programmed liquid crystal elastomers with tunable actuation strain. *Polymer Chemistry* **2015**, *6*, 4835–4844.
(49) Zhang, H.; Meng, X.; Li, P. Light and thermal-stimuli responsive materials. *Progress in Chemistry* **2008**, *20*, 657.
(50) Yang, H.; Liu, J.-J.; Wang, Z.-F.; Guo, L.-X.; Keller, P.; Lin, B.-P.; Sun, Y.; Zhang, X.-Q. Near-infrared-responsive gold nanorod/liquid crystalline elastomer composites prepared by sequential thiol-click chemistry. *Chemical Communications* **2015**, *51*, 12126–12129.

(51) Camacho-Lopez, M.; Finkelmann, H.; Palffy-Muhoray, P.; Shelley, M. Fast liquid-crystal elastomer swims into the dark. *Nature materials* **2004**, *3*, 307–310.
(52) Kohlmeyer, R. R.; Chen, J. Wavelength-selective, IR light-driven hinges based on liquid crystalline elastomer composites. *Angewandte Chemie International Edition* **2013**, *52*.
(53) Miao, Z.-C.; Zhang, Y.-M.; Zhao, Y.-Z.; Wang, D. Azobenzene Liquid Crystals with High Birefringence and Their Effect of Trans-Cis Photoisomerization on Selective Reflection. *Molecular Crystals and Liquid Crystals* **2013**, *582*, 98–106.
(54) Alaasar, M. Azobenzene-containing bent-core liquid crystals: an overview. *Liquid Crystals* **2016**, *43*, 2208–2243.
(55) Knopf, G. K.; Otani, Y., *Optical nano and micro actuator technology*; CRC Press: 2012.
(56) Birabassov, R.; Landraud, N.; Galstyan, T. V.; Ritcey, A.; Bazuin, C. G.; Rahem, T. Thick dye-doped poly (methyl methacrylate) films for real-time holography. *Applied optics* **1998**, *37*, 8264–8269.
(57) Finkelmann, H.; Nishikawa, E.; Pereira, G.; Warner, M. A new opto-mechanical effect in solids. *Physical Review Letters* **2001**, *87*, 015501.
(58) Gao, Y.; Mori, T.; Manning, S.; Zhao, Y.; Nielsen, A. D.; Neshat, A.; Sharma, A.; Mahnen, C. J.; Everson, H. R.; Crotty, S., et al. Biocompatible 3D liquid crystal elastomer cell scaffolds and foams with primary and secondary porous architecture. *ACS Macro Letters* **2016**, *5*, 4–9.
(59) Lancaster, M. A.; Knoblich, J. A. Organogenesis in a dish: modeling development and disease using organoid technologies. *Science* **2014**, *345*, 1247125.
(60) Clevers, H. Modeling development and disease with organoids. *Cell* **2016**, *165*, 1586–1597.
(61) Kaushik, G.; Ponnusamy, M. P.; Batra, S. K. Concise review: current status of three-dimensional organoids as preclinical models. *Stem Cells* **2018**, *36*, 1329–1340.
(62) Bartfeld, S.; Clevers, H. Stem cell-derived organoids and their application for medical research and patient treatment. *Journal of molecular medicine* **2017**, *95*, 729–738.
(63) Gerakis, Y.; Hetz, C. Brain organoids: a next step for humanized Alzheimer's disease models? *Molecular Psychiatry* **2019**, *24*, 474–478.
(64) Monzel, A. S.; Smits, L. M.; Hemmer, K.; Hachi, S.; Moreno, E. L.; van Wuellen, T.; Jarazo, J.; Walter, J.; Brüggemann, I.; Boussaad, I., et al. Derivation of human midbrain-specific organoids from neuroepithelial stem cells. *Stem cell reports* **2017**, *8*, 1144–1154.
(65) Takebe, T.; Wells, J. M.; Helmrath, M. A.; Zorn, A. M. Organoid center strategies for accelerating clinical translation. *Cell Stem Cell* **2018**, *22*, 806–809.
(66) Huch, M.; Knoblich, J. A.; Lutolf, M. P.; Martinez-Arias, A. The hope and the hype of organoid research. *Development* **2017**, *144*, 938–941.
(67) Yin, X.; Mead, B. E.; Safaee, H.; Langer, R.; Karp, J. M.; Levy, O. Stem cell organoid engineering. *Cell stem cell* **2016**, *18*, 25.
(68) Muschler, G. F.; Nakamoto, C.; Griffith, L. G. Engineering principles of clinical cell-based tissue engineering. *JBJS* **2004**, *86*, 1541–1558.

(69) He, Q.; Wang, Z.; Wang, Y.; Wang, Z.; Li, C.; Annapooranan, R.; Zeng, J.; Chen, R.; Cai, S. Electrospun liquid crystal elastomer microfiber actuator. *Science robotics* **2021**, *6*, eabi9704.
(70) Najiya, N.; Popov, N.; Jampani, V. S. R.; Lagerwall, J. P. Continuous flow microfluidic production of arbitrarily long tubular liquid crystal elastomer peristaltic pump actuators. *Small* **2023**, *19*, 2204693.
(71) Reynolds, O. XXIX. An experimental investigation of the circumstances which determine whether the motion of water shall be direct or sinuous, and of the law of resistance in parallel channels. *Philosophical Transactions of the Royal society of London* **1883**, 935–982.
(72) Carey, V. P., *Liquid-vapor phase-change phenomena: an introduction to the thermophysics of vaporization and condensation processes in heat transfer equipment*; CRC Press: 2020.
(73) Utada, A. S.; Fernandez-Nieves, A.; Stone, H. A.; Weitz, D. A. Dripping to jetting transitions in coflowing liquid streams. *Physical review letters* **2007**, *99*, 094502.
(74) Umbanhowar, P.; Prasad, V.; Weitz, D. A. Monodisperse emulsion generation via drop break off in a coflowing stream. *Langmuir* **2000**, *16*, 347–351.
(75) Powers, T. R.; Zhang, D.; Goldstein, R. E.; Stone, H. A. Propagation of a topological transition: the Rayleigh instability. *Physics of Fluids* **1998**, *10*, 1052–1057.
(76) Utada, A.; Chu, L.-Y.; Fernandez-Nieves, A.; Link, D.; Holtze, C.; Weitz, D. Dripping, jetting, drops, and wetting: The magic of microfluidics. *Mrs Bulletin* **2007**, *32*, 702–708.
(77) Gennes, P.-G.; Brochard-Wyart, F.; Quéré, D., et al., *Capillarity and wetting phenomena: drops, bubbles, pearls, waves*; Springer: 2004.
(78) Clanet, C.; Lasheras, J. C. Transition from dripping to jetting. *Journal of fluid mechanics* **1999**, *383*, 307–326.
(79) Eggers, J.; Villermaux, E. Physics of liquid jets. *Reports on progress in physics* **2008**, *71*, 036601.
(80) Arratia, P. E.; Cramer, L.; Gollub, J. P.; Durian, D. J. The effects of polymer molecular weight on filament thinning and drop breakup in microchannels. *New Journal of physics* **2009**, *11*, 115006.
(81) Vats, S.; Anyfantakis, M.; Honaker, L. W.; Basoli, F.; Lagerwall, J. P. Stable Electrospinning of Core-Functionalized Coaxial Fibers Enabled by the Minimum-Energy Interface Given by Partial Core–Sheath Miscibility. *Langmuir* **2021**, *37*, 13265–13277.
(82) Hashimoto, M.; Garstecki, P.; Stone, H. A.; Whitesides, G. M. Interfacial instabilities in a microfluidic Hele-Shaw cell. *Soft Matter* **2008**, *4*, 1403–1413.
(83) Rosen, M. J.; Kunjappu, J. T., *Surfactants and interfacial phenomena*; John Wiley & Sons: 2012.
(84) Biggins, J.; Warner, M.; Bhattacharya, K. Supersoft elasticity in polydomain nematic elastomers. *Physical review letters* **2009**, *103*, 037802.
(85) Schätzle, J.; Finkelmann, H. State of order in liquid crystalline elastomers. *Molecular Crystals and Liquid Crystals* **1987**, *142*, 85–100.
(86) Xiao, Y.; Wu, J.; Zhang, Y. Recent advances in the design, fabrication, actuation mechanisms and applications of liquid crystal elastomers. *Soft Science* **2023**.

(87) McCracken, J. M.; Donovan, B. R.; Lynch, K. M.; White, T. J. Molecular engineering of mesogenic constituents within liquid crystalline elastomers to sharpen thermotropic actuation. *Advanced Functional Materials* **2021**, *31*, 2100564.
(88) Iamsaard, S.; Anger, E.; Aßhoff, S. J.; Depauw, A.; Fletcher, S. P.; Katsonis, N. Fluorinated azobenzenes for shape-persistent liquid crystal polymer networks. *Angewandte Chemie* **2016**, *128*, 10062–10066.
(89) Bléger, D.; Schwarz, J.; Brouwer, A. M.; Hecht, S. o-Fluoroazobenzenes as readily synthesized photoswitches offering nearly quantitative two-way isomerization with visible light. *Journal of the American Chemical Society* **2012**, *134*, 20597–20600.
(90) Barclay, T. G.; Hegab, H. M.; Clarke, S. R.; Ginic-Markovic, M. Versatile surface modification using polydopamine and related polycatecholamines: Chemistry, structure, and applications. *Advanced Materials Interfaces* **2017**, *4*, 1601192.
(91) Tian, H.; Wang, Z.; Chen, Y.; Shao, J.; Gao, T.; Cai, S. Polydopamine-coated main-chain liquid crystal elastomer as optically driven artificial muscle. *ACS applied materials & interfaces* **2018**, *10*, 8307–8316.
(92) Tolabi, H.; Bakhtiary, N.; Sayadi, S.; Tamaddon, M.; Ghorbani, F.; Boccaccini, A. R.; Liu, C. A critical review on polydopamine surface-modified scaffolds in musculoskeletal regeneration. *Frontiers in Bioengineering and Biotechnology* **2022**, *10*, 1008360.
(93) Donnio, B.; Wermter, H.; Finkelmann, H. A simple and versatile synthetic route for the preparation of main-chain, liquid-crystalline elastomers. *Macromolecules* **2000**, *33*, 7724–7729.
(94) Lancaster, M. A. Brain organoids get vascularized. *Nature biotechnology* **2018**, *36*, 407–408.
(95) Bergmann, G. H.; Finkelmann, H.; Percec, V.; Zhao, M. Liquid-crystalline main-chain elastomers. *Macromolecular rapid communications* **1997**, *18*, 353–360.
(96) Barbosa, C. A.; Gomes, A. S. Living tandem free radical polymerization of a liquid crystalline monomer. *Polymer Bulletin* **1998**, *41*, 15–20.
(97) Engler, A. J.; Sen, S.; Sweeney, H. L.; Discher, D. E. Matrix elasticity directs stem cell lineage specification. *Cell* **2006**, *126*, 677–689.
(98) Wang, T.-L.; Tsai, J.-S.; Tseng, C.-G. Synthesis and characterization of side-chain liquid-crystalline polyurethane elastomers. *Journal of applied polymer science* **2005**, *96*, 336–344.
(99) Godman, N. P.; Kowalski, B. A.; Auguste, A. D.; Koerner, H.; White, T. J. Synthesis of elastomeric liquid crystalline polymer networks via chain transfer. *ACS macro letters* **2017**, *6*, 1290–1295.
(100) Zha, F.; Wang, T.; Luo, M.; Guan, J. Tubular micro/nanomotors: Propulsion mechanisms, fabrication techniques and applications. *Micromachines* **2018**, *9*, 78.
(101) Ware, T. H.; McConney, M. E.; Wie, J. J.; Tondiglia, V. P.; White, T. J. Voxelated liquid crystal elastomers. *Science* **2015**, *347*, 982–984.